UNIVERSITY of CALIFORNIA
SANTA CRUZ

SEARCH FOR HIGH-ENERGY EMISSION FROM GAMMA-RAY BURSTS WITH A LARGE WATER CERENKOV DETECTOR

A dissertation submitted in partial satisfaction of the
requirements for the degree of

DOCTOR OF PHILOSOPHY

in

PHYSICS

by

Tom Yang

December 1998

The dissertation of Tom Yang is approved:

Professor Dave E. Dorfan, Chair

Professor George Blumenthal

Professor David A. Williams

Dean of Graduate Studies

Abstract

Search For High-Energy Emission From Gamma-Ray Bursts
With A Large Water Cerenkov Detector

by

Tom Yang

Milagrisimo, the first-stage prototype of the Milagro detector, took data around the clock, from April to June in 1996, with a peak trigger rate of 125 Hz. There are 528 million recorded air showers and 472 million (90%) of them are successfully reconstructed off-line with an overall angular resolution of 2.1 degrees. The energy threshold of triggered events from all incident angles is approximately 100 GeV, and the median energy of all triggered events is about 3.5 TeV. Monte Carlo simulations, data reduction, and data analysis are performed to search for radiation from the directions of gamma-ray bursts that are listed in BATSE's 4B catalog. No evidence of statistically significant excess above the expected cosmic-ray background is found from the direction of any of the 16 GRBs in the field of view of Milagrisimo. Upper limits for the steady flux above 3.5 TeV are quoted at 90% confidence level.

Contents

List of Figures

List of Tables

To my Father,

Liang-Cheng Yang.

Acknowledgments

I would like to express my deep appreciation to Professor David A. Williams and Professor Dave E. Dorfan for their unconditional (literally) supports and unbelievable patience. Their supervision and encouragement guided me through quite a journey.

Many thanks to Dr. Gus Sinnis, Dr. Cy Hoffman, Scott Delay and all other fellow workers in the CYGNUS and the Milagro collaborations. People in Los Alamos have been very nice to me, and I wouldn't trade those colorful days for anything else.

Finally, I thank Professor George Blumenthal for spending time reading the draft.

Chapter 1

Introduction

The recent results from a space satellite experiment — BATSE — one of the detectors on the Compton Gamma Ray Observatory (CGRO), revolutionized our knowledge about gamma-ray bursts. At random intervals, a random spot in the sky emits a burst of high-energy photons towards us, which lasts only for a short period of time, varying anywhere from a tenth of a second to 2 hours. This distinct astronomical phenomenon is given the name gamma-ray burst (GRB). The energies of emitted photons, as detected by the satellite, range from a few KeV to as high as 18 GeV (Hurley, 1994). Among different gamma-ray bursts, the photon fluxes, energy spectra, light curves (distribution in arrival times of photons), and counterparts in other wavelength ranges can differ significantly. This wide variety makes GRBs difficult to understand, especially as regards their origins and the underlying processes. Some theorists propose that a GRB may be caused by a merger between a pair of neutron stars, or a pair of black holes (Mészáros, 1995). These theories are yet to be tested. In fact, the nature of GRBs remains an enduring mystery.

Some energetic sources might sound familiar, such as neutron stars, supernova remnants or the long-known existence of high-energy cosmic rays. Why are these gamma-ray bursts so special? There are several reasons to distinguish GRBs from other high-energy sources. First, GRBs appear to be isotropically distributed and there is no indication of any enhancement in the plane of our galaxy. This could mean one of the two things, either GRBs are located very close to the earth, i.e., at a distance much smaller than the galactic disc, or they do not occur inside our galaxy, i.e., at a distance much larger than the galactic disc. The second alternative would place them at cosmological distances, and would imply that enormous energies are released during a burst given the amount of energy collected on a tiny satellite, even if they are narrowly beamed.[1] Second, GRBs do not repeat. The underlying emission process may happen only once at the source location. Third, the energy range of detected photons from GRBs is very broad. Last, it is difficult to observe counterparts for GRBs. Only recently in 1997, several GRBs were discovered with x-ray and optical counterparts and the optical redshifts showed these GRBs were indeed at great distance. These observations will be described in some detail in Section 1.2. The energies released from these distant GRBs were comparable to the rest-mass energy of the sun (2×10^{54} erg). Furthermore, there is as yet no indication of a cut-off limit in the γ-ray spectrum. This study focuses on detection of GRB photons with energies much higher than those detected

[1] The source is emitting photons in a small cone instead of all directions.

by BATSE.

Because a satellite has small surface area and weight limitations, which restrict both the chance of observation of GRBs and energy ceiling, more particularly the probability of detecting the highest energy γ-rays, the use of large ground-based detectors to search for GRBs takes place as a natural alternative for their detection. Milagro, a large water Čerenkov detector sensitive to gamma rays above a few hundred GeV, is an ideal ground-based detector to search for high-energy GRBs.

In the following few sections, the progress in astrophysics in the detection of lower energy portions of the γ-ray spectrum is briefly reviewed, because it is relevant to GRBs, before discussions of the TeV (10^{12} eV) realm in the fifth section. BATSE and EGRET, which is another instrument on the CGRO, will be described in their own sections. A model for GRBs is presented after the section about BATSE.

As is the case for particle accelerator experiments, astrophysics experiments targeting different energy regions often require very different techniques. For instance, detectors on satellites are not suitable for conducting TeV range experiments, and, in contrast, ground-based detectors are not useful in detecting GeV radiation. The biggest technical difference between a space-based instrument and a ground-based experiment arises from the existence of the atmosphere. Air showers are generated when high energy particles travel through the atmosphere. Section 1.5 explains in some detail the general air-shower technique using the CYGNUS air-shower array as an example. The air Čerenkov method is described in Section 1.6 because of its important role in TeV γ-ray detection. In the last section of this chapter, the water Čerenkov technique for the ground-based experiments is proposed as the best method for an all-sky GRB search in the TeV range.

1.1 Overview of High-Energy Astrophysics

The earth is constantly bombarded by many kinds of cosmic radiation (or particles) ranging in energy from 1 eV to 10^{20} eV! Only by detecting this radiation, are we able to accumulate evidence and eventually to explain many astrophysical phenomena. Take a low energy source as an example; astronomers are not able to directly check *in situ* the processes happening in the sun for obvious reasons. Nevertheless, by just detecting its radiation, the sunlight, we can still come out with a profound understanding of the emitting source.

1.1.1 Charged Particles

Other than photons and neutrinos, most cosmic rays are electrically charged particles. Before a charged particle (e.g. proton) reaches the earth, its trajectory is bent by the intragalactic ($\sim \mu$Gauss) and intergalactic magnetic fields. These fields are complicated as they have both dipole and random components. Thus, by the time the particle is detected, we have no information regarding to its origin. Some numbers here will illustrate the scale of the effect.

The bending radius of a charged particle in a magnetic field is: $R = 0.01 \times (p/zB)$, where the momentum p is in TeV, the magnetic field B is in μGauss, the charge z is in units of the electron charge, and the radius R is in parsecs. One parsec (pc) is equal to 3.26 light year. The disk of our galaxy is about 30 kpc in diameter. According to this formula, a proton, with energy as high as 10^6 TeV, coming from a source inside our galaxy and at

10 kpc, is seen to have a bending radius $R = 10$ kpc. It bends 90 degrees by the time it reaches the earth.

Charged cosmic rays have been detected since the 1920s. They come from all directions and form an isotropic cosmic-ray background. The highest energy of detected particles exceeds 10^{20} eV.[2]

It is remarkable that these particles can be accelerated to such huge energies. Many theoretical ideas, such as the shock front model (Bell, 1978), and a model where the particles are accelerated by the strong electric fields around neutron stars and accretion disks (Chanmugam & Brecher, 1985), have been proposed to explain the acceleration mechanisms.

It is also interesting to examine the identities of charged cosmic rays to see if they are protons, helium nuclei, iron nuclei, and so on. Therefore, we study the relative abundance among different species. However, without knowing where these particles come from, it is difficult to interpret the data. Imagine that all the visible photons from the sun were randomly scattered by the earth's atmosphere before reaching our eyes, so that all we see is a homogeneous blue sky without a particular intense spot (the sun). It would be very difficult, if not impossible, to deduce what we know about the sun today.

In order to be more useful and interesting, cosmic radiation must be able to be traced back to its origin. In other words, it has to be electrically neutral as well as stable enough to survive the travel times needed from the sources to earth.

A free neutron decays into a proton in about 10 minutes. Even if somehow there is a way to accelerate a neutron to extreme energy, a TeV (10^{12} eV) neutron can still only live for a week in the earth's rest frame. It will lose its identity and decay to a charged proton before it arrives, unless it is from the sun. The energy of all radiation (or particles) from the sun is too low to be detected by this study.

1.1.2 Neutrinos

Neutrinos are stable neutral particles. Many celestial objects emit neutrinos as long as there are relevant high-energy processes going on in the objects. Despite the fact that there is a large flux, neutrinos are notoriously difficult to detect since they only interact via weak forces and the cross sections are tiny.[3] Nevertheless, modern neutrino projects have been playing major roles in astrophysics and proven fruitful. Basically, large detectors are built deep underground (or in the ocean, ice, etc.) with vast overburdens above them. The heavy overburdens are there to shield the detectors from all signals from above, mainly cosmic rays and muons which penetrate material. These detectors are set up to look for rare upward-going muons generated via weak interactions from cosmic neutrinos, which have penetrated through the entire volume of earth from the other side of the planet. Among others, the IMB (Irvine, Michigan and Brookhaven) collaboration, which ended in 1991, detected neutrinos from the direction of supernova SN 1987a (Reines, 1989). The ongoing project, Super-Kamiokonde in Japan, featuring a giant underground cave and filled with ultra clean water, is a large cosmic-neutrino detector. When an up-going muon travels

[2]At this extreme energy, if the particle is electrically charged, from the formula above its bending radius is now $R \sim Mpc$, much bigger than the size of our Galaxy. In case the source resides in our Galaxy, the trajectory is therefore not bent much and the source can be located near the apparent incident direction.

[3]Because of their small cross sections, neutrinos can get out of the material around their sources as well as penetrate the intragalactic dust.

through the volume of water in the detector at relativistic speed, optical Čerenkov photons are generated along the muon track. These photons are in turn detected by photo-multiplier tubes (PMTs), placed around the underground hole. Another experiment at the south pole, AMANDA, which is even larger than Super-Kamiokonde, arranges PMTs inside the solid ice a few kilometers below the surface. Similarly, when an upward-going muon goes through the ice, it generates Čerenkov light (photons).

After a secondary upward-going muon is reconstructed with its track and is accepted as a valid candidate, the original direction of the primary neutrino can be estimated if the muon is sufficiently energetic.

1.1.3 Photons

In the entire subject of astronomy and astrophysics, no one will question that the most obvious and by far the most important stable neutral particles are photons. Astronomy started with observing objects in the optical range of the electromagnetic spectrum. Photon sources, such as the sun, the moon, inner planets and stars were located on the first day human beings existed. After optical lenses were invented, some remote planets, star systems, and galaxies were found. From the studies in the optical wave band, we are able to investigate the nuclear processes going on in the sun and understand the evolution of stars. For a purely thermal process (i.e., black-body radiation), the emitted photon spectrum is determined by its surface temperature. By fitting the spectrum of optical sunshine with the known thermal formula, we found the temperature of the sun to be 6000K, which in turn constrains the sun's internal processes. In addition, we can estimate the distances from earth to many astronomical objects by observing the redshift of distinctive line spectra in the optical range. Also via the help of this technique, we can conclude that the universe is expanding.

As technology has improved and new instruments have entered the field, we have been able to detect electromagnetic photons outside of the optical band. We have extended our observations of the electromagnetic spectrum in both directions many orders of magnitude. It is fair to say that the history of astrophysics (or astronomy) is made with accumulated explorations in the electromagnetic spectrum from one energy region to another. This is similar to the path taken in physics where as we move up one order of magnitude in energy, new physics is likely to be revealed. Although we cannot control astronomical sources (and processes) as we can do with accelerators, desired environments (initial setups) can always be found via extensive searches in the vast universe. Many crucial discoveries, which are to be described in this section, firmly support the assertion — a new energy range results in some new astrophysics.

Ultraviolet-band astronomy became practical as observations from above the atmosphere materialized (e.g., high-flying balloons). Strong emissions from resonance transitions, among a wide range of common elements (ions and atoms), fall in the ultraviolet spectral region. This provides a valuable diagnostic tool for the astrophysics of sources.

After we were able to detect infrared-band photons, we could see and study many cool objects in the temperature range of 1-3000K. In addition, there is much interstellar dust inside our galaxy, which occupies some patches and blocks the view of optical observations. Fortunately, this dust looks transparent to infrared light; therefore, infrared-band observation supplies deeper sky information behind many of the optically opaque spots.

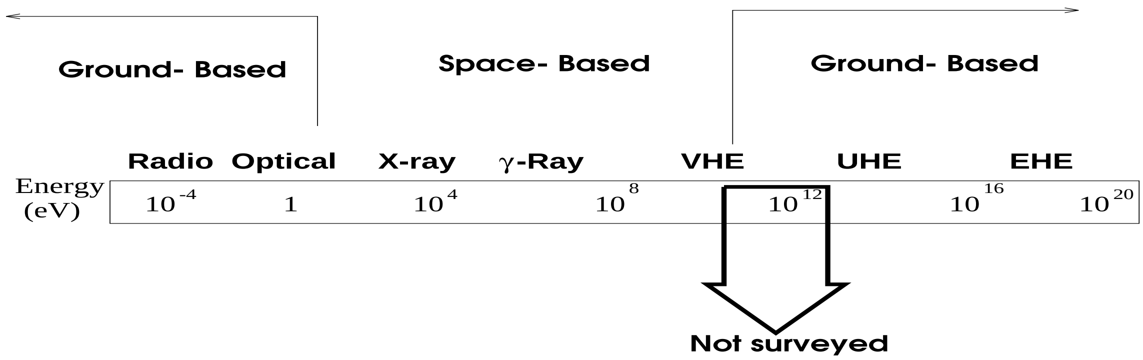

Figure 1.1: The electromagnetic spectrum in terms of energy. The suitable observation methods among different energy regions are also shown (the infrared region before optical band is better determined by space-based instruments). The energy between 100 GeV and 1 TeV is the target range in this study.

During the 70s, many dedicated x-ray satellites were launched and made many important discoveries. Some binary star systems, such as Cygnus X-3, were found to be pulsating and soon were identified as rotating neutron stars. The source of x-rays from Cygnus X-3 is actually the in-fall of matter transferred from the primary star — a process called accretion. The masses of invisible secondary partners in a few x-ray sources, similar to Cygnus X-3, are greater than the upper limit for stable neutron stars, making them candidates for black holes.

Unlike ultraviolet, infrared, or x-ray, radio signals from the sky are not heavily absorbed by our atmosphere. As radio technology and electronics improved, large dish antennas or arrays of antennas were set up and detected numerous radio sources. Millimeter radio wave band observation detected the homogeneous microwave background photons, and these photons fit the cold 2.736K black-body radiation spectrum perfectly supporting the Big Bang theory.

Another major achievement in radio astronomy is the discovery of pulsars. Pulsars were soon identified conclusively as rotating and magnetized neutron stars. The pulsar observation provided the first definite proof of the existence of these high density objects. Among others, the pulsar found inside of the Crab Nebula, which is the remnant from a famous recent supernova explosion, has a great deal of interesting astrophysics throughout all energy bands.

Many strong radio sources, which reside in other galaxies and are far away from our own galaxy, were found to be supermassive objects with giant radio lobes. The central point-like sources are called the active nuclei of the galaxies or active galactic nuclei (AGN). After two decades of observations, a successful model of AGN has emerged and is accepted by many people within the community (Begelman & Rees, 1984). This model asserts that the central engine of an AGN contains an extremely heavy black hole with its mass between 10^7 and 10^{10} solar masses![4] Energy comes out of an AGN in two narrowly-beamed jets in the directions of the magnetic poles. The nature of the detected radiation from AGNs depends heavily on the orientation of the beams relative to the earth. This orientation

[4]For comparison, our galaxy has about 10^{11} stars.

dependence causes the proliferation of classes and sub-classes of AGN — quasars, blazars, Seyfert galaxies (Types I and II), radio quiet/loud galaxies, Fanaroff-Riley galaxies (Types I and II), narrow line, broad line, no line, highly polarized line, flat spectrum, steep spectrum, optically violent variables, BL Lacs, and so on! Quasars (quasi-stellar radio sources) and many other AGNs are at great cosmological distances, which provide important diagnostic tools for cosmology. In addition, recently AGNs were discovered to emit radiation over a broad range in the electromagnetic spectrum from radio waves to TeV gamma rays. Because AGNs are far away (at least extragalactic), we can conclude from the detected flux on earth, as for GRBs, that the emitting power in the central source of an AGN is enormous, even considering that they can be narrowly collimated. Currently, AGNs and GRBs are two of the hottest topics in astrophysics. Because AGNs are steadier sources than GRBs, the study of the spectra of AGNs in the GeV to TeV range will help in calibrating the distances of GRBs for reasons described in Section 1.5.

The issue of the distance of GRBs and the issue of γ-ray absorption are the key points of this entire study.

In 1977, a balloon observation made in Australia detected a γ-ray line emission at 0.511 MeV from the direction of our galactic center (Leventhal, 1978). The γ-ray apparently resulted from the process of e^+e^- annihilation. This started the high energy gamma-ray astronomy. When its energy exceeds 10^5eV (see Figure 1.1), a photon is characterized as being in the γ-ray wave band. Because γ-ray covers all the way up to the highest energy, the name γ-ray is no longer descriptive enough and needs to be sub-categorized. There are some conventional terminologies to further characterize the different subdivisions:

HE (High Energy) .... 30 MeV – 30 GeV
VHE (Very High Energy) .... 30 GeV – 30 TeV
UHE (Ultra High Energy) .... 30 TeV – 10 PeV (10^{16} eV)
EHE (Extremely High Energy) .... > 10 PeV.

These convenient abbreviations will be used throughout this study.

Encouraged by the early success of x-ray satellites, the research community has launched many γ-ray satellite detectors over the years. The most recent, and the most important, one is the Compton Gamma Ray Observatory (CGRO). CGRO has been flying and taking data since 1991 and it will remain in service until around the year 2000. There are four different types of instruments implemented on CGRO (see Figure 1.2) — Burst and Transient Source Experiment (BATSE), Energetic Gamma Ray Experiment Telescope (EGRET), Compton Telescope (COMPTEL) and Oriented Scintillation Spectrometer Experiment (OSSE). Here, only BATSE and EGRET are described in some detail.

1.2 BATSE

Since it began operating in 1991, BATSE has been the leading detector in the field of gamma-ray bursts. BATSE detectors are designed to be able to detect x-rays and γ-rays from 20 KeV to 2 MeV closely spaced in time.

As seen in Figure 1.2, BATSE consists of eight identical detector modules at the eight corners of the satellite. Figure 1.3 shows that each of these 8 modules consists of two parts, a spectroscopy scintillator (lower part of the module) and a 1.27 cm (in thickness) $\times$ 2025 cm^2 (in area) NaI crystal. The crystal is covered by a thin plastic scintillator in front

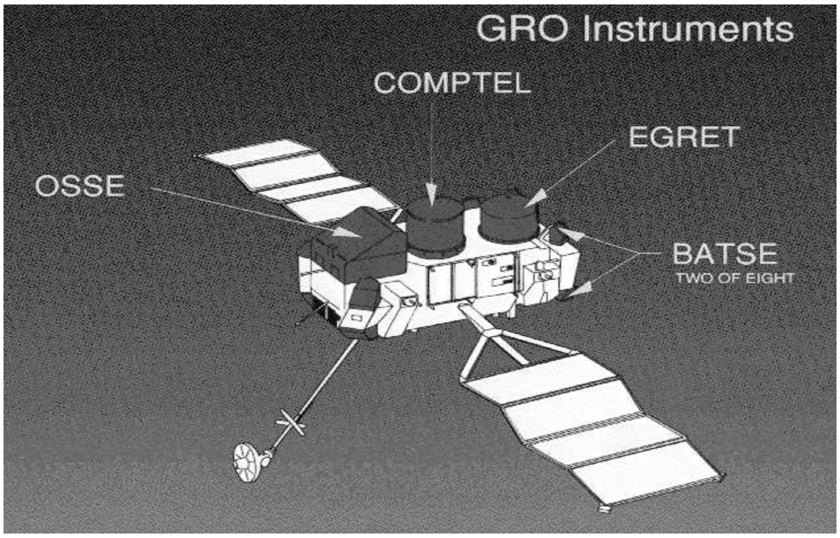

Figure 1.2: A sketch of the Compton Gamma Ray Observatory (CGRO,1998).

to reject charged particles.

BATSE determines the direction of a GRB by comparing the count rate among adjacent modules. The angular resolution for GRBs ranges from 14° for the weakest burst to about half a degree for the strongest burst. Because of its geometry layout of the eight modules, BATSE covers a large fraction of the sky[5] ($\sim 2.6\pi$) to search for GRBs. Inside each module, the number of counts caused by a burst is recorded in 128 energy channels and on three different time scales (64 ms, 256 ms and 1024 ms). The data are then combined into four broader energy bands, 25-50 KeV, 50-100 KeV, 100-300 KeV and $>$ 300 KeV. The BATSE trigger condition changes from time to time. As an example, when the number of counts between 50- 300 KeV, recorded by two or more of a group of 4 modules on any of the three time scales, is greater than 4.5 standard deviations above background,[6] the data is recorded.

Over the past seven years, BATSE has unambiguously detected more than two thousand GRBs, or an average of one GRB per day. Figure 1.4 shows the sky map of the result from 2,000 GRBs. It is isotropic and there is no enhancement in the galactic plane (the equator in the plot), strongly suggesting that GRBs happen outside of our galaxy.

In early 1997, the Italian-Dutch x-ray satellite Beppo-SAX which has directional accuracy of order of 10 arc minutes in observation, first reported detections of a GRB counterpart in the x-ray wavelength (Costa, 1997).

Since then, many observations of GRB counterparts have been made from Beppo-SAX, the Hubble Space Telescope (HST) and other ground-based experiments at x-ray, optical and radio wavelengths.

In particular, the HST observations of GRB 970228 in two photometric bands confirmed the association of GRB 970228 with a possible host galaxy and showed that

[5]BATSE's low orbit limits its coverage from 4π, since the earth blocks a big portion of sky.

[6]In fact, EGRET and COMPTEL can be triggered on BATSE as well. Most BATSE information can be obtained from BATSE's home page at http://cossc.gsfc.nasa.gov/cossc/BATSE.html.

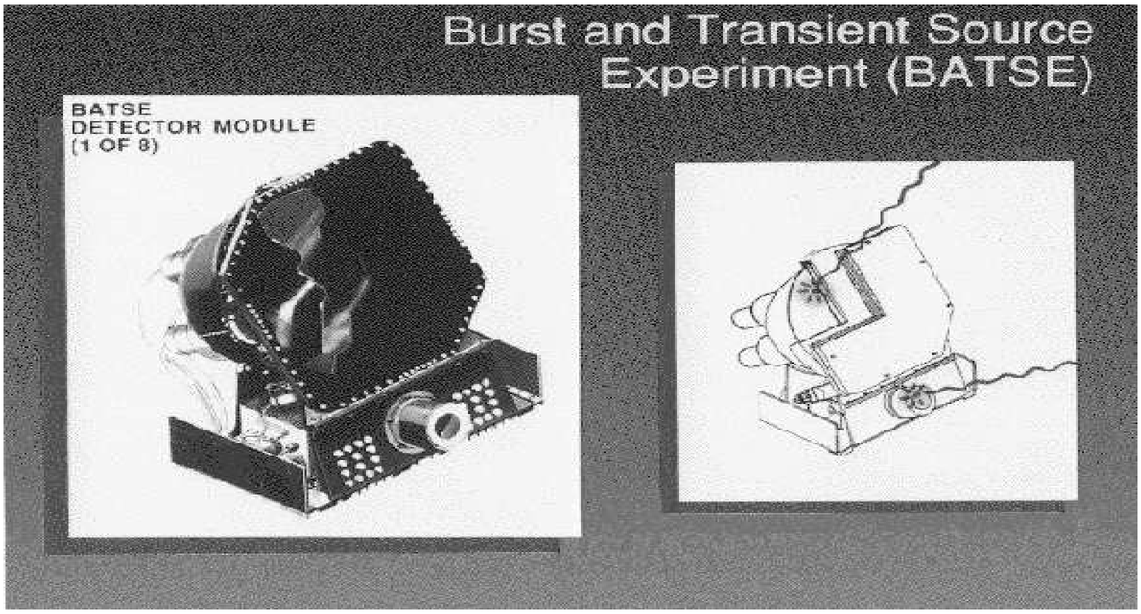

Figure 1.3: A sketch of the BATSE detector (BATSE-Figure,1998).

the GRB is situated off-center in the galaxy (Sahu, 1997a).[7] This suggests that GRBs are probably not related to the nuclear activity of the galaxy. The observations taken more than 200 days after the outburst showed no movement of the GRB, no fading of the extended component, and confirmed that the optical decay behavior continued until such late times. This places strong constraints on the energy of the gamma-ray burst, and further suggests a cosmological origin of the gamma-ray burst. The HST observation of GRB 970508, on the other hand, did not reveal any host galaxy, but a redshift $z = 0.835$ was observed from an absorption line system in the optical spectrum (Sahu, 1997b). The fact that the absorption line faded away suggests that this is the redshift of the GRB source. A redshift value of 0.835 is equivalent to a distance of order a gigaparsec.

More observations are needed before a generalized conclusion can be drawn for all GRBs that they are at cosmological distances. However, the success of discovering GRB counterparts in the low energy end encourages the search for GRB counterparts in the high energy range as well.

1.3 A Model for Gamma-Ray Bursts

There are many theoretical models explaining GRBs, ranging from cosmological origin schemes such as white holes, and superconducting cosmic strings, to galactic origin scenarios such as anti-matter comets, flares on nearby stars and even relativistic dust grains in the solar system! This section will discuss only one of the most popular models, one with a cosmological origin. It is known as the "cosmological fireball" model.

The fact that the time scale of many γ-ray bursts is as short as $\sim 10^{-3}$ second limits the size of the burst emission area r to smaller than the distance light can travel in

[7]HST has superb angular resolution in the optical wavelength.

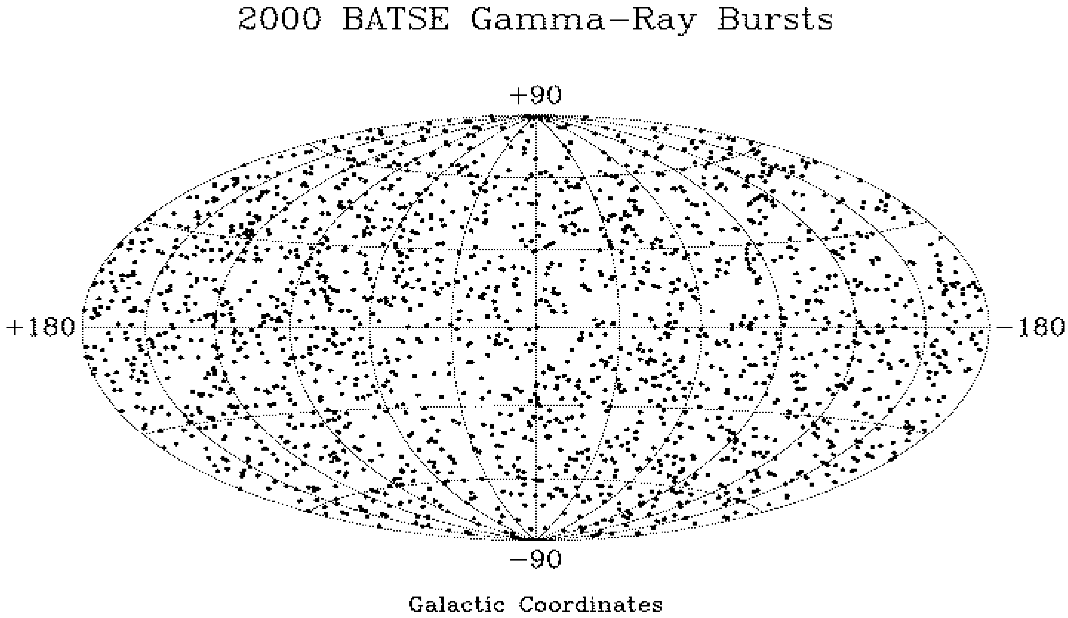

Figure 1.4: A BATSE GRB location map for 2000 bursts (BATSE-Map,1998).

that time, or $r \sim 300$ km. If the emission area were larger, the different light travel times from source to observer would smear out the observed nature of short-time variation.

This constraint poses a problem because γ-rays would not escape from such a compact region, but would run into other γ-rays and make electron-positron pairs. A solution to this problem was proposed by Mészáros, Rees (Mészáros & Rees, 1993) and others and it is now widely accepted. According to this model, the production of a GRB occurs in two stages: first, a directed beam of relativistic matter, or the "jet," is produced by a central engine with a duration less than that of the GRB, and second, this "jet" travels to large distance ($\sim 10^{13}$ m) and produces gamma-rays by a shock interaction with circumstellar or interstellar matter.

Thus, the region where γ-rays are generated is big enough so that they can escape freely. However, now the time for light to cross the source region is $\sim 10^3$ seconds. There is a way to solve this problem — if the jet is moving very fast along the direction of the observer on earth, the observed variability timescale can be shorter than the emission timescale in the source. The proportionality is governed by $1/\Gamma^2$, where Γ is the Lozentz factor. To keep the GRB's time scale within a second, Γ needs to be at least 100. That is, each baryon in the jet has to have at least 100 times its rest mess in kinetic energy. This deceleration mechanism of ultrarelativistic matter provides the only known solution to the compactness problem. The kinetic energy of the ultrarelativistic matter is converted into internal energy by relativistic shocks. These shocks can be either due to the interstellar medium (ISM) ("external shocks") or shocks inside the shell itself due to nonuniform velocity ("internal shocks") (Kobayashi, 1997).

A possible central engine for the source of the relavisitic jets is a black hole accreting matter. The angular momentum of the accreting matter causes it to accumulate in a torus. This torus rotates differentially, i.e., the inside goes around faster than the outside. As one part of the torus slides across the other, friction leads to heating and angular momentum transport. Some of this energy is carried into the black hole, while the rest is radiated as neutrinos. The rotating ionized torus also contains a strong magnetic field.

The source of the jet is the neutrino emission, and the energy carried in neutrinos is typically the accretion rate times an efficiency factor of about 0.1 Mc^2. Therefore, an accretion rate of 0.1 solar mass per second gives a neutrino luminosity of over 10^{52} erg/s. 10 solar masses per second (e.g. the black holes eats up a massive neutron star) gives a neutrino luminosity of 10^{54} erg/s.[8]

These neutrinos meet their anti-particles along the rotational axis of the black hole. They react to make electron-positron pairs and γ radiation. This energy plus the matter that happens to be in the vicinity expands to make the jet. The efficiency for converting neutrino energy to jet energy ranges from 1% to smaller values. The higher the accretion rate the greater the efficiency. Merging neutron star-black hole pairs can make jets with energies of 10^{51} erg this way.

This model can explain most GRBs in the energy range of BATSE and EGRET. However, for bursts with possible extreme redshifts (for example, $z > 3$), the model has to make room to come up with GRB output energies up to 10^{54} erg. Also, it does not address the energy range of TeV, which is the main interest of this study.

1.4 EGRET

The EGRET instruments provide the highest energy gamma-ray detection on the satellite CGRO. It is larger and more sensitive than any previous detector operating at these high energies. Since the launch in 1991, EGRET has made valuable observations of high energy processes associated with diffuse gamma-ray emission, gamma-ray bursts, cosmic rays, pulsars, and AGNs.

With a complete *veto* of charged particles, the EGRET detector accepts γ-rays in the energy range between 30 MeV and 30 GeV.[9] As shown in Figure 1.5 , an incoming hard γ photon interacts at the upper part of the detector (many thin tantalum foils inside the spark chamber) and converts to an electron and a positron. They travel through a time-of-flight coincidence system, before these two electrons are eventually stopped by a Total Absorption Spectrometer Crystal (TASC). The directions of these two electrons can be accurately measured from the tracks in the spark chamber, and their energies can be found from those deposited in the TASC. In the end, the direction and energy of the original γ-ray can be well reconstructed.

The EGRET instrument has good angular and energy resolution when the energies of γ-rays are greater than 100 MeV.[10] After detecting many photons from a given source with a fixed location, EGRET can determine the energy spectrum from that γ-ray source.

Compared to BATSE, EGRET has a much smaller field of view, only 0.25π because, as shown in Figure 1.5 , it has only one detector and is collimated. Nevertheless, as seen in Figure 1.6 , EGRET has successfully done an all-sky γ-ray survey above 100 MeV

[8] The mass of sun ($\times c^2$) is 1.8×10^{54} erg.

[9] In fact, the conventional nomenclature of HE was meant to match the energy range of EGRET.

[10] For example, the FWHM of energy resolution at 100 MeV is 26% and the FWHM of angular resolution is 5.5°. At a higher energy of 1 GeV, the energy resolution improves to 19% and the angular resolution is 1.2°.

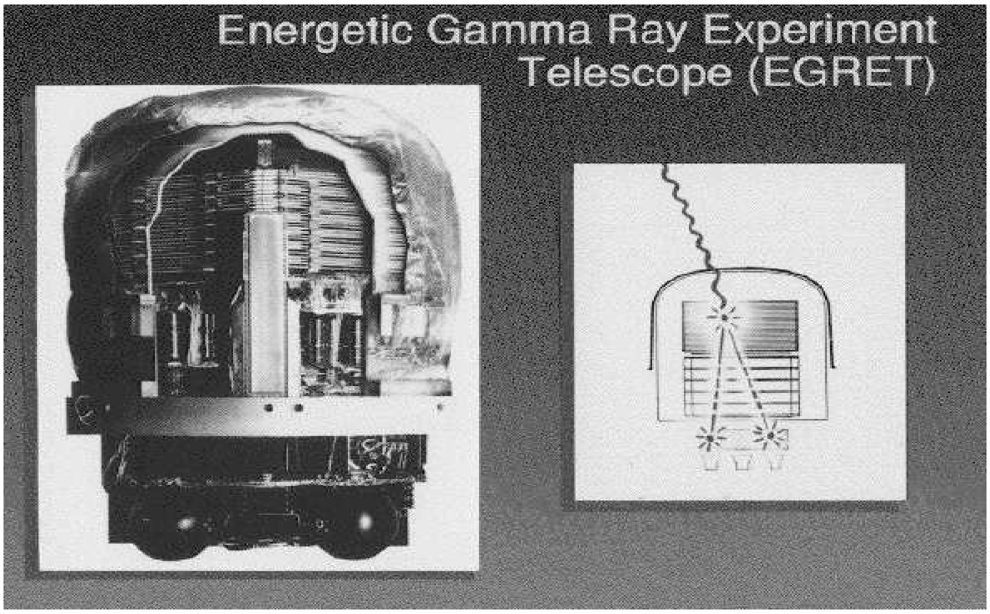

Figure 1.5: A sketch of the EGRET detector (EGRET-Figure,1998). The figures are described in the text..

with an excellent statistics.[11] The image in Figure 1.6 , plotted in a galactic coordinate viewed from the earth, shows the γ-ray intensity from every spot in the sky. Unlike the isotropic GRB sky map, the obvious middle band, with higher γ intensities, is accumulated from all γ-ray sources from the direction of the galactic plane. These diffuse γ-rays mainly come from the decay of neutral pions, which are generated in collisions between the nuclei of atoms (and molecules) of the interstellar gas and cosmic ray protons and nuclei.

On the same figure, there are some discrete sources away from the galactic plane. Naturally, there should be many more discrete sources embedded in the galactic plane which cannot be distinguished on the figure. Among these discrete HE γ sources are the Crab pulsar (in the plane) and AGN Mrk421 (out of the plane). The flux, as well as the energy spectrum, of the Crab pulsar have been well measured in the HE domain by EGRET and the flux is time correlated with the pulsar's characteristic 33 millisecond period. The Crab pulsar is one of the few objects we know that emits energy in all bands: radio, optical, X-ray, γ-ray, HE and VHE regions (see Figure 1.7).

With the help of BATSE's trigger, EGRET not only detects the existence of GRBs in the HE domain (up to 18 GeV), but also can measure the energy spectra of some GRBs. BATSE itself cannot determine the energy spectrum of a GRB well since the instrument has only four energy bins. As an example, the following two GRBs on BATSE's list, which will be referred to many times in this study, have their spectra measured by EGRET: (1) BATSE GRB 4B 940217, which lasted for 90 minutes after the main BATSE trigger, and

[11] Most EGRET information can be obtained from EGRET's home page at http://cossc.gsfc.nasa.gov/cossc/EGRET.html.

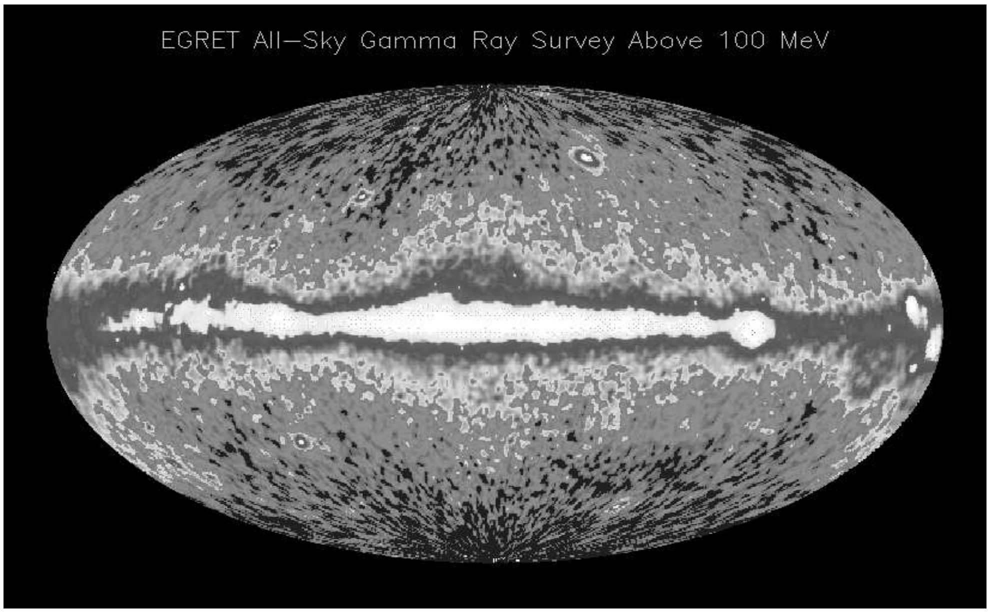

Figure 1.6: The all-sky map of detected high-energy gamma rays from EGRET (EGRET-Map:1998).

had a spectrum given by

$$\frac{dN}{dE} = (2.91 \pm 0.97) \times 10^{-7} (\frac{E}{128MeV})^{-2.08 \pm 0.56} \ photons \ cm^{-2} \, s^{-1} \, MeV^{-1} \qquad (1.1)$$

(2) BATSE GRB 4B 930131 (Sommer, 1994), which lasted for 25 seconds after BATSE's main trigger, with a spectrum given by

$$\frac{dN}{dE} = (7.4 \pm 1.8) \times 10^{-6} (\frac{E}{147MeV})^{-2.03 \pm 0.36} \ photons \ cm^{-2} \, s^{-1} \, MeV^{-1}. \qquad (1.2)$$

The second one, with very strong emission and a recorded 1 GeV photon among other hits, is called the "Super Bowl" burst.

EGRET provides very little information on the spectrum above 1 GeV for two reasons: (1) there is no energy information above 30 GeV because of the detector's energy ceiling, (2) the flux, following $\frac{dN}{dE} \propto E^{-2}$, drops fast and there are not sufficient events in the high energy region to allow a spectrum measurement. Take the Crab flux as an example. Even with a satellite detector as big as a football field, we would only expect one photon at 1 TeV in an hour. Considering EGRET has an area of only 0.5 m^2, we see that space-based experiments are reaching their limits when the energy is above 100 GeV.

1.5 CYGNUS Air-Shower Array

To go to higher energies, we need a detector with much bigger area than we could put in a satellite. At high enough energies, γ-rays can penetrate the atmosphere, so we can set up a large detector on the ground. The CYGNUS air shower array, located at

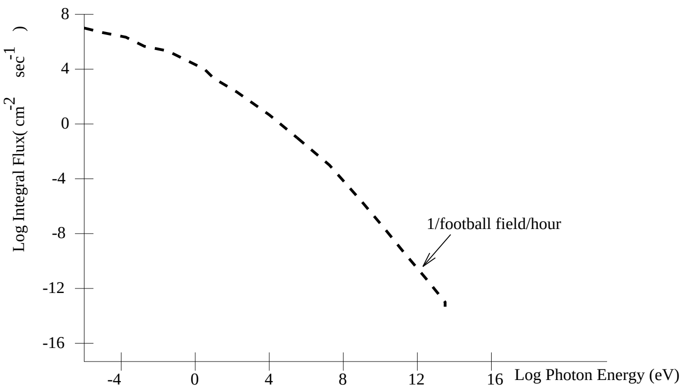

Figure 1.7: Integral photon flux from the Crab nebula.

Los Alamos, New Mexico, at an altitude of 7,500 feet, is a good example of an air-shower technique. The experiment will be described in some detail to show the idea. This section will be referred to constantly in later chapters, not just because the air-shower methods are nearly identical to that of the Milagro experiment, but also because many ideas and much of the work in this study, such as the Monte Carlo simulations, the data reconstruction techniques, physics motivations, and data analysis methods actually originated in the CYGNUS project.

Our atmosphere prevents cosmic radiation from reaching the ground without interacting. At sea level, the air overhead is equivalent to 20 cm of lead, or in a more convenient unit, 37 radiation lengths (29 interaction lengths)[12] , spread out over 100 kilometers. That is to say, the probability of a high-energy γ ray not interacting before it reaches the ground is in the order of e^{-29}. The way it interacts with air can be best described with an example. As shown in the middle bundle of the drawing in Figure 1.8 , a 50 TeV (UHE) γ -ray enters the atmosphere and splits into two electrons, typically in the first radiation length of atmosphere (the vertex occurs at about 25 kilometers above sea level). Then these two electrons emit bremsstrahlung photons in the second radiation length of air. The two new-born bremsstrahlung photons, in turn, split into four electrons via pair production by the end of the next radiation length. Therefore, at the bottom of the third radiation length of atmosphere, which is about 18 km above the sea level, the original γ -ray has converted into six secondary electrons and two secondary photons. This development is called the generation of an extensive air shower (EAS). As long as they have enough energy, these secondary particles will continue to break into more daughter secondaries and the EAS grows. However, the primary particle, the original 50 TeV γ -ray, no longer exists. Nonetheless, just like in the cases of neutrino experiments described earlier, the properties of the primary γ-ray can be reconstructed from information carried by its secondary particles which are detectable when they reach the ground.

Not every secondary particle can reach the ground, though. Those with less energy will be stopped by the air without further splitting. An EAS reaches its shower maximum

[12]The unit of radiation length is defined as the distance over which the electron energy is reduced by a factor of $e^{-1} = 0.37$ due to radiation loss, or bremsstrahlung, only. On the other hand, the interaction length of an energetic photon is defined as the distance over which it has 63% of probability to interact with air. In this case, interaction length is equal to $\sim \frac{9}{7}$ of radiation length.

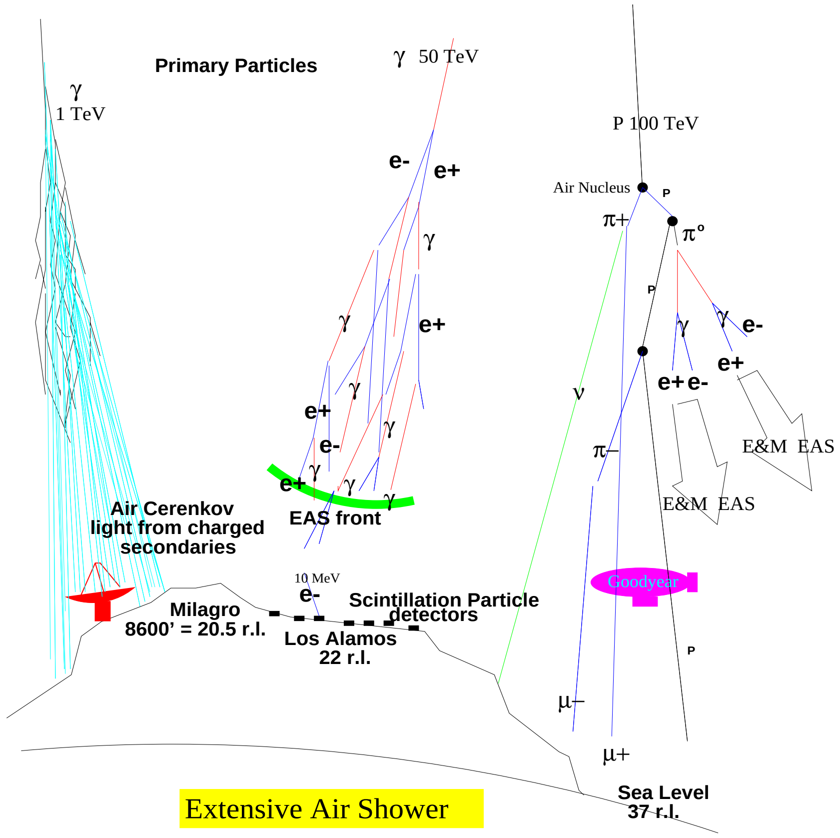

Figure 1.8: Conceptual drawings of extensive air showers.

when the number of secondaries reaches its maximum. After reaching the shower maximum, a rather low energy EAS will die out before its secondary particles are able to reach the ground. The shower maximum and other EAS properties will be explained again quantitatively in Chapter 3. A 100 TeV γ EAS reaches its shower maximum as high up as 14 r.l. (refer to Figure 3.2). On average, a less-energetic 500 GeV γ EAS will have no secondary particles reaching sea level. When it comes to the design of an air shower detector, the rule of thumb is always try to set up a ground-based experiment at as high an elevation as possible in order to detect shower secondary particles before they die out.

CYGNUS's altitude, 7,500 feet, was equivalent to 22 r.l. of air overburden. The array contained 108 plastic scintillator particle detectors (see Figure 1.9), separated from each other by 15 to 20 meters, and covered an area of $22,000\,m^2$. Each light-tight cone-shaped detector, wrapped in a 0.25 cm of lead sheet, had a slab of plastic scintillator at the bottom 10 cm thick and a 2" fast PMT hanging up-side-down at the top. The array took data around the clock and covered the sky from vertical to $\sim 50°$.[13] CYGNUS had been detecting air showers since 1986 before it was finally disassembled in 1996 to facilitate the next-generation Milagro detector.

[13]The energy needed to penetrate the atmosphere increases with the zenith angle because the air shield is thicker for an inclined air shower than a vertical one. Above $\sim 50°$, the energy gets very high and there are practically no CYGNUS triggers, due to the steep energy spectrum of cosmic rays.

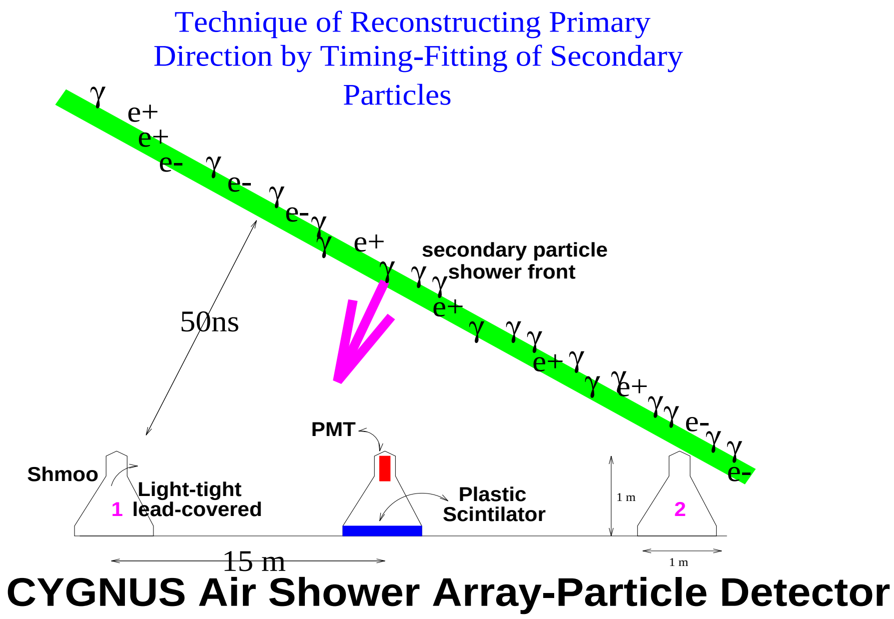

Figure 1.9: The CYGNUS air-shower counters and the direction reconstructing technique.

As sketched in Figure 1.8 and Figure 1.9 , the "front" of an air-shower moves downwards at nearly the speed of light and this front actually consists of shower particles. As this pancake-like shower front of an EAS passes through the detector, a small portion of its secondary particles are sampled by these counters, and both their particle counts (in terms of PMT pulse heights) and times are recorded. Given the fact that all (x,y,z) locations of counters are known, as is the speed of light in air (0.3 m/ns), we can derive the original EAS's direction from the timing differences among counters. From Figure 1.9 one can see intuitively that the shower direction is determined by the plane containing all the shower secondaries. Chapter 4 will describe how to fit the plane in detail.

A charged-particle primary, such as a proton, can also interact (see the shower to the right in Figure 1.8) with air nuclei and it generates a hadronic air shower. As shown in the drawings, the generated π° can decay to two γs and in turn account for the electromagnetic secondary particles in a hadronic air shower. The first interaction position takes place, however, lower than that in the γ primary case, because the "interaction length" between proton (at 1 TeV) and air nuclei is $83\,g/cm^2$ (Gaisser, 1990), which is larger than the γ interaction length in air ($\frac{9}{7} \times 36\ g/cm^2$). Also, in the process, some muon and hadron secondaries are generated, which are not present to the same degree in those of γ showers.[14] Other than the presence of secondary muons and hadrons, there is not much difference to first order, as far as the detector is concerned between a γ primary and a proton primary.

As explained earlier, charged particles form an isotropic cosmic-ray background. After we reconstruct the original directions of all air showers, signals (γ primaries) from a source will be buried amid a sea of cosmic-ray background events since charged particles are far more numerous than γ's (1000:1). This does not happen to EGRET or BATSE,

[14]The cross-section for the inelastic γ–p interaction is three orders of magnitude smaller than that of p–p with the same center of mass.

because their instruments can reject charged particles at the beginning. This intrinsic similarity between signal events and background events is a major drawback for ground-based experiments. To help identifying background showers, we can build extra muon or hadron detectors along with the main air-shower detector to reject some background events.

Having the wanted signals (or data) buried among background events is a common problem in many fields in physics and astronomy. Fortunately, signals always pile up around a fixed point since they are supposedly biased by certain underlying influences, while background events are random. After enough events, the signal stands out. For example, we have no problem picking up the direction of the sun from the homogeneous blue sky, because the signal photons add up at the spot where the source, the sun, is. Of course, the intensity of photons from the direction of the sun is much larger than the intensity of photons from any random direction in the blue sky. However, the concept is the same, except that in real experiments, the expected signal intensity is much weaker and is comparable to that of the background.

The next concern in locating the source is how sharp the focus is, or equivalently, how good the angular resolution of the detector is. As an imaginary example, in the primitive eyes of a fly, it probably sees a sun "spot" 10 times bigger than what we see. We say that its vision has poor angular (image) resolution. Nevertheless, it still concludes that the center of the blurred chunk it sees is the correct direction of the sun.

While a quantitative definition will be given in Chapter 5, the angular resolution of the ground-based detector is a measure of how good the agreement is between the reconstructed direction of an EAS and the true direction of the original primary particle. Better angular resolution is crucial since it pulls all signals into one sharp spot and enhances the signal to background contrast.

The CYGNUS detector achieves an angular resolution of $\sim 0.8^\circ$ for all its shower events. After the CYGNUS data were analyzed for emission from BATSE's GRBs (Schnee, 1996), there was no evidence found for signals.

The problem is that the energy required to trigger the CYGNUS array is too high, despite the detector's high altitude. The median energy of triggered primaries in CYGNUS is around 100 TeV.[15] Out of the few times 10^8 reconstructed showers from CYGNUS data, there is no evidence for a steady γ-ray source with $E > 100$ TeV. The energy may simply be too high as there may be no γ-ray source with that kind of energy at all.

Here we have to address an important issue in the field of high-energy γ-rays — the possible absorption of γ-rays via interacting with other soft photons en route to the earth. In Figure 1.10, the mean free path, as a result of various absorption sources, of an energetic γ-ray is plotted against its energy. According to these curves, if a γ-ray source exists at a distance of 100 Mpc and emits 100 TeV γ-rays towards us, these γ photons will be severely absorbed before they can reach earth. As a result, we do not see the source.[16] Since AGNs are extragalactic HE and VHE γ-ray sources, they fall into this category. As shown in Figure 1.11, the actual shape of the detected energy spectra of AGNs can reveal some information about their distances, as well as the suitability of various theoretical models. In addition, many AGNs have their host galaxies visible in the optical wavelength and thus the distances of these AGNs can be independently determined. This aspect of

[15] The most probable energy of CYGNUS events is 50 TeV.

[16] The diameter of our galaxy is ~ 30 kpc and the distance to the nearby Andromeda galaxy is ~ 1 Mpc.

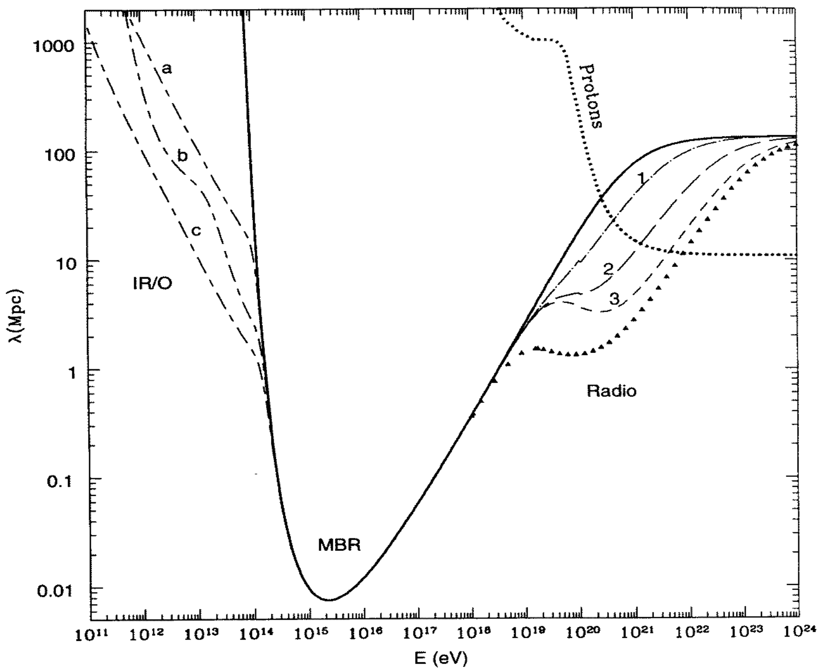

Figure 1.10: Mean free path, λ, for γ-rays of energy E, showing absorption by the various extragalactic backgrounds. The solid line shows the effect of the microwave background radiation (MBR), the dashed curves (a, b, c) show three models of the Infrared/Optical (IR/O) diffuse background, and the dashed curves (1,2,3) and triangles show the extragalactic radio background estimates with cut-offs at 5, 2, and 1 MHz, and upper limits assuming the total observed radio background is extragalactic, respectively. The dotted line shows the mean free path for energetic protons (Coppi and Aharonian, 1997).

opaqueness applies to the photons from GRBs as well. If many different AGNs with known distances have their energy spectra detected, especially over the region between 100 GeV and 1 TeV, these actual AGN spectral shapes can be used to determine the distance of a GRB by matching with the GRB's energy spectrum.

Therefore, the detection of γ-ray bursts in the energy range between 100 GeV and 1 TeV, whether it is positive or negative, gives some crucial input to the important question — are GRBs inside or outside our galaxy? If outside, how far away are they?

Can the CYGNUS detector lower its energy threshold, then? Yes, it can, through lowering its trigger requirement to fewer detectors. However, doing so will degrade the angular resolution since there will be fewer points used in the plane fit for finding the shower direction. Consequently, the sensitivity to signals will drop significantly.

A closer look at the CYGNUS geometry shows that most of the valuable shower secondaries miss the scintillation counters. Only 0.5% of the area is actually active and covered by detectors. If the percentage of active area can be somehow increased, the energy threshold can be lowered without compromising the angular resolution. Of course, it is far too expensive to cover the entire area with solid scintillators.

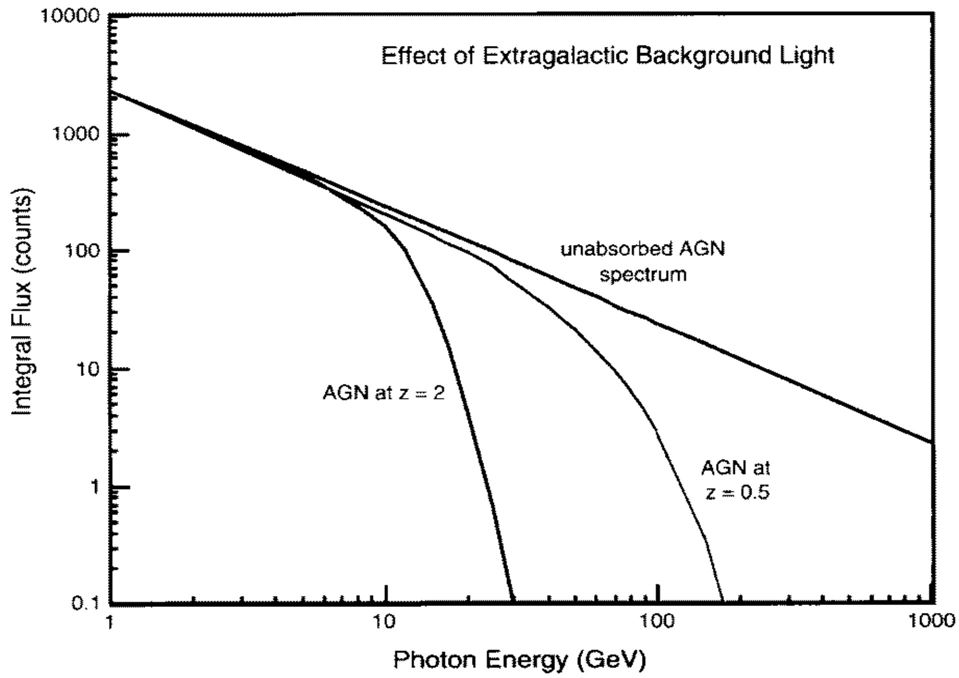

Figure 1.11: Energetic γ -rays emitted by distant AGN can interact with extragalactic background photons before they can reach us. Shown above is how a power-law AGN spectrum would appear if observed at redshifts of z = 0.5 and 2 for a particular absorption model (Norris, 1998).

1.6 Whipple Air-Čerenkov Telescope

The air-Čerenkov telescope is another important type of ground-based VHE γ-ray instrument. When energetic secondary electrons pass through air, their speed exceeds the speed of light in the same medium. As a result, optical Čerenkov photons are emitted along the tracks of secondary electrons and spread towards the ground. We can set up optical mirrors to collect this Čerenkov light as shown in the left drawing of Figure 1.8. In turn, from these by-products of secondary particles,[17] we can reconstruct some attributes, for example, the direction, the energy, or even the identity of the primary particle. The Whipple telescope (Figure 1.12) in Arizona is the leader in the field of the air Čerenkov detection.

Consider a smaller EAS with primary energy less than 1 TeV, whose secondaries, as mentioned earlier, have a difficult time reaching the ground. The shower generates many Čerenkov photons in the upper part of atmosphere and the optical light easily penetrates the thick air and gets collected by the detector. Consequently, the energy threshold drops dramatically without loss of angular resolution. In addition, because Čerenkov photons are emitted at the early stage of the EAS ($\sim$ 10 km) and with an angle of about 1.4° relative to the shower axis, the light pool is spread out in an area much bigger than the size of collector. Thus, the optical light can be detected even if the collector is not sitting

[17]The by-products of the by-products of the wanted primary particle!

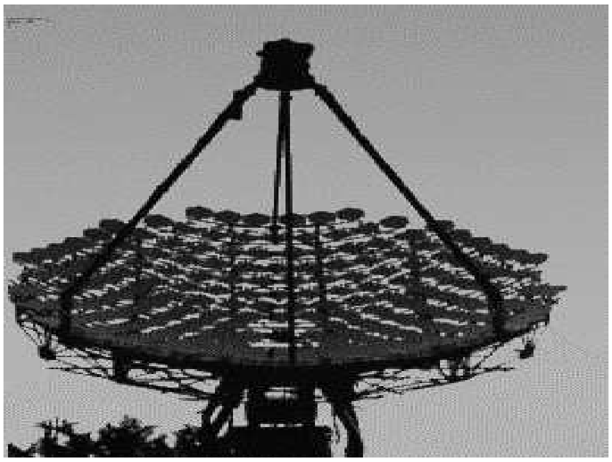

Figure 1.12: The Whipple Air Čerenkov Telescope

near the shower core. As a result, the effective area is bigger than the physical area of the detector, and any primary particle which falls inside the effective area will trigger the detector.[18] Furthermore, the amount of Čerenkov light is proportional to the total track length of the charged secondaries, which is in turn proportional to the total energy of the primary particle. Not surprisingly, the Whipple telescope has very good energy resolution. In addition, the Whipple group developed an algorithm based on the light shape difference in image to reject a significant portion of charged primaries.

Whipple has detected and identified the Crab nebula as a steady γ-ray source in the TeV domain. Several AGNs, have also been confirmed as TeV γ-ray sources by Whipple, although their fluxes can vary from time to time.[19]

There is no doubt that the air-Čerenkov technique is ideal for ground-based HE γ-ray astronomy and will continue to provide major contributions. However, two shortcomings of the air-Čerenkov method exist — short duty cycle and narrow field of view. Air-Čerenkov observation requires a dark (moonless) and clear (no clouds) sky. Whipple actually takes data for less than 10% of the time in a year. Because the detection of Čerenkov light needs an optical instrument with accurate focal point, the field of view for Whipple is narrow and is in fact smaller than 10^{-2} sr. Therefore, Whipple has to choose (or guess) a source candidate beforehand, aim the telescope at it, and hope that it turns out to be a γ-ray source. Under these restrictions, Whipple cannot do an all-sky γ-ray survey and it is very difficult to search for GRBs.

1.7 Milagro Project

After considering the pros and cons of all the methods described, we designed the Milagro experiment, which means "miracle" in Spanish, (see Figure 1.13) as the best

[18]If they all come from near the direction that the mirror is aimed.

[19]In contrast to the Crab pulsar, AGNs, for instance Mrk421 and Mrk501, are not found to be steady TeV γ-ray sources. Instead, their intensities fluctuate irregularly. On the seventh of May in 1996, Mrk 421 had a strong flair seen by Whipple at more than 12 standard deviations above background during the a few hour of the flare (Gaidos, 1996).

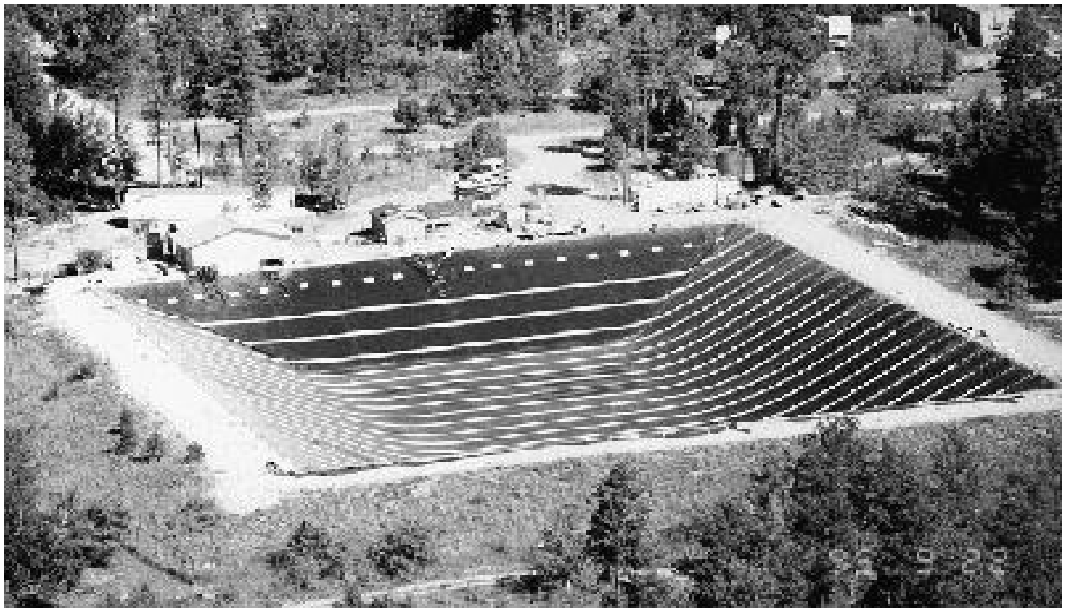

Figure 1.13: An aerial photograph of the Milagro pond.

instrument to explore the energy region mainly between 100 GeV and 1 TeV for both steady sources and γ-ray bursts. As shown in the aerial photograph, the main body of the detector is a large artificial 5 million gallon pond, the size of a soccer field. It is located in a National Forest in Northern New Mexico at an altitude of 8,660 feet (or an air overburden of 20.75 radiation lengths). The $60m \times 80m \times 8m$ pond is to be filled with clean water enclosed by a light-tight cover and liner. The top schematic drawing of Figure 1.14 shows that the 200 plastic scintillators from CYGNUS are deployed around the pond. These particle detectors can help detecting shower core locations and thus improving the angular and the energy resolution of the entire Milagro detector.

The lower drawing gives details of the internal structure of the detector. Two layers of encapsulated 8" Hamamatsu PMTs (723 total) will be placed inside the volume of water. The top layer, with 450 PMT's, is called the air shower layer and it is used to reconstruct directions of primary particles. The role of PMTs in this layer is similar to that of the particle counters in the CYGNUS experiment, except that they detect Čerenkov light. The bottom layer consists of 273 phototubes and is called the muon layer. To first order, only secondary muons and shower core constituents can penetrate to the bottom of the pond. Despite the fact that (1) many Čerenkov photons generated in the upper water layer may hit the bottom PMTs after attenuation in water, and (2) many energetic shower secondaries, especially those around the shower cores, can travel to the deeper water, Monte Carlo simulations show that secondary muons from air showers can still be well determined by their high intensity light output and their distinct firing pattern among adjacent phototubes.

Once a shower is flagged with one or more muons, it can be rejected as a hadronic background event. The muon layer will have an ability to reject more than 25% of back-

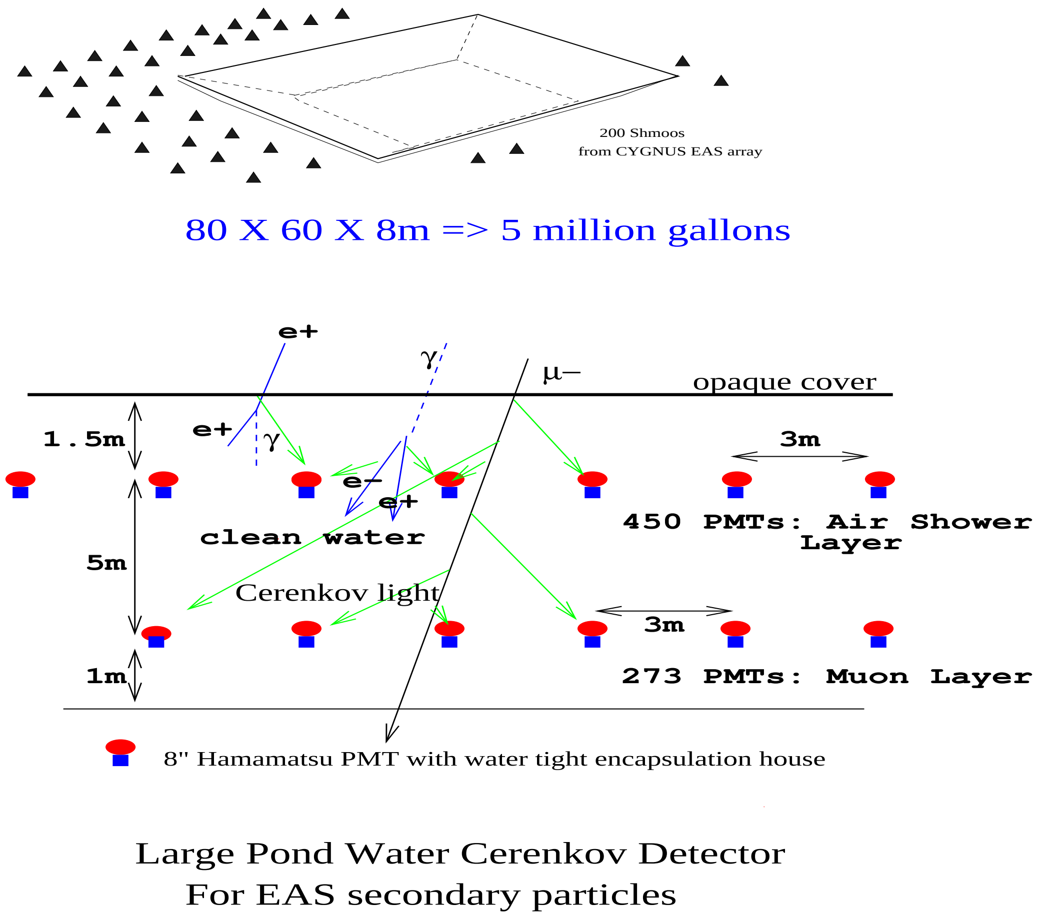

Figure 1.14: A schematic drawing of the Milagro detector.

ground events.[20]

The 3 meter spacing in the upper layer PMTs, which are 1.5 meter deep below the surface, ensures the detection of most EAS secondary particles via the Čerenkov light they emit in water. The Čerenkov light is emitted in an angle of 41° relative to the track of a charged particle in water. Unless a charged particle in water is vertical and located in the middle of the 4 adjacent tubes, or/and it is born too low below the water surface, the large Čerenkov light cone is most likely to hit one or more PMT.

In addition, hard photons from an air shower can interact in water and create electron-positron pairs, which are in turn detected by PMTs. A more detailed discussion on water Čerenkov process will be given in Chapter 3, when the detector simulation is described. Generally speaking, the entire pond acts now like a solid detector. That is an improvement of two orders of magnitude, compared to the poor 0.5% sampling in the CYGNUS case. With a trigger condition of a 40 PMT coincidence in the top layer, Milagro will record air showers at a rate above 1,000 Hz. From the results of Monte Carlo studies, the energy threshold for Milagro is as low as 300 GeV, and the angular resolution at that

[20]Muons spread out widely because they are generated early in the hadronic showers. They might totally miss the detector, especially when shower cores fall outside of the pond.

low energy can still be less than a degree. Like CYGNUS, Milagro will operate 24 hours a day and 7 days a week. It has a large aperture and accepts showers from the sky up to 60° away from vertical.[21]

Owing to the funding schedule, weather conditions at the site,[22] manpower availability, operational-experience demands, and other factors, two intermediate stages were implemented before the full-scaled Milagro is commissioned. The first prototype is called Milagrisimo (11/95 - 7/96),[23] which is a small prototype of Milagro. It took data from April to June in 1996. The rest of this study is about Milagrisimo only. The second stage is called Milagrito (9/96 - 4/98), or small-Milagro. It took data from 2/97 to 4/98. Milagrito consisted of a simple layer of 220 PMTs with 3 meter spacing sitting at the pond bottom covered by 2 meters of water.

[21] As mentioned earlier, the energy required for a horizontal shower to trigger the array is very high, and the primary energy spectrum drops fast. There are practically no triggered events with zenith angle larger than 60 degrees. In addition, since a tilted shower propagates longer than a vertical one, the shower front is thicker than that in a vertical shower. Monte Carlo simulation shows that the angular resolution for large-angle showers is worse than that of vertical ones with the same shower sizes. This aspect will be described again in Section 5.2.

[22] For example, in winter when there is several feet of snow on the top of the pond, we cannot inflate the cover and go into the pond to do servicing.

[23] This made-up word was meant to be "mini-Milagro" by some of us, but Spanish speakers might think the other way around.

Chapter 2

The Milagrisimo Experiment

As mentioned in the last section of Chapter one, Milagrisimo was the first-stage prototype for the Milagro project. It was a small water-Čerenkov detector, with 28 photomultiplier tubes (PMTs) spread out over an area of 600 m^2 at the bottom of the actual Milagro pond. Filled with one meter of water above PMTs, the detector, or the entire water volume, was then enclosed with a light-tight cover.

In this chapter, I shall describe the physical structures, detector configurations and electronic instruments for the Milagrisimo experiment.

2.1 Site Construction

The Milagro reservoir was taken over from a terminated geo-thermal project. In the summer of 1995, the waste in the pond was drained, the pond was cleaned, and a new opaque liner and cover were installed. In the aerial photograph of the Milagro site (Figure 1.13), the black cover can be seen lying on the bottom of the pond, and the white strips are reinforced seams, which are used to help to raise and support the cover.[1]

Several items of the site construction were done in the summer and the immediate following fall of 1995, including the installation of power systems, water lines, phone lines, a clean power generator, an electronics trailer (the counting house), office trailers, a pond utility building (for water filtration systems and cover inflation systems), cover inflation systems, propane heating systems, storage containers, basic lightning protection wires, a T1 data line, the internal PMT support structure (a square grid made of 4 inch diameter PVC pipes), RG-59 PMT cables and water tight connectors. The pond geometry and grid points were also surveyed.

2.2 Milagrisimo PMT, Cable, Configuration, and Water

In fact, Milagrisimo was not planned in the first place. Originally there was only one intermediate prototype proposed, which was Milagrito, and it was scheduled to be installed in the same Fall of 1995. Just prior to the PMT installation, the special adhesive, Stycast, used for PMT encapsulation was found to squeeze and crack the Hamamatsu

[1]Actually, the cover support is largely provided by the filled air within.

PMTs and there was no time to remedy the situation before the onset of snow.[2] The Milagrito installation, therefore, was forced to be canceled in 1995. At that time, there were fortunately 32 10" Burle PMTs available encapsulated in water-tight housings. These tubes had been used earlier in a water-Čerenkov prototype detector with the CYGNUS experiment. The idea of laying a mini array with these 32 tubes was immediately proposed. Three days later, the 32 Burle tubes were installed in the pond (see Figure 2.1). Right after

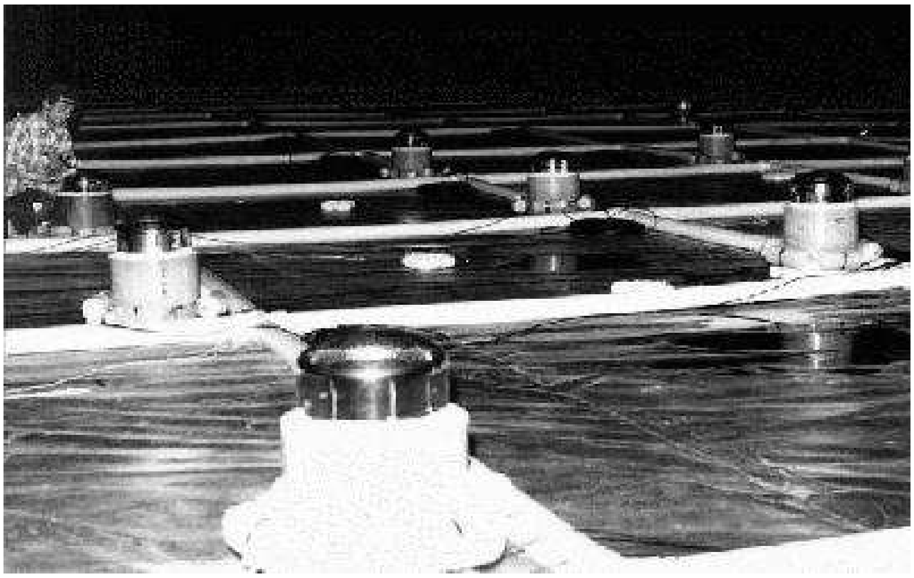

Figure 2.1: The author was installing Milagrisimo PMTs. A total of 32 10" Burle PMTs were placed at the bottom of the Milagro pond. The obvious grid structure was made of 4" diameter PVC pipes with 2.84 m spacing and sitting on the newly installed liner. Some water patches are visible in the photo; they were left from the cleaning job.

the tubes were in place, the process was started to fill the pond with well water. Within a week, all the tubes were immersed and the cover floated entirely on the top of water. Two weeks later, six extra RTV-only (no Stycast) encapsulated 8" Hamamatsu PMTs were added to join the mini array. Thus, there were a total of 38 tubes in the water. We kept filling the pond with water, even during the data taking phase, until there was about 107 cm of water above the surface of PMTs at the edge of array, or 130 cm of water above the surface of PMTs at the center of the array. Ten Burle PMTs with their electronics channels were found to be nonfunctional soon after they were submerged in the water. The problem was mainly caused by leaking around the cable connectors.

The final configuration of the detector, Milagrisimo, consisted of a total of 28 phototubes spread out on an area of 600 m^2 (see Figure 2.3). The water filtration system was not ready at that time to clean the well water, which affected the mean free path for Čerenkov photons. In June, 1996, the attenuation length of the water in the pond was measured to be 2.0 m (at 3,000 Å), 3.1 m (at 3,500 Å) and 3.6 m (at 3,700 Å).[3]

[2] The cover cannot be inflated with heavy snow sitting on it, and, therefore, people cannot go inside.

[3] For comparison, the attenuation length of Čerenkov photons in ice in the AMANDA experiment in the south pole exceeds 30 meters at 3,500 Å.

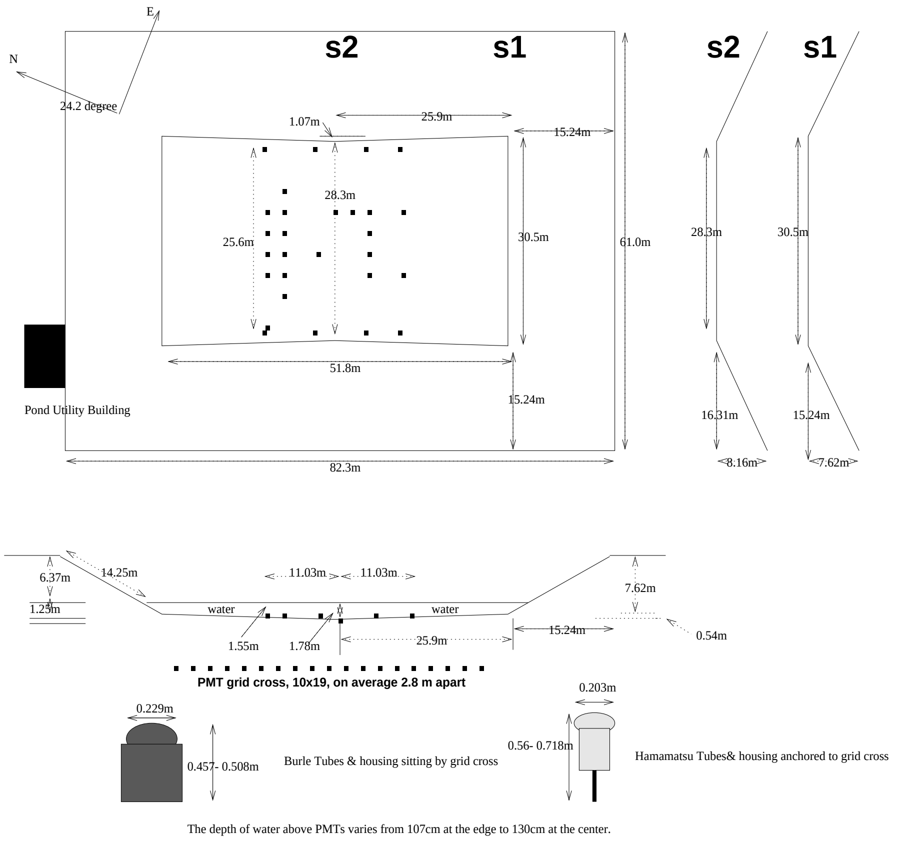

Figure 2.2: The Milagro pond geometry, to scale.

2.3 Power Supply, Clock, and Front-End Electronics

The cables from PMTs came out of the pond and went into the custom-made Front-End Electronics (FEE) boards, which were designed and built by UC Santa Cruz. As shown in the drawing of Figure 2.4, the 12U analog board[4], to which 16 PMT cables were attached and the smaller digital board were connected together to process a total of 16 electronics channels. There were two high-voltage (HV) cables, from two different channels in a CAEN high voltage power supply, connected to a top port and a bottom port on the analog board. Each HV channel supplied 8 PMTs with an identical voltage level.[5] A total of three such analog boards and three digital boards were used in the Milagrisimo experiment. The driving voltage for a PMT and the actual signals from this PMT used the same physical cable. Consequently, there was only one cable going into the pond for each PMT. At the input stage of each electronic channel on the analog board, the capacitor coupling blocked the DC high voltage while transmitting the signals. Throughout the entire electronic channel on the analog board, signals were processed differentially before they were passed to the corresponding channel on the digital board. This differential design suppressed the inter-channel cross-talk by 75 db as well as other noise (Figure 2.5). After the analog

[4] 12 units, which is a measurement of the vertical size in IEEE convention.
[5] The phototubes were grouped by voltage preference.

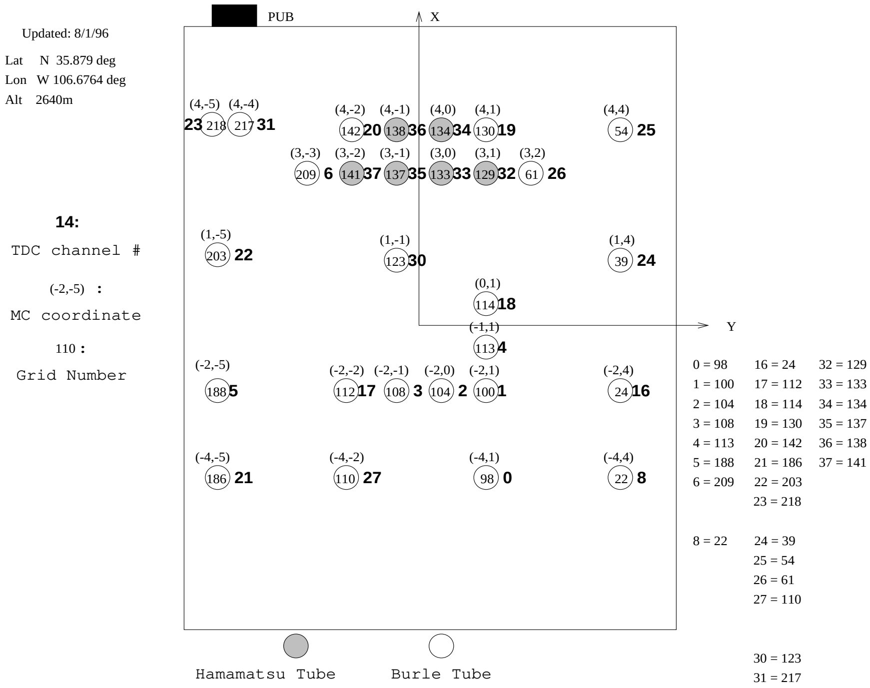

Figure 2.3: A schematic diagram for the Milagrisimo PMT layout.

board processed signals from the PMTs, there were 16 ADC outputs available for the pulse height information. A ribbon cable connected these ADC ports on the analog board to a FASTBUS ADC module — the LeCroy 1881M. Likewise, after the digital board finished processing signals, which were passed from the analog board, the timing information of pulses was available and was sent out, via another ribbon cable, from ports on the digital board to a multiple-hit TDC module — the LeCroy 1877. As will be explained later in Chapter 4 (shower reconstruction), the LeCroy 1881M ADC data were only used for calibration purposes. In fact, even for Milagro (and Milagrito), the ADC data will be used for calibration only. The needed pulse height information can be obtained via the Time-over-Threshold (ToT) method from the TDC data.

The advantages of using the ToT technique instead of the traditional ADC plus TDC are the following: (1) a large amount of money is saved since 1,000 channels of ADCs are not needed,[6] (2) with the absence of ADC data, the event size is cut significantly, and in turn, the ability to handle a higher trigger rate in the data acquisition is enhanced, (3) the ADC conversion time is relatively slow, $\sim$12 microseconds, and that may cause dead time during data taking, (4) there is no need to worry about synchronizing the ADC and TDC data,[7] and (5) the ToT has much better dynamic range than that in the ADC.

A PMT pulse delivers a charge which charges the capacitor, and the capacitor then discharges as that in a simple RC circuit (with resistance R and capacitance C). At time t_a, the capacitor starts to discharge into the resistor and at a later time t_b the voltage

[6] The 1,000 channels includes the particle scintillators around the pond.

[7] For some unknown reasons, sometimes ADC and TDC data do not match up with each other event by event. In Milagrito and Milagro, since there is more than one LeCroy 1877 module, the out-of-sync problem may still exist even without the ADC data.

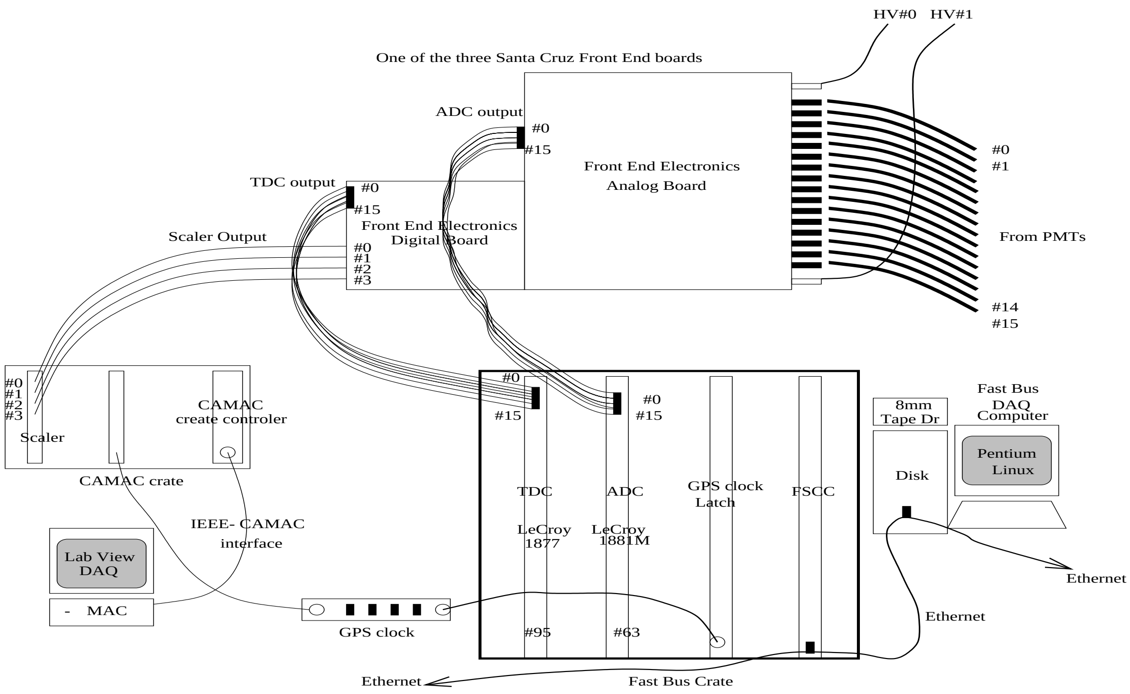

Figure 2.4: A drawing for the Milagrisimo electronics and data acquisition system.

drops to,

$$V_b = V_a \, e^{-(\frac{t_b - t_a}{RC})}.$$

The charge in the capacitor is proportional to the voltage across, Q=VC. Therefore, the original charge stored in the capacitor, Q_a, can be presented in terms of parameters at a later time t_b:

$$Q_a = C \, V_b \, e^{\frac{t_b - t_a}{RC}},$$

or $Q_a \propto e^{(t_b - t_a)/T_c}$, where $T_c = RC$ is a characteristic time constant for the circuit. Figure 2.6 shows two PMT signals as seen on an oscilloscope. The y-axis displays voltage and x-axis, time. The voltage drops, for example, for the top pulse in the figure, from time t_a (point a) to time t_b (point b). The "pulse height" of a signal from PMT is proportional to the stored charge caused by photoelectrons. Thus,

$$PMT \ pulse \ height \quad \propto \quad charge \ deposited \quad \propto \quad e^{(t_b - t_a)/T_c} \ , \tag{2.1}$$

where T_c now is the characteristic time constant for the entire electronic channel. Each channel has its own characteristic T_c. As shown in the figure, the crossing times t_b and t_a are recorded by the digital board as a "2-edge" event.

In order to cover a larger range of pulse height with better statistics, to avoid the nuisance of a prepulsing problem,[8] and to minimize the problem of pulse size misinterpretation when small random noise rides on the tail of the main signal just before the threshold

[8] Large pulses sometimes have accompanying small pulses, which arrive earlier than the main pulses. This prepulsing problem will be explained in Chapter 4.

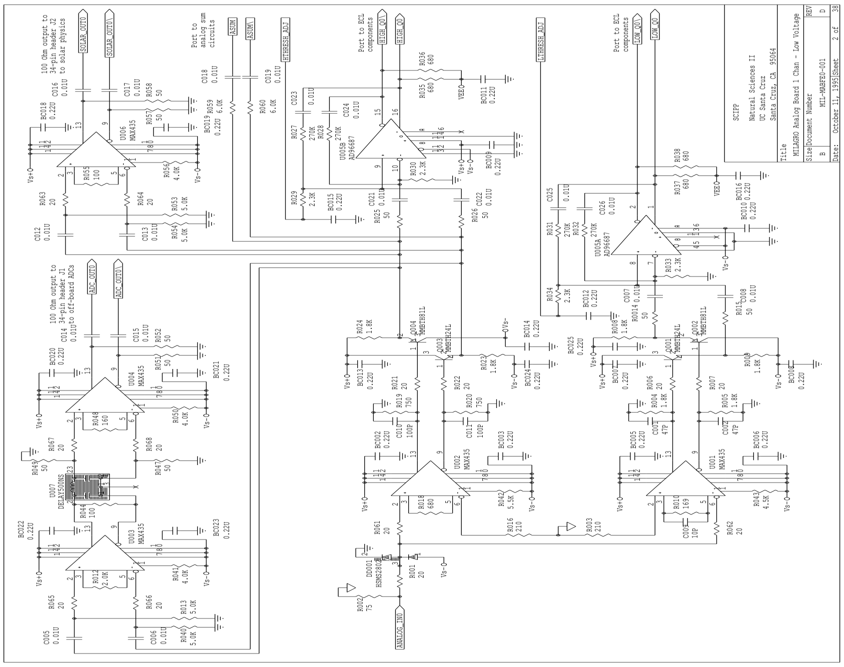

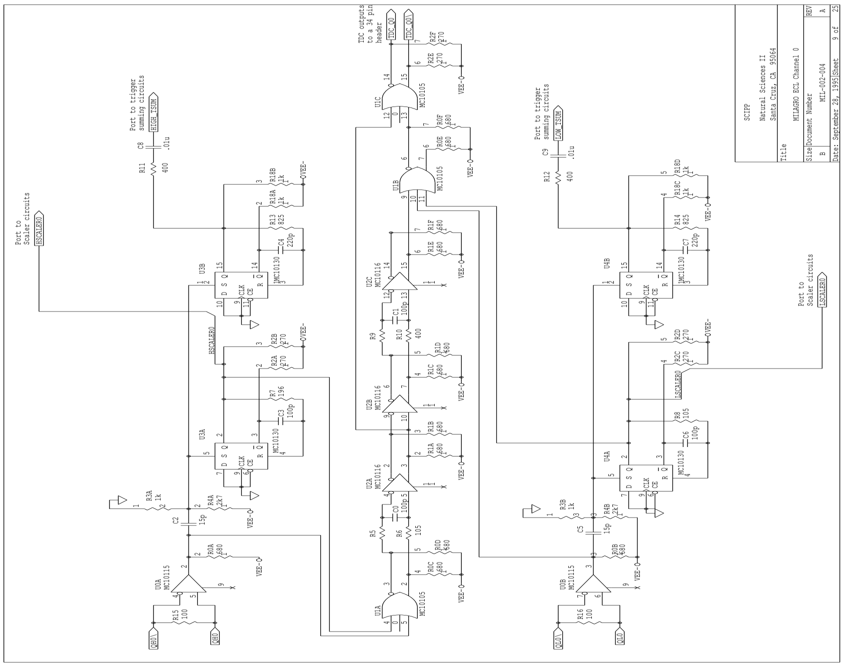

Figure 2.5: The circuit diagram for the front-end electronics boards. The top one is the analog board and the bottom one is the digital board.

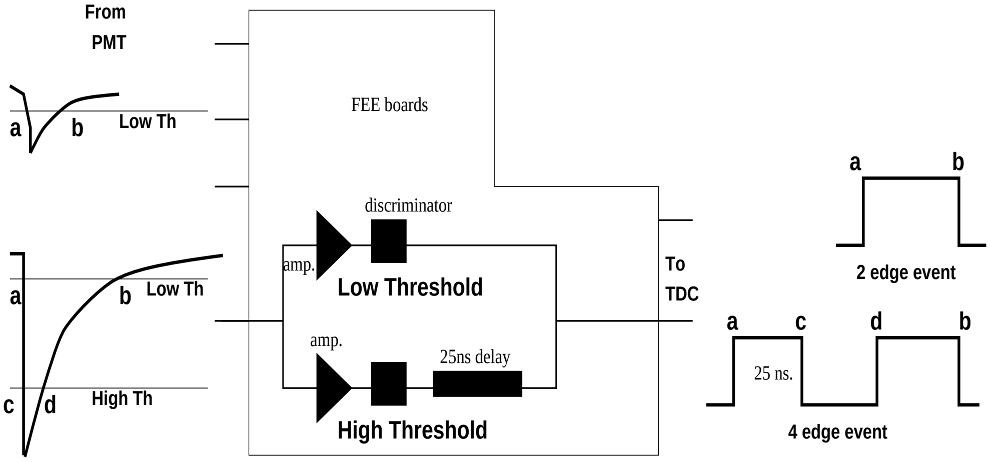

Figure 2.6: A conceptual drawing of the time over threshold method.

crossing, a second voltage threshold is introduced.[9] As shown in the bottom pulse in Figure 2.6, there are two preset thresholds, a low ToT threshold and a high ToT threshold. The low threshold is set at about 0.25 photo electron (PE) and the high threshold is at about 6 PEs. The pulse height unit of PE is actually defined by the ADC data and will be shown in Chapter 4 (Figure 4.9). A small pulse from the PMT can pass only the low threshold, and thus it only produces two crossing edge times, while a large signal can fire both the low threshold and the high threshold to generate 4 edge counts in the TDC. Each one of the 96 channels on the LeCroy TDC 1877 module can store up to 16 timing edges, with a time resolution of a half nanosecond. Given an external input of a common-stop signal to the LeCroy 1877, an earlier timing edge records a larger number in TDC counts.

Because there were not many active channels in the Milagrisimo experiment, and an *in situ* test of the ToT method was needed for the planned Milagro data acquisition, one 64-channel LeCroy 1881M ADC was in fact connected to take the pulse-height output from the analog FEE board. A GPS clock with an accuracy of one microsecond was connected to a latch module in the FASTBUS crate to join the data stream with the TDC and ADC information.

2.4 Trigger

When the experiment was running, each electronics channel which had its low threshold crossed by a PMT pulse contributed an additive –50 mV to a total sum of the 16 channels on the digital board. This total sum was then available for use via a port (*trigger sum*) on the front face of the digital board. For example, the output would measure –0.55 volt if there were a total of 11 PMTs fired out of all the 16 channels on that board. In the setup of Milagrisimo, voltages of trigger-sum outputs from all 3 digital boards were further added together before a final lemo cable took the voltage sum into a discriminator

[9]The same small random noise can ride on the tail of signal before the "high threshold" crossing as well, but the error introduced is smaller than that in the "low threshold" crossing case because the signal shape is much steeper around the high threshold region.

module with a preset threshold of –0.571 volt. This –0.571 volt threshold translated into a trigger requirement for Milagrisimo of 12 or more fired PMTs. The discriminator output was properly delayed and used as the common-stop signal to the 1877 module.

We choose an coincidence window of 250 nanoseconds (ns), after considering all the following timing factors involved: (1) the rate of a single PMT is $\sim$ 10 kHz, or one hit per 100 μs, (2) the trigger rate of the experiment is $\sim$ 100 Hz or one trigger per 10 ms for a 12-fold multiplicity, and (3) it takes an extra $\sim$ 100 ns longer for a horizontal shower to finish passing through the detector than it does for a vertical shower.[10] On average, the summed-voltage signal sits in the middle of the coincidence window. All fired PMTs in a triggered event thus record particles from the same air shower; the possibility of getting a contaminated event is small.[11]

2.5 Data Acquisition

The FASTBUS Smart Crate Controller (FSCC) we used in Milagrisimo was designed by Fermilab and made by Bi-Ra Systems. It is a single-board computer with a 16MHz Motorola 68020 CPU, 4Mb of memory, two RS232 serial ports for console and control, a 10BaseT ethernet connector, and an embedded bootable operating system – the kernel of VxWorks[12] on PROM chips. Of course, the FSCC's bus type (protocol) is FASTBUS. The FSCC is the bus master and controls all other FASTBUS modules present in the same crate, such as the LeCroy 1881M ADC, the LeCroy 1877 TDC, and the clock latch module. After power-on for the crate (and FSCC), the embedded VxWorks OS kernel in the PROM chips boots up the FSCC so that a VxWorks shell prompt is seen on a console screen. By the time it finishes loading the kernel, the OS has already detected the FASTBUS modules present, the I/O ports and the ethernet port, just like a regular computer. The user can then enter commands from the keyboard of the console to configure the hardware ethernet port on the FSCC (e.g. assign IP address, gateway and host computer's IP address) so that the FSCC can further download the remaining part of the operating system, more drivers, libraries for FASTBUS modules and data acquisition software over the network from another computer.

Once the data are available on the bus during the running of the experiment, we have to ship them out before they accumulate.

For Milagro and Milagrito, the planned method to send out the data in FASTBUS is complicated and has many intermediate modules involved. The full scheme is: the FSCC sends out the data via a ribbon cable to an intermediate board (named DC-2) outside the FASTBUS crate, afterwards, the data will be transferred from the DC-2 board to the VME bus in a separate VME crate, and finally, the main DAQ computer, an SGI Challenge, can access the data through the dual-ported memory modules in the VME crate. At the time of the Milagrisimo experiment, this complicated FSCC/DC-2/VME/SGI acquisition system was far from ready. To enable us to run the experiment, a shortcut was developed.

The FSCC is a computer without an internal disk interface such as SCSI or IDE.

[10] The coincidence window only makes sure to cover all "arriving" times of hits in the same shower, not their "durations". A typical time constant for an electronics channel is $T_c \sim 100$ ns, which means the duration of the threshold crossing for a large pulse can last up to $\sim$ 600 ns (refer to $T_b - T_a$ in Figure 2.6).

[11] Later in Chapter 4, Figures 4.7 (a) and (e) show the distribution of hit times for two chosen PMTs in real triggered events. The majority ($> 99\%$) of PMT hits accumulate within a 500 ns range.

[12] VxWorks is a UNIX-like real-time operating system, which is widely used in data control and acquisition.

Fortunately, it has ethernet networking hardware plus complete TCP/IP networking support in VxWorks. With TCP/IP support, the natural approach would be to mount a disk from another computer over the network to the FSCC so that the FSCC could just dump data on the NFS (Network File System) disk. However, the expensive burn-in PROM chips we had for Milagrisimo on the FSCC did not include, among other things, the NFS networking support in the kernel. Even though we could always download NFS software from the host computer, we could not insert the NFS drivers into the kernel while it was running.[13] Consequently, the NFS did not work. As a last resort, a network driver using the lower networking building block, socket protocol, was written, which is common to all UNIX platforms. A path was successfully developed to deliver data through sockets riding on the ethernet hardware. Data traveled directly from the FSCC to a host computer — a Pentium 100 PC running Linux 1.1.12. The 10BaseT ethernet had a hardware bandwidth limit of 10 Mps or 1.25 megabytes per second. Nevertheless, it was fast enough to handle the data rate for the Milagrisimo experiment. Once the data were read in by the Linux system and written to its disk, they were backed up to 8mm tapes.

Milagrisimo took data at a peak rate of 125Hz, when the water level reached its final depth of one meter above tubes at the rim with a trigger requirement of 12 or more PMTs fired. The dead time for Milagrisimo in the FASTBUS was practically zero and was measured to be less than 0.5%. With a regular event size of about 350 bytes, the throughput data rate was 0.05 Mbyte/s, which was far below the 10BaseT ethernet bandwidth limit. The data output for a triggered event with N fired PMTs consisted of N channels of zero-suppressed TDC edge counts (a 2 edge hit or a 4 edge hit), N channels of ADC counts, and 8 bytes of GPS data for the time of trigger. In Chapter 4, I shall explain how these raw data were processed for shower reconstruction.

[13]Recently, most UNIX operating systems have been developed such that drivers can be plugged in on the fly.

Chapter 3

Milagrisimo Simulation

If there were one or more intense TeV gamma-ray sources (with known positions and spectra) around to calibrate the Milagrisimo detector, a simulation would not be necessary. Unfortunately, such sources were not available to Milagrisimo.[1]

The simulation for Milagrisimo is a computational process to imitate all the interactions in the air shower development, the water Čerenkov light generation and the detector response. In order to do this, we have to enter all relevant known properties of air, water and other material involved, as well as the probabilities for all possible interaction channels based on their cross section data. Where cross section information is not available from the accelerator data (for example, the cross section for a 100 TeV γ to create an electron-positron pairs in air), theory is used to extrapolate from lower energy data. Since there are millions[2] of interactions involved in a typical air shower generation, only a handful of air-shower parameters, as I shall discuss soon, can be extracted by simply applying analytical and statistical methods to predict what a final "average" shower should look like.[3]

When the simulation follows a secondary particle in an air shower, it reads in a table of probabilities for all possible channels for this particle before it travels further. The simulation then takes a random number between zero and one, compares the outcome fractional number to the table of probability and decides which channel this particle should follow and how far the step is. This nature is similar to the dice-throwing in a casino, so the simulation is also called Monte Carlo simulation.

As discussed in the CYGNUS section in Chapter 1, after an air shower is detected, what we really want is the information about the primary particle — its direction, identity, and energy. We have to reconstruct these properties from the experimental data. In contrast, a simulation starts from a primary particle with known attributes (identity, energy and direction), and in the end it gives the final detector output, whether it is a triggered event or not. By comparing the simulated output with the actual data, we can deduce much valuable information about the primary particles, which cannot be obtained from the experimental data alone. Also, by adjusting air and detector parameters (altitude, water

[1] Since the angular resolution for Milagrisimo was not good enough and the experiment did not last long enough, the data were not sensitive enough to see the Crab pulsar or AGNs. In addition, as explained in Appendix A, the trigger energy was too low for the detector to examine the deficit of the moon shadow.

[2] Including numerous steps of multiple Coulomb scattering.

[3] Most of these parameters derived from analytical methods, for example, the number of secondary electrons and the lateral distribution, still cannot be directly measured by the detector.

depth, water attenuation length, PMT size and arrangement, etc.), we learn how the final data depend on these changes. Without the use of a simulation in the early stages, it is impossible to optimize the design of a complicated detector, such as Milagro. In addition, without simulation, it is very difficult to analyze or even understand the data, both during and after the experiment, since the experimental data never speak for themselves. In the case of Milagrisimo, specifically, only via the help of simulations, can we get information about the trigger energy and angular resolution.

Milagrisimo Monte Carlo simulations can be separated to two parts: the air shower and the pond detector. Both γ-ray primary particles and cosmic background primary particles (proton showers) are simulated. The air shower part covers the processes from the top of the atmosphere to the pond cover. Once the surviving secondaries reach the pond, the detector simulation takes over, transporting them inside water, and generating Čerenkov light whenever applicable. Because each process is complex, and there are only few directly observable quantities in the experimental data, I use several independent Monte Carlo packages and customize them to fulfill the Milagrisimo simulations. GEANT, EGS4, and SHOWERSIM packages are applied and their results are compared in great detail. If good agreement exists among the different Monte Carlo simulations, we can proceed with confidence.

3.1 Atmospheric Model

In Section 1.5, which describes the CYGNUS experiment, we briefly discussed the processes of extensive air showers and mentioned the unit of radiation length several times. To simulate an air shower, we have to first set up a model for the atmosphere. The atmosphere above the Milagro pond has 750 g/cm^2 of air overburden, or in high-energy physics terms, it is 20.75 radiation lengths. The air density decreases going to higher altitude. The air above Milagro is divided into 42 slices (Figure 3.1) of constant density, which use the actual atmosphere profile of measured density and pressure (as a function of the height above sea level). Each one of the 42 slices is 0.5 radiation length thick except for the first slice (the top slice), which is only 0.25 radiation length. The upper slices are thicker than the lower ones. For example, the second air slab from the top has a thickness of 7 km, whereas the thickness of the third one decreases to 4 km, although both of them are 0.5 radiation length of air. This atmospheric model is implemented into both GEANT and EGS4, which will be described in the following sections. In the case of the SHOWERSIM package, however, there is no need for such user-supplied air model, because it has a built-in exponential atmosphere.

3.2 Simulation Packages

3.2.1 GEANT

GEANT (GEANT, 1994), developed and maintained by CERN for many years, is a general and comprehensive software system for simulating a wide variety of interactions occurring in high-energy physics as well as complicated apparatus responses. It is written mainly in Fortran code. The copy used for Milagrisimo simulation is Version 3.21. GEANT

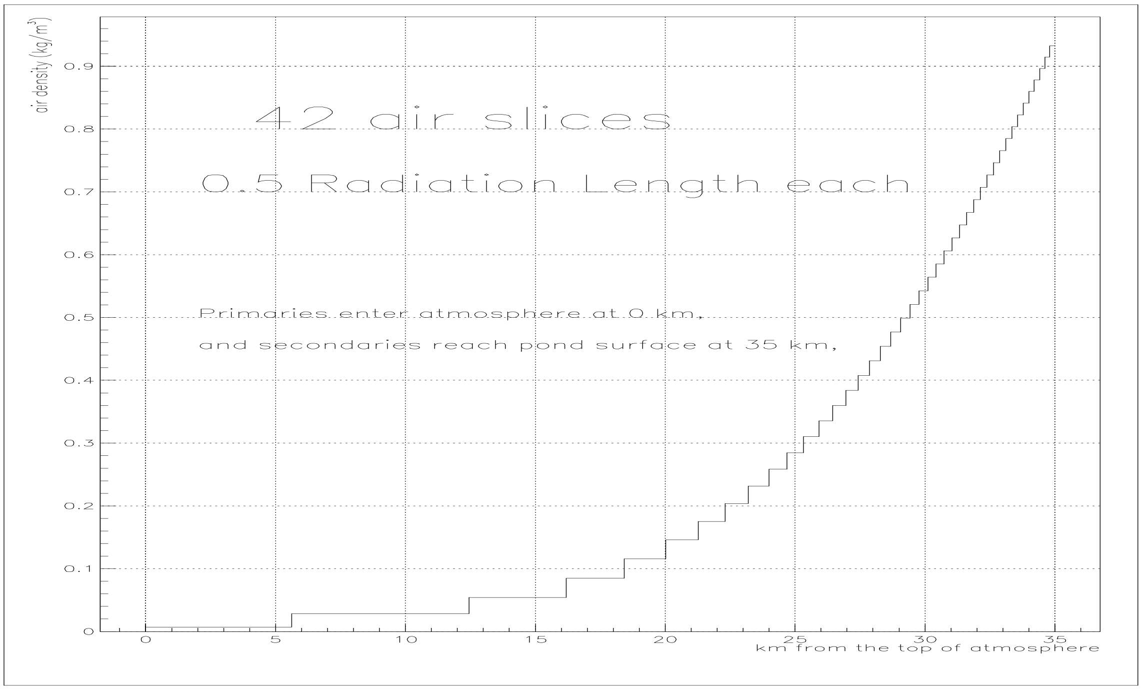

Figure 3.1: The atmospheric model for the air shower simulation.

is able to thoroughly simulate both γ and proton induced EASs for Milagrisimo, once the air model is provided.

3.2.2 EGS4

EGS (Nelson, 1985), developed by SLAC, is another popular Monte Carlo system in the high-energy physics community for simulating electromagnetic interactions within matter, even though it does not handle hadronic transport. The most current version, EGS4, is used in the Milagrisimo simulation.

3.2.3 SHOWERSIM

Originally written by Wrotniak, SHOWERSIM (Wrotniak, 1984), unlike GEANT or EGS, was specifically designed for the purpose of UHE (refer to page 6) air-shower simulations. It runs fast since it omits much less important detail. SHOWERSIM was tuned by known air-shower data above 100 TeV. For electromagnetic secondaries, SHOWERSIM only carries them down to a certain energy level (for example, 20 GeV), and whenever an electromagnetic secondary drops below that energy level, the program user has to take care of the soft secondary particle by himself to finish the entire shower. In this study, when secondary electrons or photons drop below 20 GeV, EGS4 is called to continue and follow these energetic soft residues, or “tails,” all the way down to 1 MeV. On the other hand, for the hadronic transport, all secondaries are processed by SHOWERSIM itself, and are followed to as low as 10 MeV in kinetic energy, before they are discarded.

These days, CPU power is no longer the number one concern in VHE or UHE air-shower simulations. A low-end workstation can generate a full-blown air shower above 1 TeV in a short time using either GEANT or EGS. Ideally, I should run through all three Monte Carlo programs and present their results in such a way that they can be compared directly with Milagrisimo experimental data. We shall do that[4] at the end of the Chapter 4, when experimental data are available. At the mean time, since there are many adjustable parameters (some of them are very important and they are well defined in theory) involved in a complete EAS simulation, different Monte Carlos and theories can be compared even in certain intermediate stages. It is more sensitive and informative to check results in several different stages than to do a final yes-or-no type comparison of the data.

3.3 Longitudinal Development

In this section and the next, two intermediate shower properties obtained from a selected Monte Carlo package are compared to their relevant theories.

As explained briefly in Section 1.5, when an EAS propagates through the atmosphere, the number of secondary particles (electrons or photons) increases as they repeatedly split. The energy of the primary particle, therefore, is distributed among all its secondaries. As the EAS develops further, the absorbing power of air is no longer negligible and starts to play a role in stopping some lower energy secondaries. When the stopping rate becomes higher than the multiplying rate, the total number of EAS secondary particles begins to decrease until the entire EAS dies out or reaches the ground. Theorists have examined the nature of processes in the EAS transport and have come up with an analytical formula for the EAS longitudinal (from top to bottom) development. The best one, known as the "approximation B" formula (Gaisser, 1990), calculates the number of secondary electrons, N_e, during the development of an electromagnetic air shower (with primary energy $E_\circ$) versus the shower depth, t (in units of radiation lengths). It is given by,

$$N_e = \frac{0.31}{\sqrt{y}} e^{t(1-1.5\ln s)}, \tag{3.1}$$

where

$$s = \frac{3}{1+\frac{2y}{t}}, \tag{3.2}$$

$$y = \ln(\frac{E_\circ}{E_c}), \tag{3.3}$$

and $E_c = 90$ MeV (Aguilar-Benitez, 1998), the critical energy for air.[5] The s number marks how "old" a shower is during its development and therefore is called the age parameter. In the upper plot of Figure 3.2, the solid lines represent the theoretical approximation B formula, for various energies, $E_\circ$, from γ primaries. The curves, defined by diamonds, hollow circles, and asterisks, are average simulation results from γ primaries using GEANT. These Monte Carlo results are averaged from fixed-energy vertical GEANT EASs of fifty 2 TeV γ, five hundred 500 GeV γ, and one thousand 100 GeV γ showers, respectively. The straight vertical line shows the air depth of the Milagro site.

[4] Only GEANT and EGS are used for the real detector simulations.

[5] The critical energy is defined as the energy below which the dominant energy loss is by ionization rather than by bremsstrahlung.

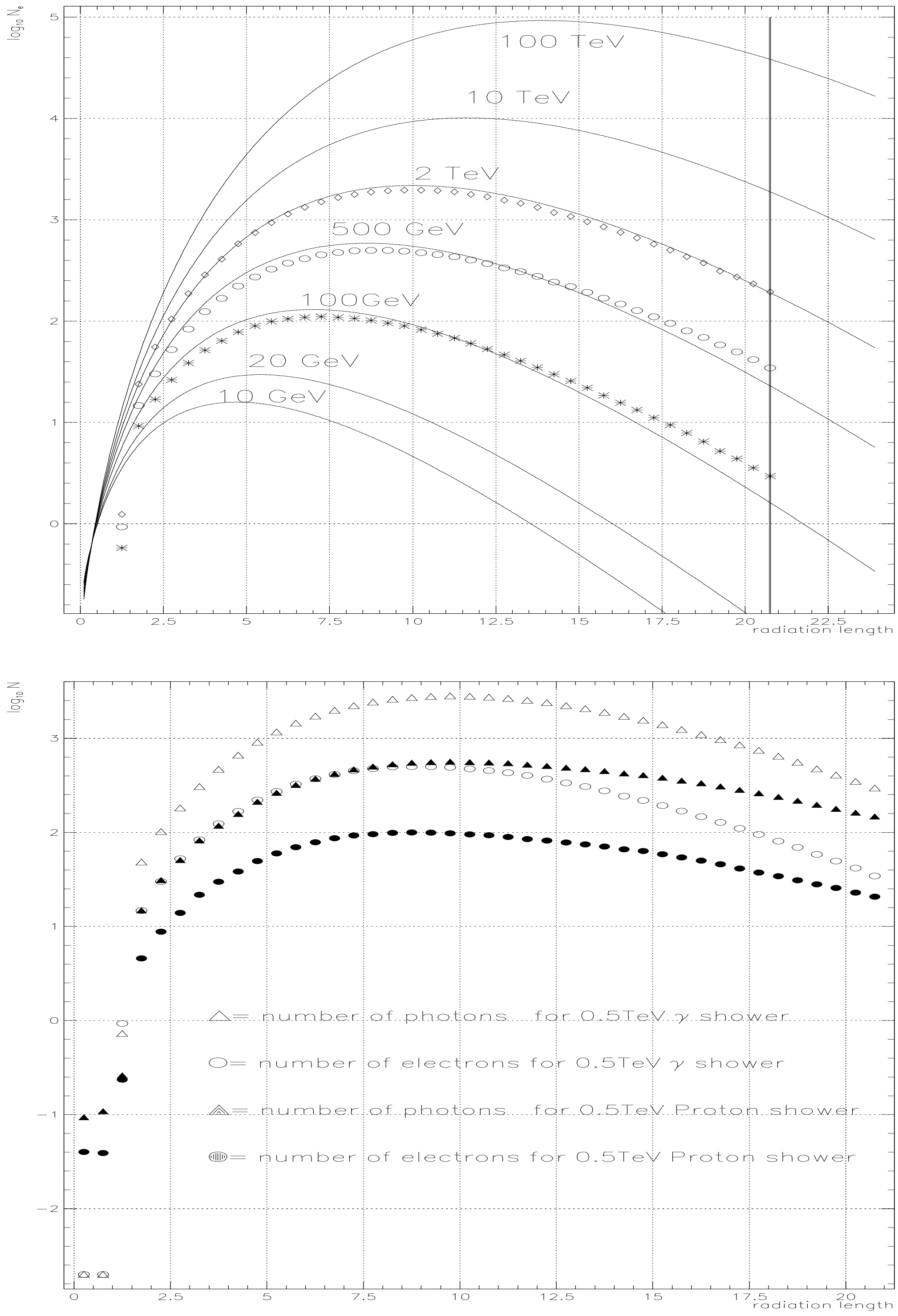

Figure 3.2: The longitudinal development of EAS. Solid lines plot the approximation B formula. Symbol curves represent the average EASs, which are obtained from many air showers with identical primary energies to smooth out the shower-by-shower fluctuations.

The upper plot only shows the number of secondary electrons. The 500 GeV hollow circle curve is plotted again in the lower chart of Figure 3.2. In addition, the number of secondary photons for the same 500 GeV γ "average" shower is shown by hollow triangle symbols. Clearly, the number of secondary photons is many times more than that of secondary electrons at all depths. This result has drawn people's attention to the consideration that a better detector must be able to detect these valuable secondary photons as well as secondary electrons. For comparison, also plotted in the lower half of Figure 3.2 are the average number of secondary electrons and the average number of secondary photons in a 500 GeV proton EAS, which are obtained from 2,000 GEANT fixed-energy (500 GeV) vertical proton showers. There are more secondaries in a γ shower than those in a proton shower with the same primary energy mainly because a large portion of the proton energy goes into muons, hadrons and neutrinos. In fact, less than half of the primary energy in a hadronic shower is carried by electromagnetic secondaries. We say that the γ shower has larger shower size than that of the proton shower with the same primary energy.

Overall, γ Monte Carlo showers agree well with approximation B.

3.4 Lateral Development

The lateral spread of secondary electrons that reach the ground from a γ primary has also been worked out analytically and yields the so called Nishimura, Kamata and Greisen (NKG) distribution (Gaisser, 1990). In the case of Milagrisimo, for which the atmospheric depth is $t = 20.75$, the lateral electron density is given by,

$$\rho(r) = \frac{N_e}{(r_0)^2} f(s, \frac{r}{r_0}), \tag{3.4}$$

where r (in meters) is the lateral distance from the sampled spot to the shower axis,

$$f(s, \frac{r}{r_0}) = (\frac{r}{r_0})^{s-2}(1+\frac{r}{r_0})^{s-4.5}\frac{\Gamma(4.5-s)}{2\pi\Gamma(s)\Gamma(4.5-2s)}, \tag{3.5}$$

r_0 is equal to 99 meters, the Molière multiple scattering unit at Milagrisimo's altitude, Γ is the Gamma function, and s is the age parameter, as defined in Equation 3.2. In Figure 3.3, the NKG formula for a 0.5 TeV γ primary is plotted as the smooth solid line, and is directly compared to Monte-Carlo results. The solid histogram is generated from averaging over 8,000 0.5 TeV GEANT proton showers, and the dashed histogram is generated from averaging over 500 (thus, with poorer statistics) 0.5 TeV GEANT γ showers.

The simulations generally agree well with theories. A more careful comparison shows that γ showers are steeper than proton showers in the lateral distribution and the NKG curve agrees better with the proton EAS simulation than with the γ EAS simulation. The same result, that γ showers are steeper than proton showers, was independently discovered by other people (Hillas & Lapikens, 1977). In the γ-ray astrophysics community, this difference is commonly known as that a γ shower has a better defined "shower core" than that of a proton shower. While the main contribution for shower spread comes from the electron multiple scattering in the air for both γ and hadronic showers, one big reason to cause the difference between the two cases is the existence of the transverse momentum in hadronic interactions, which is approximately $\langle P_\perp \rangle = 400\ MeV/c$ (Sokolsky, 1989). This transverse momentum makes a hadronic shower more spread out and chunky.

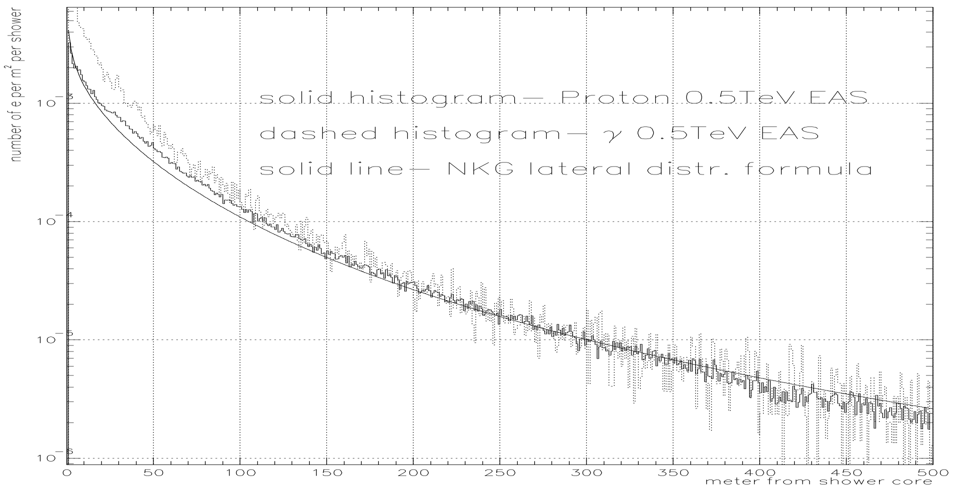

Figure 3.3: The EAS lateral distribution. The solid line represents the NKG formula; the solid histogram plots an average 0.5 TeV GEANT proton shower; and the dashed histogram, an average 0.5 TeV GEANT γ shower.

3.5 EAS Comparisons Between Different Monte Carlos

In this section, the attributes of secondary particles at the ground level obtained from the three Monte Carlo packages will be compared.

3.5.1 γ Primary

GEANT and EGS4 are compared directly for γ primaries of one energy. In both cases, 500 fixed-energy 0.5 TeV vertical γ EASs are generated. After these 500 showers are finished in each case, the number of total secondaries is divided by 500 to produce an average shower. All histograms in Figure 3.4 are prepared this way. The low energy cut for shower secondaries is 1 MeV inside both GEANT and EGS4. In other words, all secondary particles (only electrons and photons in the γ category) are followed to 1 MeV before they are discarded. In all eight plots, GEANT results are plotted in solid histograms and EGS4 ones are plotted in dashed histograms. All four charts at the left-hand side in Figure 3.4 are for secondary photons, whereas the four to the right are for secondary electrons. The first two plots on the top row are energy distributions among secondaries in MeV. The two plots in the second row are lateral distributions of secondaries, covering a range from their shower cores to 500 meters. The two in the third row are timing distributions of secondary particles up to 250 ns. The definition of "time" of a secondary particle in an EAS is the time delay relative to the arrival time of the shower core. Take a vertical shower as an example, the shower core hits the ground first and defines the time zero for all its secondary

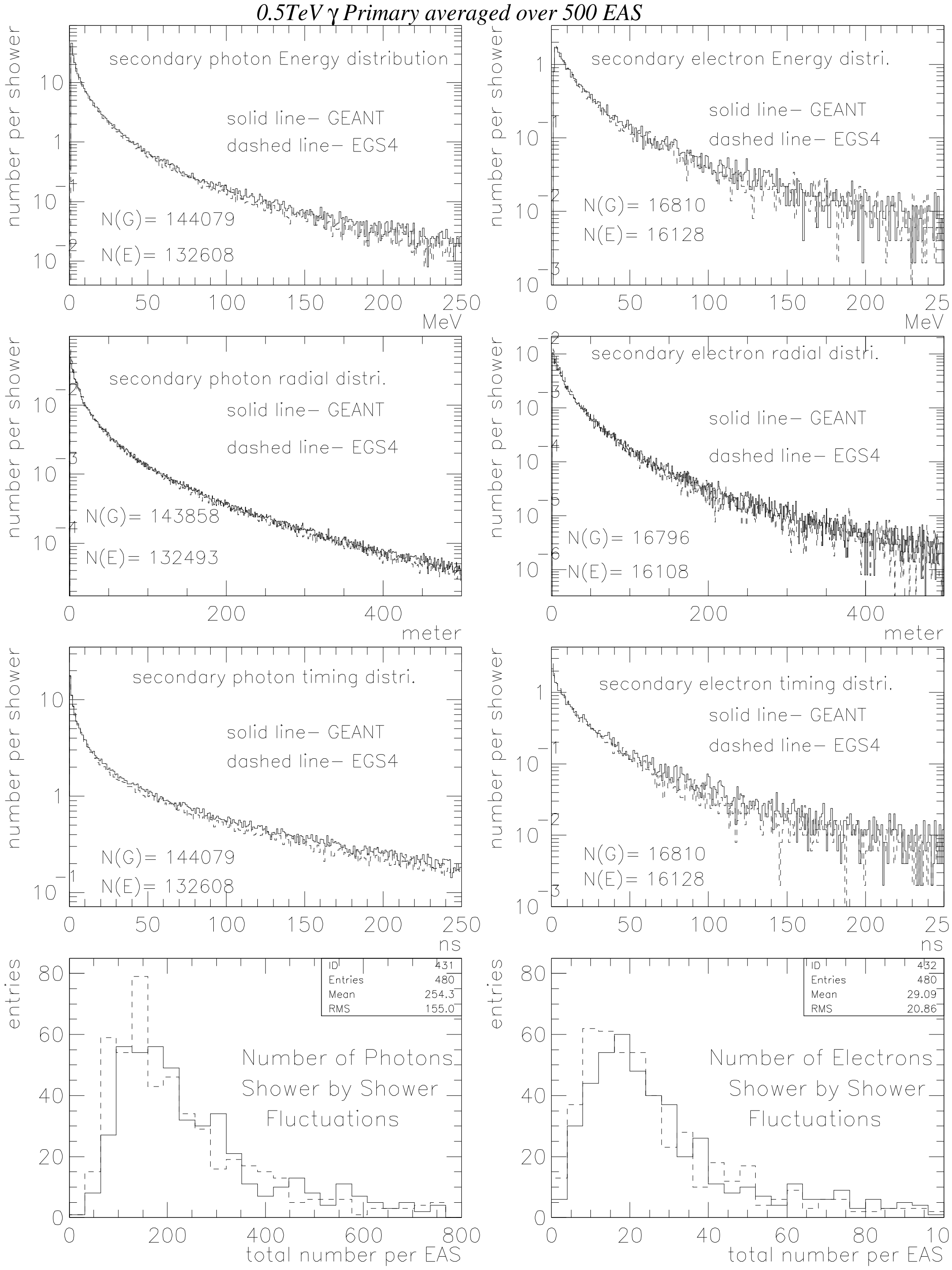

Figure 3.4: The comparison of γ -induced EAS between GEANT and EGS4. The figures are described in the text.

particles. In the same shower, if a secondary electron, which is located 100 meters away from the shower axis, hits the ground 25 ns later than the shower core, it has a "time" of 25 ns. In a more general case of a tilted shower, one side of the peripheral secondary particles will arrive earlier than the shower core; therefore, they have negative times. The final two plots at the bottom row show the number of secondaries for each of the 500 individual showers to reveal the effect of shower-by-shower fluctuations. Even with the same energy, one shower may contain 800 surviving electrons, whereas another shower may only have 30. This fluctuation reminds us that a ground-based experiment, such as Milagrisimo, actually triggers on shower fluctuations rather than on the "average" shower. This is another reason a full-scaled simulation is more useful than an analytical prediction.

The results of γ showers show good agreement between GEANT 3.21 and EGS4.

3.5.2 Proton Primary

For hadronic showers, the result from GEANT is to be compared with that from the combination of {SHOWERSIM + EGS4 tail} since EGS4 itself does not handle hadronic interactions. As shown in Figure 3.2, the shower size (number of electromagnetic secondaries) of a proton shower is smaller than that of a γ shower with the same primary energy. More showers are needed for the proton case to achieve the same statistics. 2,000 fixed energy 0.5 TeV vertical proton EASs are generated with both GEANT and {SHOWERSIM + EGS4}. In each case all secondaries from the 2,000 showers are collected together in one single data file; by the same token, the number of total secondary particles is divided by 2,000 in the end to produce an "average" 0.5 TeV proton shower. All histograms in Figure 3.5 are defined and arranged similarly to those in the previous γ case, except for the bottom two rows, which are only for the proton case. As seen on the plots, GEANT and {SHOWERSIM + EGS4 tail} agree with each other very well in their energy spectra of electromagnetic secondaries, lateral distributions of electromagnetic secondaries, and timing distributions of electromagnetic secondaries. The two new plots in the fourth row in Figure 3.5 show the energy and lateral distributions respectively for secondary muons. The final two plots at the bottom row show the energy and lateral distributions respectively for secondary hadrons (kaons, pions, neutrons, and so on). Disagreement appears. The results from SHOWERSIM (the bottom four plots have nothing to do with EGS4) contain more muons and fewer hadrons than those from GEANT. Given all the other good agreement between their results, the chance that the difference is caused by programming errors during implementation of either GEANT or {SHOWERSIM + EGS4 tail} is small. The SHOWERSIM package may have over-simplified the hadronic processes in order to transport air showers quickly. GEANT is widely believed to have better treatment of hadrons since it has been verified by accelerator data at these energy levels (< 0.5 TeV).

To conclude this section, we have verified and selected GEANT 3.21 as a valid tool for Milagrisimo air-shower simulations.

3.6 Milagrisimo Air Showers

After individual air showers are discussed, it is necessary to simulate the global situation that the detector actually sees. We are interested in questions like: How many

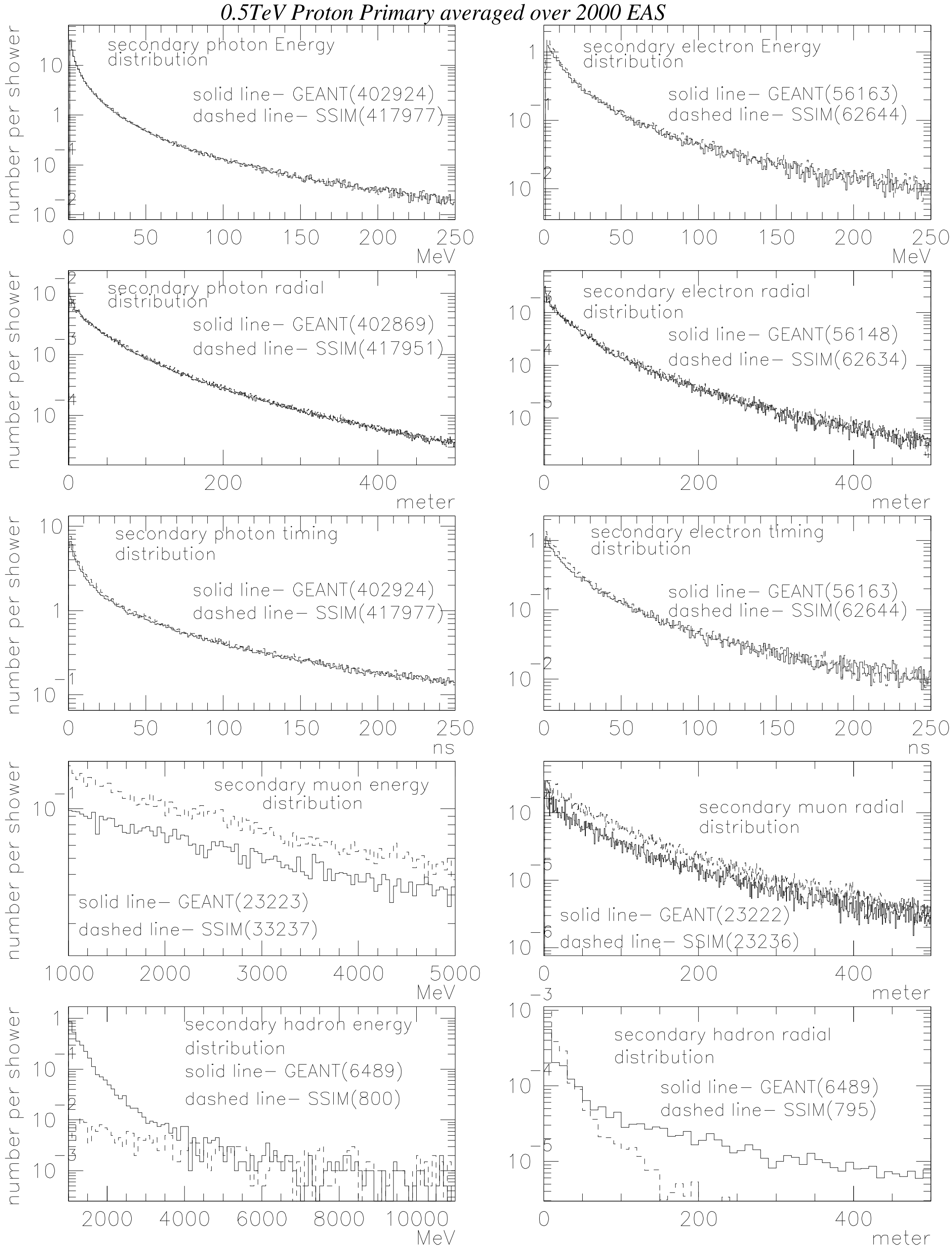

Figure 3.5: The comparison of proton-induced EAS between GEANT and {SHOWERSIM + EGS4}. The figures are described in the text.

showers per second does the detector trigger? Should all showers come from the vertical direction? Do all the showers have the same energy? and Where do shower cores land?

As seen by an observer at the top of atmosphere, the number of cosmic-ray counts per fixed time interval is the same from any direction in the sky (with the same space angle opening, that is). In other words, cosmic-rays are isotropic and the density is constant regardless what direction (θ, ϕ) one chooses.[6]

If this space-based observer can as well measure the energies of cosmic rays, he will conclude that the energy distribution follows a well-defined spectrum. Over more than half a century, the cosmic-ray energy spectrum has been independently measured by many different experiments. Different experiments, however, have their own characteristic energy ranges. It is thus more appropriate to quote the spectrum formula from an experiment with a similar energy range to that of the Milagrisimo detector than from experiments with very different ones. In this study, the spectrum measured by the collaboration of the Tibet Air-Shower Array (Amenomori, 1996) is chosen because they have lower energy threshold than other similar ground-based air-shower detectors.[7] The differential cosmic-ray energy spectrum is given by,

$$\frac{dN}{dE} = 1.5 \times 10^{-20} (\frac{E}{10^{14.75} eV})^{-2.6 \pm 0.04} m^{-2} s^{-1} sr^{-1} eV^{-1}, \tag{3.6}$$

for $E < 10^{14.75} eV$.

Given the point of view of computation, it is not practical to simulate something that has little effect. To be more specific, cosmic rays with energies less than 10 GeV have tiny chances to trigger the detector despite the large flux and the possibility of shower fluctuations, and cosmic rays with energies more than 100 TeV rarely occur due to the steep power law index of -2.6, even though they can trigger the detector easily. A rather arbitrary energy range of 0.1 - 8 TeV is chosen as an initial guess to simulate the detector. Contributions from primaries with energies higher than 8 TeV and lower than 0.1 TeV will be explored in later runs. In addition, showers with large zenith angles, as explained in Chapter 1, are not likely to trigger the detector, even though they occupy a large phase space. An arbitrary portion of the sky with zenith angles between 0° and 60° is used. The suitability will be verified after we have examined the result.[8] Eventually, the number of showers thrown is limited by the CPU time and the disk storage space.

With these considerations in mind, 200,000 proton and 200,000 γ showers are generated, from vertical to 60° away from vertical, with primary energies varying from 0.1 TeV to 8 TeV following a differential spectral index of -2.6. The set of proton showers is to simulate the cosmic-ray background.[9] The purpose of the equivalent γ set is for comparisons and later on for the signal effective area derivation and the sensitivity calculation.

Because the azimuthal angle, ϕ, is not a factor in air shower simulations[10] under symmetry considerations, only the zenith angle, θ, is used when preparing the directional

[6]This is true only at the top of atmosphere.

[7]As will be discussed in Chapter 5, the effective area is deduced differentially in energies so other spectrum formulae can be applied later to check the differences.

[8]It will be shown later that 96% of the actual Milagrisimo triggered events fall inside the θ range of $0° - 60°$.

[9]The cosmic-ray background actually includes many different species. The suitability for using proton alone will be discussed in the end of this chapter.

[10]It is a factor, as will be shown, in the detector simulations.

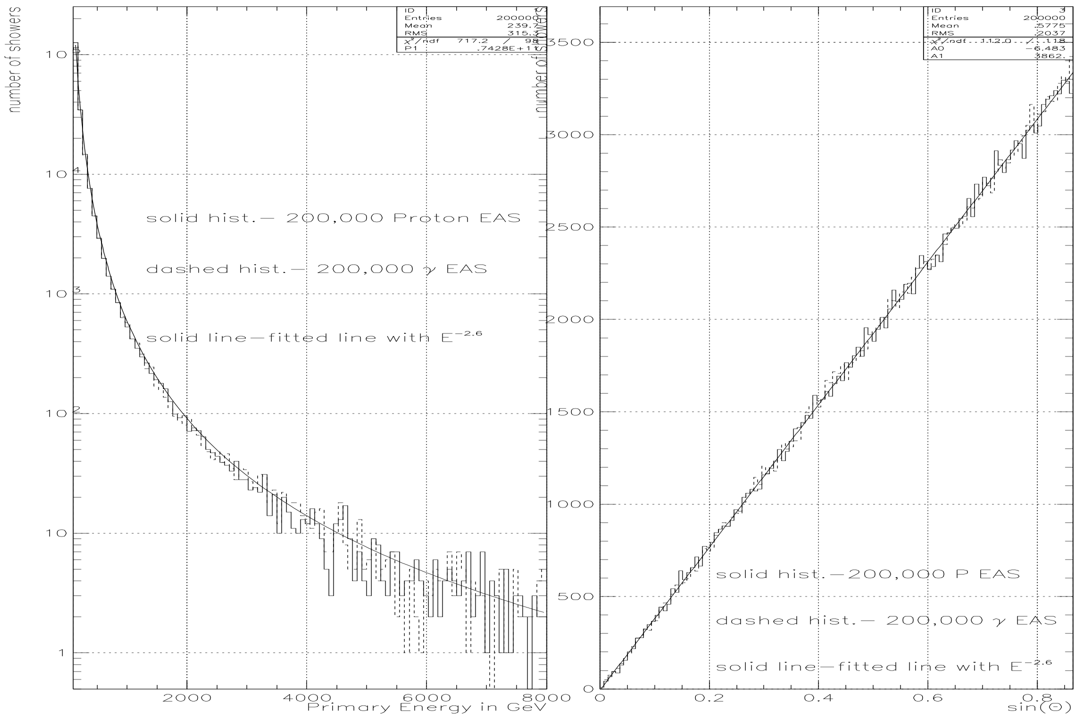

Figure 3.6: The energy and zenith angle distributions for the Milagrisimo air shower simulation.

distribution. Due to the different phase space, the number of cosmic rays thrown is not constant in θ, even though the density is.

After these 400,000 individual showers are generated, their primary energy (E) and zenith angle ($\sin\theta$) distributions are plotted in Figure 3.6 to check if they actually follow the input distributions. Smooth solid lines in the figure represent the input distributions, solid histograms are from the generated proton showers and dashed histograms are from the generated γ showers. They are well-behaved.

3.7 Detector Simulation

Unlike the complicated air-shower simulations, the detector simulation for Milagrisimo is easy to understand and is rather straightforward.

The major task of the Milagrisimo detector simulation is to follow the tremendous number of Čerenkov photons emitted along the tracks of charged particles inside the water volume in the pond. The majority of these Čerenkov photons will not fire PMTs, which are sitting at the bottom of the pond, because of: (1) the geometry constraints — many photons simply head in the wrong directions, (2) the attenuation of Čerenkov photons caused by water — some photons head in the right directions but are absorbed by water en route to PMTs, and (3) the fractional quantum efficiency of PMTs — some photons eventually arrive at phototubes but they may not fire the tubes.

In addition to the particle transport in water, GEANT supplies a built-in flag to turn on the generation of Čerenkov photons. However, due to GEANT's inefficient methods of generating and handling Čerenkov photons, it takes too much time to finish even one shower secondary particle. With the help of EGS4, we wrote our own code to do the detector simulations. Nevertheless, GEANT plays a crucial role in calibrating and verifying our custom-made simulator.

3.7.1 GEANT

For the purpose of Čerenkov light calibration, as shown in Figure 3.7, one hundred 2 GeV muons are thrown vertically onto a 100 cm thick water slab with GEANT's Čerenkov light emitting flag turned on. These high energy muons punch through the slab without changing their identities or altering their directions. This is expected since a minimum-ionizing particle, such as a muon, will not interact in water but simply lose 2 MeV in energy per centimeter of its track length.[11]

During the process, a symmetrical cone of Čerenkov light is emitted along the muon tracks. From the combined results of 100 muons, there are on average 490 Čerenkov photons emitted for each centimeter of the muon track in water (see the number in the middle plot of Figure 3.7). If an infinite water attenuation length is used in GEANT, (e.g., 500 meter in this case), all these emitted Čerenkov photons will reach the bottom of the 1 m thick water slab. However, as mentioned earlier, a PMT is not necessarily fired even if it does get hit by a Čerenkov photon. In fact, the probability is only about 20- 25% and is called the quantum efficiency for the phototubes. Different phototubes have different quantum efficiencies, which are specified by the manufacturers.

The spectrum of the Čerenkov photons from muons is not flat (the bottom plot in Figure 3.7), and there are more blue photons than red ones. Since quantum efficiencies are also wavelength dependent, we can fold in the quantum efficiencies with the actual Čerenkov wavelength spectrum to get a "PMT-detectable" photon spectrum (the lower curve[12] in the same plot). Once a "PMT-detectable" photon reaches a phototube, it is now guaranteed to fire the tube and becomes a photo electron (PE) to be amplified and the tube sends a signal out via the PMT cable. We will encounter the term, PE, many times in the rest of this study.

Since a PMT does not care if the Čerenkov light is blue or red as long as it can fire the tube, we come out with an average number of 55.5 for the number of PE per centimeter of charged-particle track.[13] This number is an important input for the detector simulation described in the next section.

3.7.2 EGS4

As drawn in the sketch of Figure 3.8, the Milagrisimo detector model consists of a water slab with a constant depth of 110 cm, twenty two $20.3cm \times 20.3cm$ (for Burle

[11] The possible process of multiple Coulomb scattering is included in GEANT as well.

[12] For simplicity, the quantum efficiency is not shown on the plot. It comes with the Burle phototubes on a data sheet. It rises from 0.0 at a wavelength of 280 nm to 0.24 at 380 nm and drops to 0.0 after 620 nm. The Hamamatsu tubes have similar profile as the Burle tubes.

[13] Compare to the previous 490 photons per cm. This is the reason GEANT is not efficient. A good simulator should only emit and follow "PMT-detectable" Čerenkov photons.

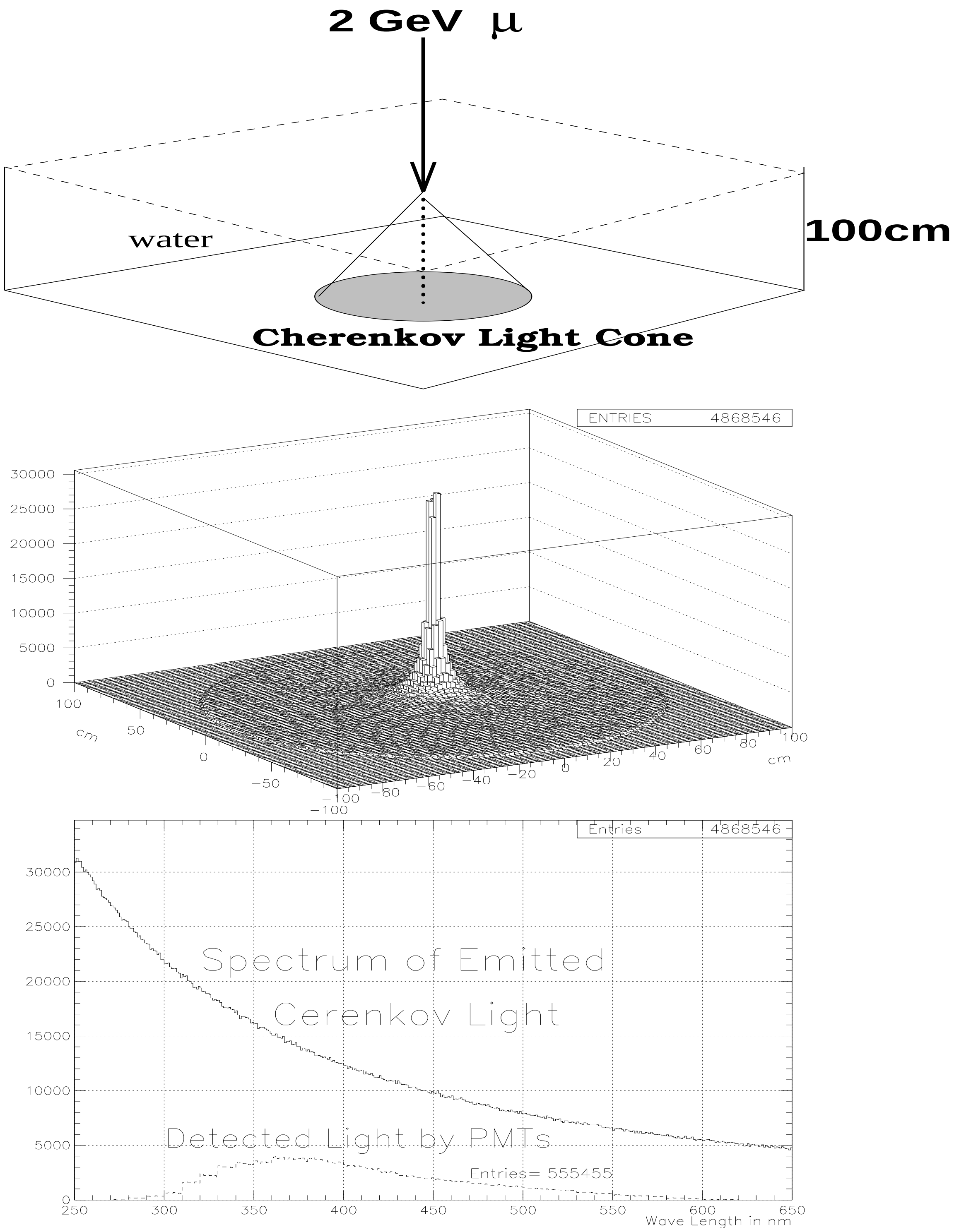

Figure 3.7: Water Čerenkov simulations with GEANT. The figures are described in the text.

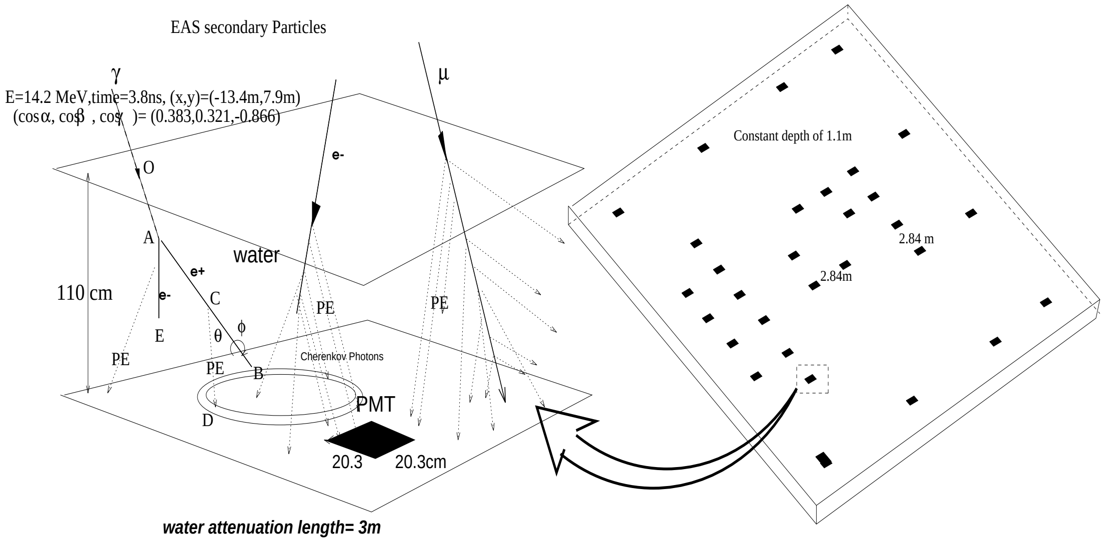

Figure 3.8: A schematic drawing of the detector simulation with EGS4. The slab to the right gives an aerial view of the entire water volume of the Milagrisimo detector. There are 28 “square dots” sitting at the bottom of the slab to represent the 28 PMTs. The area around one particular PMT is blown up to illustrate a few typical emitting processes of Čerenkov photons.

PMTs) and six $16.8cm \times 16.8cm$ (for Hamamatsu PMTs) square traps. These 28 square traps represent the PMTs and they are deployed at the bottom of the water slab located at the positions of the Milagrisimo PMTs. The unit for the distance (along x or y direction) between square PMTs is 2.84 meters, except for the corner twins — the two PMTs at the northwest corner are next to each other with no space in between.

Later on in the next chapter, from a subtle shift in the incident directions of the data, we shall learn that the assumption of constant water depth in the model is not good enough to represent the real detector. The pond bottom actually tilts toward the middle and the six Hamamatsu PMTs are floating higher than the Burle PMTs (see Figure 2.2 and Figure 4.24). Nevertheless, this simple model serves well as a first try.

EGS4 is used to proceed the detector simulation by taking over all shower secondary particles hitting the pond. In the water, EGS4 follows these electrons and photons down to 0.77 MeV.[14] During the process, whenever there is an electron with energy $E_e >$ 0.77 MeV (below which Čerenkov light cannot be generated) in the water (segments A-B, A-E in Figure 3.8), Čerenkov light is generated cylindrically and the number of photons is proportional to the total track length traveled by the electron. These Čerenkov photons are emitted at an angle, θ, relative to the electron's trajectory. The size of the Čerenkov angle, θ, depends on the energy of the electron and is given by,

$$\theta = cos^{-1}\frac{1}{1.33 \times \sqrt{1 - (\frac{0.511}{E_e})^2}}. \tag{3.7}$$

As E_e goes to infinity, the limiting value of Čerenkov angle is 41.25°. Even for a moderate

[14] Air shower photons, not Čerenkov photons.

electron energy of $E_e = 5$ MeV, the angle is almost the same (40.9°).

During the process of Čerenkov light generation, the number of emitted Čerenkov photons is actually proportional to $\sin^2\theta$ (Sokolsky, 1989). From the derived number of 55.5 PEs/cm from the previous section, we can deduce the proportionality constant via $55.5/\sin^2(41.25°) = 127.7$, such that,

$$N = 127.7 \times \sin^2\theta. \tag{3.8}$$

Note again that N is the number of Čerenkov photons emitted for each centimeter of electron path in water, corrected with the photo conversion efficiency.

After these PEs are emitted, they are subject to an average water attenuation length of 3.0 meters (refer to the end of Section 2.2). If a PE survives the water attenuation, reaches the bottom of the 110 cm deep pond, and is lucky enough to land on a square trap, the corresponding PMT is triggered and registered as one PE. If another PE hits the same trap later, the PMT adds another PE (thus, a total 2 PEs), and so on. This total PE number is the PMT pulse height.

The PMT timing (or time) is rather complicated. The original timing information stored in shower secondaries is transfered to EGS4, before EGS4 transports these secondaries in water. It can be best explained by an example in plot. As shown in Figure 3.8, a secondary photon in the air shower tells EGS4 its identity (photon), its energy (14.2 MeV), its shower time (3.8 ns, relative to the shower core), its position to enter the pond ($[x, y]$= [-13.4m, 7.9m]) and its incident angle relative to the water surface ($[\alpha, \beta, \gamma]$= [0.383, 0.321, -0.866]). EGS4 adds the original 3.8 ns to all the travel times spent from the surface of pond (point O) to the vertex where a PE is emitted (point C). Furthermore, the travel time needed for this PE from point C to the pond bottom (point D) is calculated. All these times are added together when the PE finally hits a PMT. There can be many PEs scored by the same PMT (PEs are additive), but the time of this PMT is fixed by the time of the earliest PE.

The simulation procedure for one secondary particle has now finished. After all secondary particles in the shower are processed, if there are 12 or more PMTs with non-zero PE counts, we have a triggered event.

How does our detector simulator handle muons and hadrons? Muons are understood. If they have enough energy, the simulator just drives them straight through the water volume (Figure 3.8), and emits Čerenkov photons around them. As for hadrons, in the current detector simulations they are processed as if they were muons with the same energies. This is not a good approximation. For example, a 2 GeV neutron could cause more PMTs fired than a 2 GeV muon dose, because the neutron will likely interact in water, creating several charged particles and consequently creating more Čerenkov photons. Fortunately, the 110 cm water depth is small compared to the tube spacing of 3 meters such that the localized hadronic sub-shower in water may not hit any PMT. Also, there are not many secondary hadrons in a hadronic air shower (on average 3.2 in an 500 GeV proton shower).

Horizontal muons generated from irrelevant large angle showers may fire some phototubes and contaminate a triggered event. The main consideration is that the Čerenkov light from these flat-going muons is likely to be "totally reflected" by the water boundary instead of absorbed by the black cover and liner. Nevertheless, as shown in Figure 4.8 (a) and (e) and explained in Section 2.4, the contamination is minimal.

3.8 Result and Interpretation

After the air shower sets are completed, there are 200,000 proton and 200,000 γ showers with different primary energies and different zenith angles. However, they all have the identical shower core position, i.e. $(0, 0)$, and the same azimuthal angle, $\phi = 0°$.

To be realistic, showers cannot all land at the center of the pond and their cores have to move around. Showers with their cores outside of the pond can trigger the detector as well. Secondly, showers cannot always come from a same side (e.g., east), even if they have different zenith angles. With these concerns, each shower is randomly assigned a core location (X_c, Y_c) over a large square area of $180m \times 180m$ centered on the pond, and is randomly assigned an azimuthal angle ϕ between $0°$ and $360°$. The coordinate system is defined as that shown in Figure 2.3. Once a random (X_c, Y_c) and a random ϕ are chosen for a particular air shower, the values of coordinates (x, y) and incident angles (α, β, γ) for all its secondary particles are geometrically transformed accordingly. The new transformed coordinates and directional angles for secondaries are inputs for the detector simulation described in the previous section.

Because a shower, after rotating to a new ϕ and shifting to a new core location, looks very different to the detector, we can take advantage of this fact and use the same air shower many times by just assigning new azimuthal angles and new core locations. However, we have to be careful not to overuse them to avoid any bias. After calculating the ratio of the physical size of the detector (600 m^2) to the size of the area over which showers are thrown (32,400 m^2), the same shower is chosen to reuse 50 times. This minimizes the possibility for the detector to see the same portion of air shower.

After throwing each individual shower 50 times, 10 million virtually different proton and 10 million γ air showers are fed into the detector simulation to get triggers. There are 2,657 proton triggers and 1,696 γ triggers.

As mentioned in the previous section, because the pond bottom is not perfectly flat but is tilted toward the middle, and the 6 Hamamatsu tubes are afloat at a shallower depth than the Burle tubes, a sizable directional preference is found during the data reconstruction. This will be explained in the next chapter. To accommodate this adjustment, the same sets of the 20 million showers were rerun through an improved version of the detector simulation. The new version is implemented with the true depth for each individual PMT as shown in Figure 4.24. The revised results for this improved detector simulation are: 2,857 proton triggers and 1,791 γ triggers.

To avoid repetition and to be able to do direct comparisons, the event properties for Monte Carlo results are postponed to be shown at the end of next chapter, where real reconstructed data are available. Only the trigger rate will be calculated here to conclude this chapter.

3.8.1 Effective Area and the $cos\theta$ Factor

The definition of effective area is similar to that of cross section in high-energy physics. Basically, we randomly cast many air showers, N, in a practically large[15] area, A,

[15] A has to be large enough such that the probability for showers outside of A to trigger the detector is at least two orders of magnitude smaller than those right above the detector.

and count the number of triggers, n, in the end. The effective area is given by,

$$A_{eff} = \frac{n}{N} \times A.$$

Generally, showers come to the detector from different directions. To account for the projected area of the region, an extra cosine factor has to be included for the area A, according to the meaning of effective area. An example will clarify this point: if 10 triggers occur in the case of randomly throwing 100 vertical showers on an area of 1 m^2, the effective area is 0.1 m^2; however, if 10 triggers occur after throwing 100 60° away from vertical showers on 1 m^2, the effective area is only 0.05 m^2, because these tilted showers simply see a smaller area before they try to trigger it.

After correcting with this cosine factor for each trigger, the effect areas for proton EAS and γ EAS (with energies between 100 GeV and 8 TeV, and with zenith angles between vertical and 60° away from vertical) are

$$A_p = \sum_{i=1}^{2857} \frac{\cos\theta_i}{10^7} \times (180m \times 180m) = \frac{2581.7}{10^7} \times (180m \times 180m) = 8.36\ m^2, \tag{3.9}$$

and

$$A_\gamma = \sum_{i=1}^{1791} \frac{\cos\theta_i}{10^7} \times (180m \times 180m) = \frac{1688.7}{10^7} \times (180m \times 180m) = 5.47\ m^2. \tag{3.10}$$

Notice that the improved depth-corrected version of the detector simulation is used to derive the numbers above.

It is intriguing that the effective area for proton showers turns out to be larger than that for γ showers, whereas, as pointed out earlier in this chapter, the shower size is the other way around. First of all, the effective areas are primary energy dependent. Second, in the earlier case, only vertical showers were discussed. The zenith angle plays an important role in changing the all-angle effective area. At larger zenith angles, the effective area for protons is larger than for γ showers.[16]

3.8.2 Trigger Rate

After deriving the effective area, all we need to calculate the trigger rate is the real air shower flux. From Tibet's cosmic-ray flux formula, Equation 3.6, the total flux for energies between 100 GeV and 8 TeV and for zenith angles between 0° and 60°, can be simplified to,

$$J_{0.1-8TeV,0-60^\circ} = 16.6\ m^{-2}s^{-1}. \tag{3.11}$$

We can therefore estimate the trigger rate for Milagrisimo to be,

$$Trigger\ Rate = 16.6 \times 8.36 = 139\ s^{-1}. \tag{3.12}$$

The actual trigger rate in the experiment is 125 s^{-1}.

There are several comments to make here for discussion. First, the assumption that all showers come from within 60° in zenith angles is not far off because, from the

[16]This fact is quantitatively shown in Figure 5.10.

real data, as shown in Figure 4.22 (e), the angle range of 0-60° actually covers 96% of all triggered events.

Second, the trigger contributions from showers with energies above 8 TeV and below 0.1 TeV need to be explored. In the section on effective area in Chapter 5, more showers at both ends will be simulated, and the results are put together in Table 5.1. Adding the contributions from the two ends will increase the calculated trigger rate, and it actually turns out to be 206 (see Equation 5.3).

Third, the Tibet formula is for the total cosmic ray flux, including protons, helium nuclei, iron nuclei and all other species. A series of balloon flights between 1979 and 1981 made by the JACEE collaboration well measured the energy spectra above 1 TeV of proton and helium nuclei in the primary cosmic rays (Burnett, 1983). At 1 TeV, the ratio between protons and helium is about 3 to 1. After we consider all other cosmic-ray species, the composition of cosmic rays at TeV to PeV energies is approximately 50% protons, 25% α-particles, 13% CNO, and 13% Fe (Sokolsky, 1989). It is complicated to separately simulate air showers from these heavy nuclei. From the nature of air-shower development, an 1 TeV helium nucleus is approximately equivalent to four 0.25 TeV protons (Gaisser, 1990). Consequently, the 1 TeV helium has less penetrating power and less triggering ability than a 1 TeV proton.[17] The fact that we used all proton showers instead of 50% protons, 25% helium nuclei, and 25% other heavier species significantly increases the calculated trigger rate.

With the third factor in mind, the simulated results agree adequately with the trigger rate of the real experiment.

[17] The effective area at 1 TeV is much more than 4 times the effective area at 0.25 TeV (see Figure 5.1).

Chapter 4

Shower Reconstruction

The raw data coming out of the FASTBUS cannot be used directly to search for γ -ray bursts. They need substantial refinement before we can extract and derive the properties of a primary particle, and these properties (ideally, the primary particle's energy, identity, and direction) are what we really need before we can start to look for γ-ray sources. Furthermore, the apparent raw data, most of the time, do not reveal the needed information about the secondary particles either, but contain noise, false signals,[1] electronic slewing and other misbehaviors. In this chapter, many efforts are made to understand and correct the raw data, as well as to reconstruct the properties of primary particles.

To calculate the primary energy of an air shower, one has to estimate its shower size by fitting its pulse height distribution. It is difficult to perform the pulse-height fit because the distribution is lumpy and irregular on a shower-by-shower basis, and the area where shower secondaries land is much larger than the detector. Even if the shower size were accurately determined, its primary energy estimation could still be off easily by an order of magnitude (see the bottom two plots in Figure 3.4). During the development of an air shower, only a small fraction of the energy makes it through the 21 radiation length of air and this energy is subject to large fluctuations, particularly if the detector has a low trigger threshold. Nevertheless, the average trigger energy can be estimated by Monte Carlo simulations.

Can Milagrisimo tell whether a particular shower is γ-induced or proton-induced? Some proton showers[2] have muons hiding among their shower secondaries. If the detector is able to record and identify muons, the associated hadronic showers can thus be identified and rejected. Milagrisimo does not have such ability to detect muons.[3] And, most of all, on an event-by-event basis, it is very difficult, if not impossible, to pick up any "γ signature" from shower secondary particles.

The only thing Milagrisimo can attempt to reconstruct from the raw data is the original directions of primary particles. As stated earlier (on page 15), after we reconstruct the original directions of all air showers, the signals (γ primaries) from a source will be buried amid a homogeneous sea of cosmic-ray background. Fortunately, signals always pile up around a fixed point since they are supposedly biased by certain underlying influences,

[1] Prepulses, afterpulses, muon hits, etc..

[2] Monte Carlo simulation shows less than 40% of triggered events have one or more muons hitting the pond.

[3] As described in Section 1.7, Milagro has the ability to identify muons.

while background events are random. After enough events, the location of the signals stands out. Also in the same section, we closely linked the primary shower direction to the relative times among detected secondaries (page 15). A full explanation is given below.

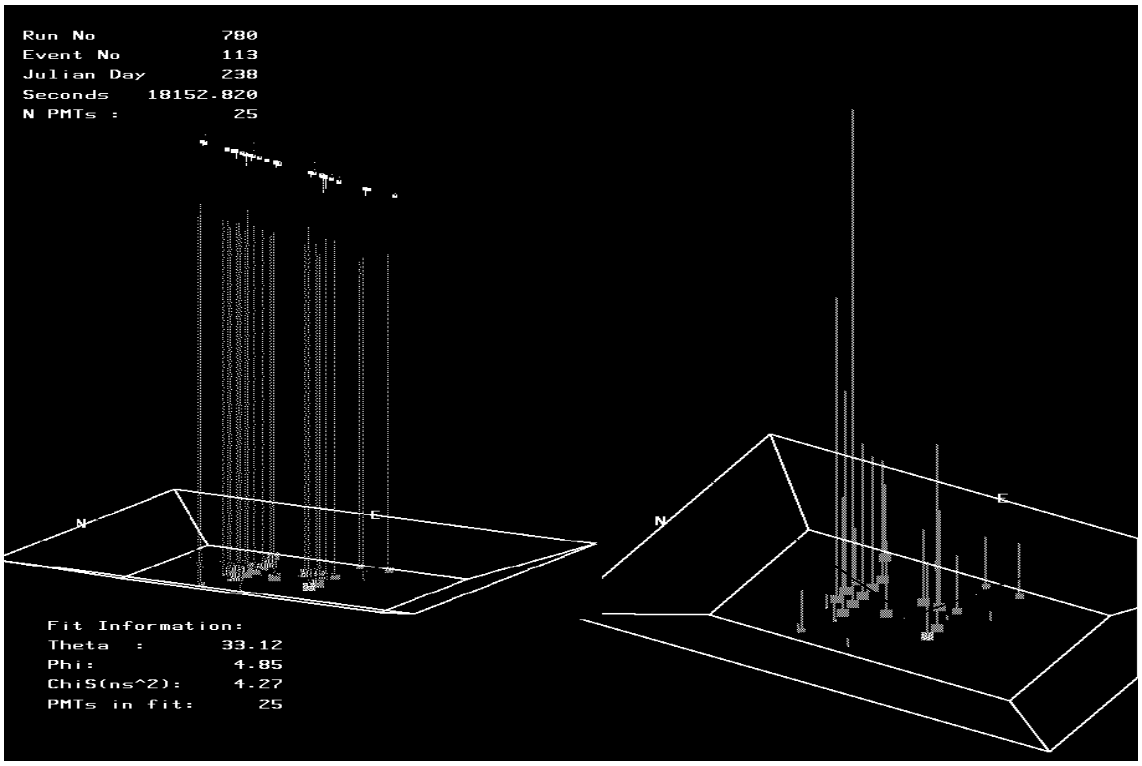

Figure 4.1: A Milagrisimo visual event display. To the left is a timing plot with a fitted plane sitting on the top of the timing lines. The small segments connecting to the defined plane are residues from the fit, which are the differences (T-Chi) between individual timing lines and the common fitted plane. The picture to the right is the pulse-height distribution for all fired PMTs. The taller the bar is, the more energy is deposited in the phototube.

Referring to the EAS drawing on page 14, we learn that the secondaries in an EAS do not hit the ground at the same time, especially when the air shower comes in at an angle. Some secondaries in the shower arrive earlier and some arrive later. We state that these secondaries have timing differences. The two images in Figure 4.1 are from a typical Milagrisimo event display. The one at the left is the timing display and the one at the right is the pulse height distribution. The vertical lines in the timing display, that stand above fired PMTs, signify the arrival times of recorded secondaries.[4] The shorter the bar is, the earlier the hit arrives. If we draw the timing lines to scale and make 1 m = 3.3 ns, we can convert the concept of time into a third coordinate, such that the direction defined by the timing lines is the true space direction of the air shower. In the image shown, it seems rather obvious that the shower direction is normal to the plane that is defined (fitted) by all those timing lines.

In order to perform a straightforward least-square fit to a plane, all we need to

[4]They are actually the arrival times of detected Čerenkov photons from shower secondaries.

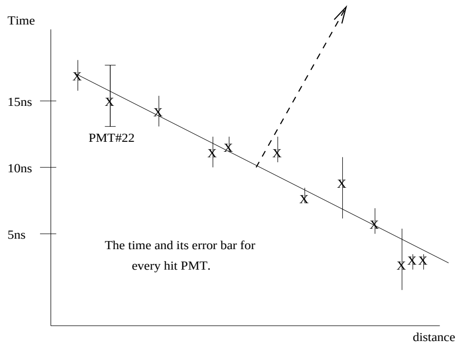

Figure 4.2: There are three inputs needed to fit a shower: PMT positional geometry, PMT times, and PMT time error bars.

know is the lengths of these timing lines (up to a constant since only the relative timing matters), and the uncertainties in them (errors for the times). The error bars of timing lines are not shown in the interest of clarity.[5]

In the simpler example of an one-dimensional case in Figure 4.2 , an air shower fires 13 PMTs. Their times (in nanoseconds) with error bars (in ns, too) are plotted against the 1-dimensional separation (in meters) between PMTs. Given these 26 numbers — 13 times and 13 time error bars, we can determine a best line (a plane in the real 2-D case) to represent these 26 inputs, using a fitting method like least squares or maximum likelihood. The 13 time error bars give different weights for the 13 time values during the fitting procedure.[6]

By now, if the task of Milagrisimo reconstruction just means getting the primary directions, the complete method to accomplish it is to fit the PMT times. Therefore, all we have to do is just read out from the raw data, presumably, PMT times and their errors event after event, and fit them with a plane! That is exactly right, in concept.

Some visual checking of the drawing will illustrate that the final fitted direction is sensitive to small variations in those 26 values. If, for any reason, one of these numbers misses by a few nanoseconds, the resulting direction may differ by a few degrees, especially since the detector ($20m \times 30m$) has a rather small lever arm. That "few degrees" turns out to be unacceptably large. Later on in the source analysis, whether or not a source is detected depends on that "few degrees." For example, if the angular resolution drops from 1° to 4°, the significance will drop from 4 standard deviations (sigmas) to 1 sigma for the same signal.

We have to determine accurately the PMT times and their errors. Most of the rest of this chapter is devoted to extracting these quantities from the raw data. The raw data (and the experimental instruments) require careful study, and the timing error, as will be explained shortly, is strongly correlated to the PMT pulse height.

[5]It is better to view it on a computer monitor; a different color is used to display the error bars, and the entire image can be rotated in 3-D with a mouse.

[6]Later on in Section 4.5.1, the least-square method will be elaborated when we actually fit the air shower.

4.1 The Origin of Timing Errors

The spread of shower secondaries is caused by fluctuations during the shower propagation.[7]

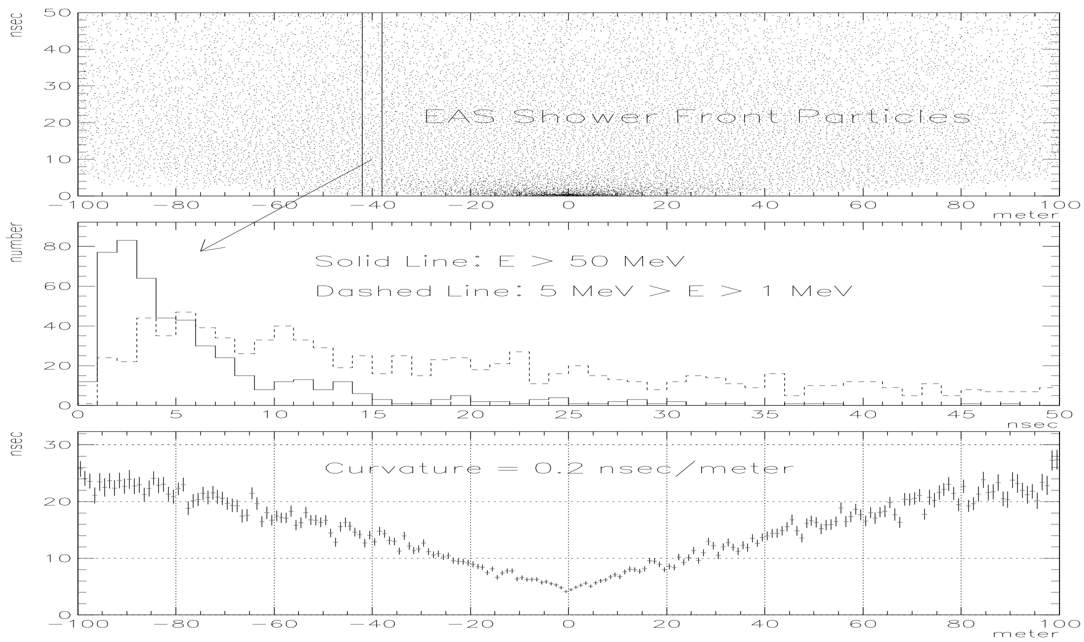

Figure 4.3: A snapshot of secondary particles from a simulated γ shower. X-axis is the coordinate to shower core ranging from -100 meters to 100 meters. Y-axis represents the timing delay in nanoseconds. The middle plot is a histogram sliced off from the scatter plot at $-42m < x < -38m$. Shower secondaries (electrons and photons enter together) in two different energy groups are shown. The bottom plot is a profile chart to summarize the top plot in the sense that every point represents the mean times of all secondaries (for all energies) in the corresponding x bin.

As an example, a 10 TeV γ vertical shower is generated with GEANT. Right at the moment when the shower core hits the ground, we freeze the shower and take a side-view snap shot of it. The resulting scatter plot is shown in the top row of Figure 4.3 . For clarity, only the x dimension is shown. Notice that the shower front (i.e. the lateral spread) is not flat, but has a curved shape away from the center, and the shower secondaries are not all packed together in a thin layer (i.e. the longitudinal spread), but they have a characteristic timing distribution with a tail. In order to examine the timing structure more closely, a slice from the scatter plot is selected to include all particles with x coordinate between -38 meter and -42 meter as shown. The timing structure of secondaries depends on their energy. For clarity again, only two energy categories are selected from this slice of particles, and are plotted in the middle chart of Figure 4.3 : one with particles' energies greater than 50 MeV,

[7]For example, the fluctuations in directions and step sizes among millions of multiple coulomb scattering processes.

and the other one with particles' energies between 1 MeV and 5 MeV. Those secondaries with higher energy stay closer to the shower front, and the spread of their times is narrower than those in the other group with lower energy. Low energy particles scatter more and lengthen their flight paths.

When these secondaries go into the water producing Čerenkov light, which in turn produces PMT pulses, the timing structure in the air shower is very much preserved. For example in an air shower, imagine there are a few hundred 50 MeV photons, at $(x, y) \sim (20m, 20m)$, distributed similarly to the middle histogram in Figure 4.3 (with a width ~ 5 ns). If we throw this same shower 100 times through the detector and examine the response from a particular PMT which is near the entry point of $(x, y) \sim (20m, 20m)$, the resulting distribution of the PMT's times is similar to that at the air-shower stage[8] due to the simple sampling processes. If the PMT gets a value of 3 ns one time, it may get a different value of 5 ns another time, but it is not likely to get a value of 30 ns. On the other hand, a 30 ns fluctuation looks normal for the case of a 1 MeV photon. The width of the PMT time distribution reflects how confident the read-out value of the time is, or the error for the PMT's time.

It is clear now why the PMT's timing errors are strongly correlated to the PMT's PE values.[9] It results directly from the nature of air showers. Also shown in the bottom plot of Figure 4.3 , the peak position (not the width) of the timing distribution (including all energies) shifts toward the positive direction (i.e. is delayed), as the distance from the shower core increases.

4.2 Shower Core Consideration

This section will deviate from the main course of shower timing, and discuss the problem introduced by the shower core location. The curvature issue discussed in the last section (the shower front is not flat) has a major impact on the topic of shower reconstruction.

Figure 4.4 displays an exaggerated shower with two scenarios: case A where the shower core strikes at the center of the pond, and case B where the core hits outside of the pond. The primary energy in case B is larger than that in case A to be able to trigger the array with the same detector response (number of fired tubes). In case A, the direction obtained from the plane fitting is close to the real shower direction. However, in case B, the pond sees a tilted portion of the same air shower, and in turn the fitted direction acquires a pointing error and deviates from the true shower direction. Once the shower core falls completely outside, to first order, the error does not get worse.

If we can somehow locate the shower core position, the distance from each hit PMT to the shower core can thus be determined. In turn, a curvature correction can be made to each counter's time to level off the tilt before the normal shower fit. In this way, the pointing error mentioned can be minimized.

As said earlier, we have to look at the PMT pulse-height distribution to search for the shower core. As shown on the right-hand side picture of Figure 4.1, the pulse

[8]The PMT time distribution will be further broadened by $\sim$1 ns because of the extra fluctuations introduced in the γ conversion depth. The speed of a secondary γ particle is faster than that of the Čerenkov light.

[9]An exception can occur when a low energy γ converts right at a phototube and produces a large output.

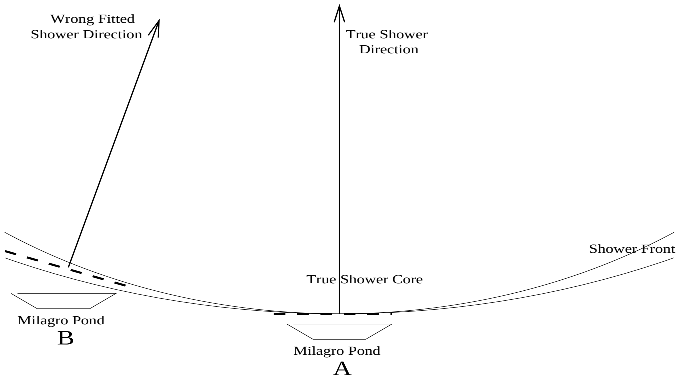

Figure 4.4: Core inside pond or core outside pond can make a difference. The true shower core hits under the middle arrow.

height distribution of the event might have persuaded us already that, the shower core lands near the hottest counter. We could fit the pulse height distribution with the NKG lateral distribution discussed in Section 3.4, or with a two-dimensional Gaussian function to find the shower core. However, with only a handful of tubes (12 - 28) spread out in a small area, it is difficult to perform these formal fits on Milagrisimo events.[10]

As a first try, a quadrant test is applied to see if Milagrisimo can yield some information about the shower core. Simulated triggered events (see Section 3.8) with known core positions (X_{core}, Y_{core}) are examined to find their fitted cores (x_c, y_c) by just calculating the center-of-mass values among PMT hits (PE_i, and (x_i, y_i)),

$$x_c = \frac{\sum_i^N PE_i \cdot x_i}{\sum_i^N PE_i} \qquad , and \qquad y_c = \frac{\sum_i^N PE_i \cdot y_i}{\sum_i^N PE_i}.$$

For a minimal agreement, we want to see that, (x_c, y_c) and (X_{core}, Y_{core}) should fall in the same quadrant. To eliminate the ambiguous cases around boundary regions between the four quadrants, I select only those events with $|X_{core}| > 5m$, and $|Y_{core}| > 5m$. As seen from

	γ triggers	proton triggers
all triggers in Monte Carlo events	1696	2657
triggers with $\|X_{core}\| > 5m, \|Y_{core}\| > 5m$	1073	1946
(X_{core}, Y_{core}) and (x_c, y_c) fall in the same quadrant	371(35%)	550(28%)

Table 4.1: Results of the quadrant test for shower core search.

the result in Table 4.1, this simplest core finder fails badly. From the Monte Carlo result in Figure 4.3, the shower curvature is estimated to be ~0.2 ns per meter. Once the core hits completely outside the pond, the worst case timing difference introduced by the shower curvature is 6 ns across the 30 meter wide detector. This is equivalent to a 3.1 degree in

[10]It is harder to locate cores for hadronic events than γ events because they spread more widely than γ events. Also, some PMT hits in hadronic showers are caused by muons. In some worst case scenarios in Milagrisimo, the light output from through-going muons may be big enough to fake shower cores.

pointing error. This is an extreme case, though. In reality, the situation is not like that. First, the majority of triggers, which peak at 12 fired PMTs, have a "hit" area with a mean radius less than 8 meters, especially since the working Milagrisimo PMTs are not evenly distributed (see Figure 2.3). Second, in the case of a steep source energy spectrum, such as the flux of GRBs (Equation 1.1 or Equation 1.2), Monte Carlo study shows that the lower-energy triggers with their cores inside the pond outnumber the higher-energy triggers with their cores outside the pond.[11] Third, as will be shown in the next chapter, the overall angular resolution for Milagrisimo is estimated to be $2.1°$. That is too large to be fully sensitive to the core effect.

The actual size of the systematic error in pointing caused by the nature of shower curvature has yet to be determined. On the other hand, discussions in Section 4.7 and Section 4.10 will put an upper limit on the "total" systematic error of the detector.

4.3 PMT Timing Determination

The raw data in FASTBUS are accumulated from 40 electronics channels.[12] The TDC output is zero suppressed, whereas the ADC output has pedestal counts even without real signals. For a triggered event with N PMT hits, the data consist of N meaningful ADC pulse height counts, $40 - N$ ADC pedestal counts, N sets of TDC counts (each set may contain 2, 4 up to 16 timing edge values) and the trigger time (8 bytes in size, with a precision of a microsecond). The PMT timing information is stored in the set of TDC edges.

4.3.1 TDC Conversion Factor

According to the manufacturer, LeCroy, each TDC count in the module 1877 measures 0.5 ns. A calibration scheme is undertaken with a fast pulse generator controlled by a Macintosh Lab-View system. The pulse generator sends a train of 18 consecutive narrow pulses (few nanoseconds), with a 100 ns delay between leading edges of two adjacent pulses. These pulses are sent in to the 1877 module to read out their rising edges. Just by listing these data, we can clearly see the relationship between TDC counts and ns (Figure 4.5 (a), and (b)). The conversion factor is obtained from the slope of the fitted line. After fitting the time slope for each TDC channel, we plot the time scale factor over all 40 channels on the module in use (Figure 4.5 (c)). Note the scale of the y-axis. The calibration shows a tiny systematic error from the claimed value of TDC conversion factor: 0.5 ns; nevertheless, it is good enough for all purposes[13] to use 0.5 ns per count as the TDC conversion factor for all 28 channels.

[11] For example, in the case of the 0.1- 8 TeV proton shower simulation in Chapter 3, there are 287 triggers with cores "inside" the pond and with energies between 0.1 and 1.1 TeV while there are 115 triggers with cores "outside" the pond and with energies between 6.1 TeV and 7.1 TeV.

[12] Only 28 tubes worked through the whole experiment.

[13] A possible error of 0.1 ns for the largest PMT timing difference of 100 ns across the Milagrisimo detector is far less than the random errors introduced in the air shower, water, PMT, cable, or electronics.

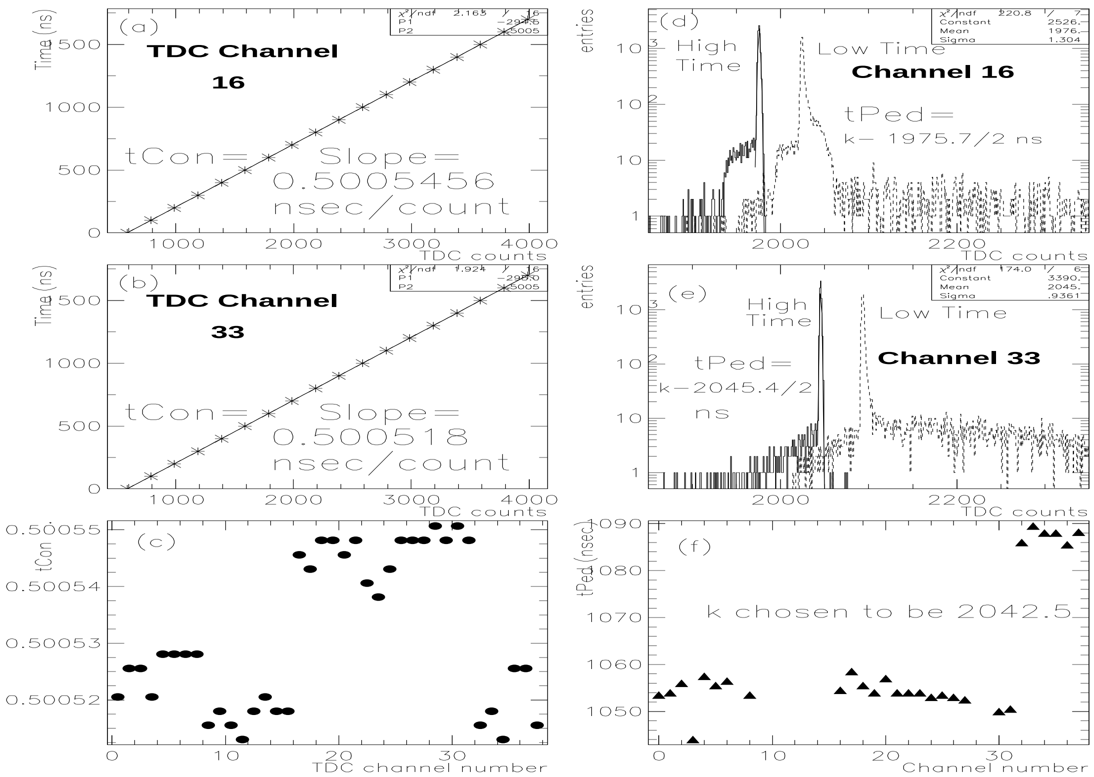

Figure 4.5: TDC conversion factors and TDC pedestals. The upper two rows are plotted from channel 16 and 33 respectively. The two charts at the bottom row show values of all 28 channels.

4.3.2 Time Pedestal

If we were to shoot detectable photons *simultaneously* on all 28 PMTs to make an artificial event, the 28 read-out times from data acquisition channels would still have a finite spread. During the signal transfer processes in the apparatus, different channels have different time delays. These differences have to be eliminated in order to have a common "time zero" for every channel. The different timing delays are accumulated from different electron transit times inside the PMTs (due to different operating voltages and different phototube lengths), different cable lengths from the PMTs to the electronic boards, and different paths in electronic circuits between cable-ends and FASTBUS modules. After the Milagrisimo experiment finished data taking in early July, 1996, we drained the water in the pond, but left the 28 PMTs where they were and left the data acquisition system unchanged to do the timing calibration. An LED system was set up to measure these timing differences among different channels.

Inside the dark pond with the cover inflated (see Figure 2.1), we manually placed a fast green LED on the top of a chosen PMT. A special pulse generator drove the LED with narrow (<10 ns) but large (>10 V) pulses at 10 Hz, and at the same time the generator opened the ADC gate and sent the TDC common stop. As described in Section 2.4, the

TDC common stop was normally provided by the summed voltage from the digital board to trigger the readout. Thus, essentially the same data acquisition system (and electronics) took data at 10 Hz with the chosen phototube illuminated by the LED photons. A few thousand triggers were taken and read out. Then, the LED was taken to the next PMT to calibrate its time pedestal, while everything else remained unchanged. Since an LED signal was essentially a blast for the PMT, the resulting pulse from the PMT was equivalent to at least a few hundred PEs. Consequently, the TDC values for these PMT pulses were all 4-edge sets, with both low-crossing edges (edge "a" in Figure 2.6) and high-crossing edges (edge "c" in the same drawing) present.

The distributions of both high-crossing edges and low-crossing edges are plotted in Figure 4.5 (d) and (e), for channel 16 and 33, respectively. The dotted peaks are from low-crossing edges, and they have a few (note the log scale) entries with larger TDC values. These are prepulses. Recall that earlier hits have larger TDC values (refer to Section 2.3) because of the common-stop feature in the LeCroy module. As will be explained in the next section, large pulse-height hits are prone to have prepulsing problems, so the low-time edge tends to be earlier than it should. Nevertheless, the TDC pedestals can be unambiguously defined by fitting either the high-crossing or the low-crossing peaks. The results from fitting the high-crossing peaks are shown in Figure 4.5 (f). In the examples of channel 16 and channel 33, the fitted high-crossing peaks sit at 1975.7 and 2045.4 (TDC counts) respectively. Even though the absolute value of the time pedestal does not change the result in shower-direction fitting, it is clumsy to bear a large common baseline value. The time pedestal, tPed, can be rearranged as $tPed = k - \frac{1975.7}{2}$ (ns) (for channel 16), where $k = 2045.2$. Thus, each TDC datum, t_{TDC}, can be corrected by $t_{true} = \frac{t_{TDC}}{2} - tPed$ (ns), and the baseline for t_{true} will turn out to be approximately zero. This is done by the carefully chosen value of k. As seen in Figure 4.5 (f), the pedestal differs channel by channel, but channel 32–37 (Hamamatsu PMTs) have higher values of tPed than those in channel 0-31 (Burle PMTs). This is because Hamamatsu phototubes use lower operating voltages than those of Burle PMTs.[14] A photo electron takes longer time to reach the bottom in a Hamamatsu PMT than in a Burle PMT.[15]

4.3.3 Closer Look at Timing Edges

Now that the time pedestals are available, we can go ahead to determine the time of each PMT hit, provided that its time edges are "clean." This section describes how to select clean edges, and how to interpret or correct dirty ones.

As sketched in Figure 2.6, the signal pulses from PMTs eventually go into the front end boards. After processing a PMT pulse, the board sends a two-edge logic pulse (for a small pulse) or a four-edge sequence (for a large pulse) to the TDC 1877 module in the corresponding channel. In Figure 4.6 , the process is blown up in detail to show how the TDC timing edges are formed. Notice how the edges are labelled (0, 1 for a two-edge hit, and 0,1,2,3 for a four-edge hit). The same numbering scheme will be used throughout this chapter.

This consideration should have covered all cases. However, as we decode the raw

[14] Even though the Hamamatsu tubes are smaller than Burle tubes.

[15] The minus sign in the tPed calculation changes the original polarity of pedestal, so later entries have larger values in tPed.

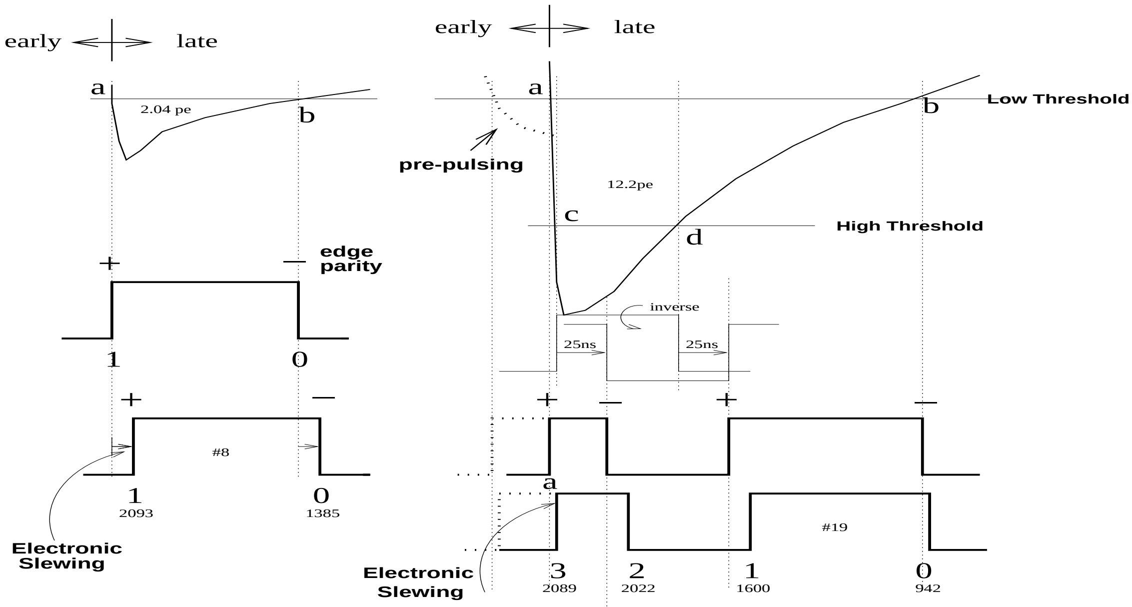

Figure 4.6: The TDC timing edges are formed from analog PMT pulses. On the left is a small pulse, and on the right, a large one. This is a more refined drawing of Figure 2.6. The dotted small pulse before the large one, is a prepulse. Electronic slewing is caused in the electronics board during the threshold crossing. Smaller pulses have larger slewings.

data, there are PMT pulses with 5 edges, 6 edges or even up to 16 edges present (see the left column in Figure 4.7 for relative percentages). What causes these noisy data? For the worst case, we can always discard them, but is a 2-edge (or 4-edge) hit truly a 2-edge (or 4-edge) hit?

Consider a typical Milagrisimo run, Run 780, as an example. Run 780 consists of 10^6 triggered events or 18.2×10^6 TDC hits. Referring to Figure 4.7 again, we find out that, fortunately, only 2.1% of them are neither 2-edge nor 4-edge hits. For the time being, they are ignored to avoid complications. Now we have to examine all 2 and 4 edge hits by filtering them with certain rules.

Notice that, as seen in Figure 4.7, for both 2-edge and 4-edge hits the parities of edges (leading edge or trailing edge) are also recorded in the raw data. The first rule, which is marked as "Parity" on the graph, is that, a good set of edges has to start with a rising edge (+) then alternate after that. The majority of hits for both 2-edge and 4-edge cases passed this somewhat trivial cut as can be seen in the branching chart in Figure 4.7. By plotting and checking some combination distributions of these edge values, we can make several cuts on PMT hits based on the resulting statistics from these distributions.

Again, I take a Burle-tube channel and a Hamamatsu-tube channel as examples to plot these edge-combination distributions in Figure 4.8 . The edge assignments are the same as those in Figure 4.6. For examples, edge #2 in a 4-edge hit is the starting time for a high-crossing edge, and edge #0 is the ending time of a low-crossing edge for both 2-edge and 4-edge hits. The letters in Figure 4.8 are arranged to be the same as those in Figure 4.7, and these rather complex plots in Figure 4.8 are just graphical explanations

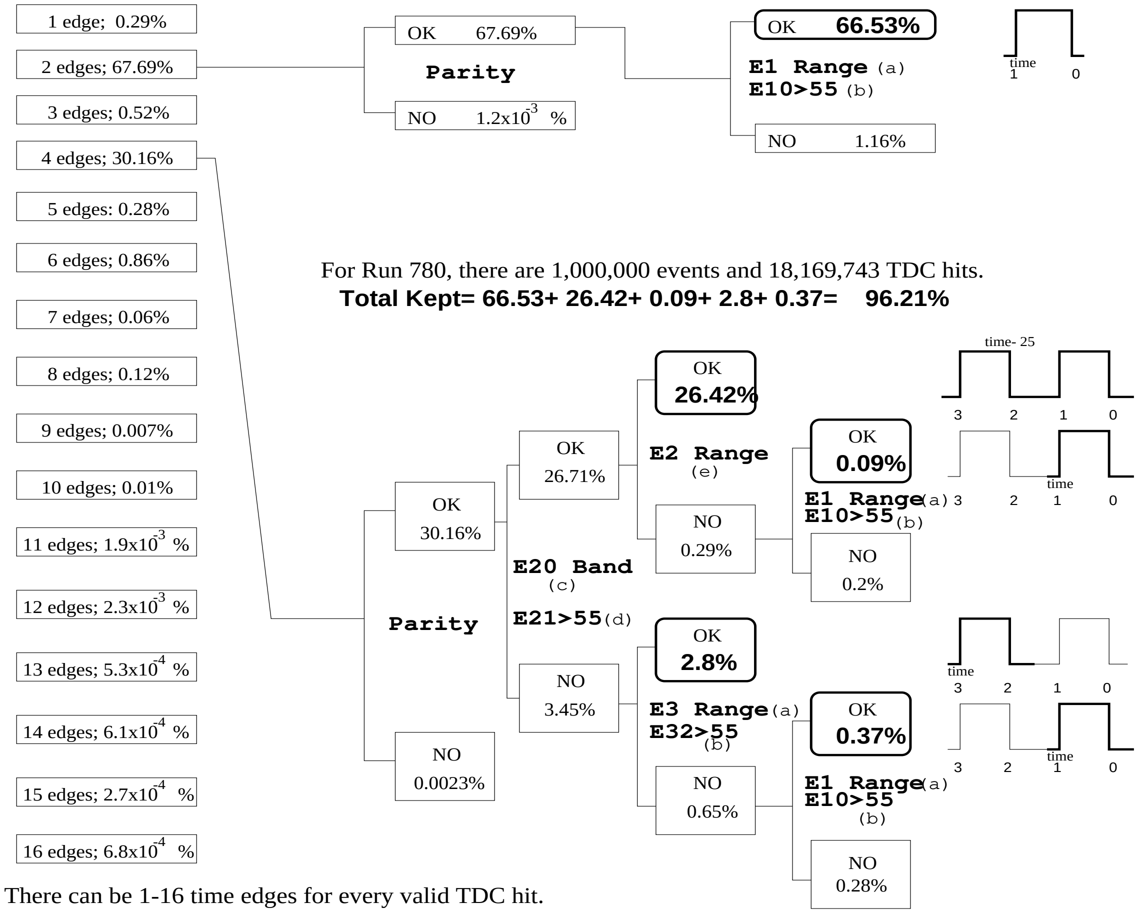

Figure 4.7: The branching charts show the surviving percentage after various selection cuts. To the far right, final edge interpretations are summarized. The edges highlighted in bold faces are used and the edge with a "time" printed by it is the final time of the hit. The figures are described in the text.

for those cuts made in Figure 4.7. For example, Figure 4.8 (e) tells what the "R2 Range" requirement in Figure 4.7 is. In terms of notations, E2 means the TDC counts of edge #2, E10 stands for E1 - E0 (recall that earlier edges have larger values), and so on. These five cuts are important and need to be explained clearly here.

The first cut, (a), which is the low start edge range cut — E1 (or E2, or E3, whenever it represents the leading edge), comes from the fact that it takes at most ~100 ns for a tilted shower to cross the detector. If a leading edge comes 600 ns (in a Burle channel) after the trigger time, it is probably too late to be related to the same air shower. It may be noise or a signal from another air shower.

The second cut, (b), requires that E10 (or E21, or E32, whenever it represents the pulse span of the low ToT) has to be longer than 55 TDC counts (or 27.5 ns) because the width of a valid edge pair cannot be shorter than 25 ns, which is hardwired on the electronics board.

The third cut, (c), constrains the ranges of the total span in a 4-edge hit. It would

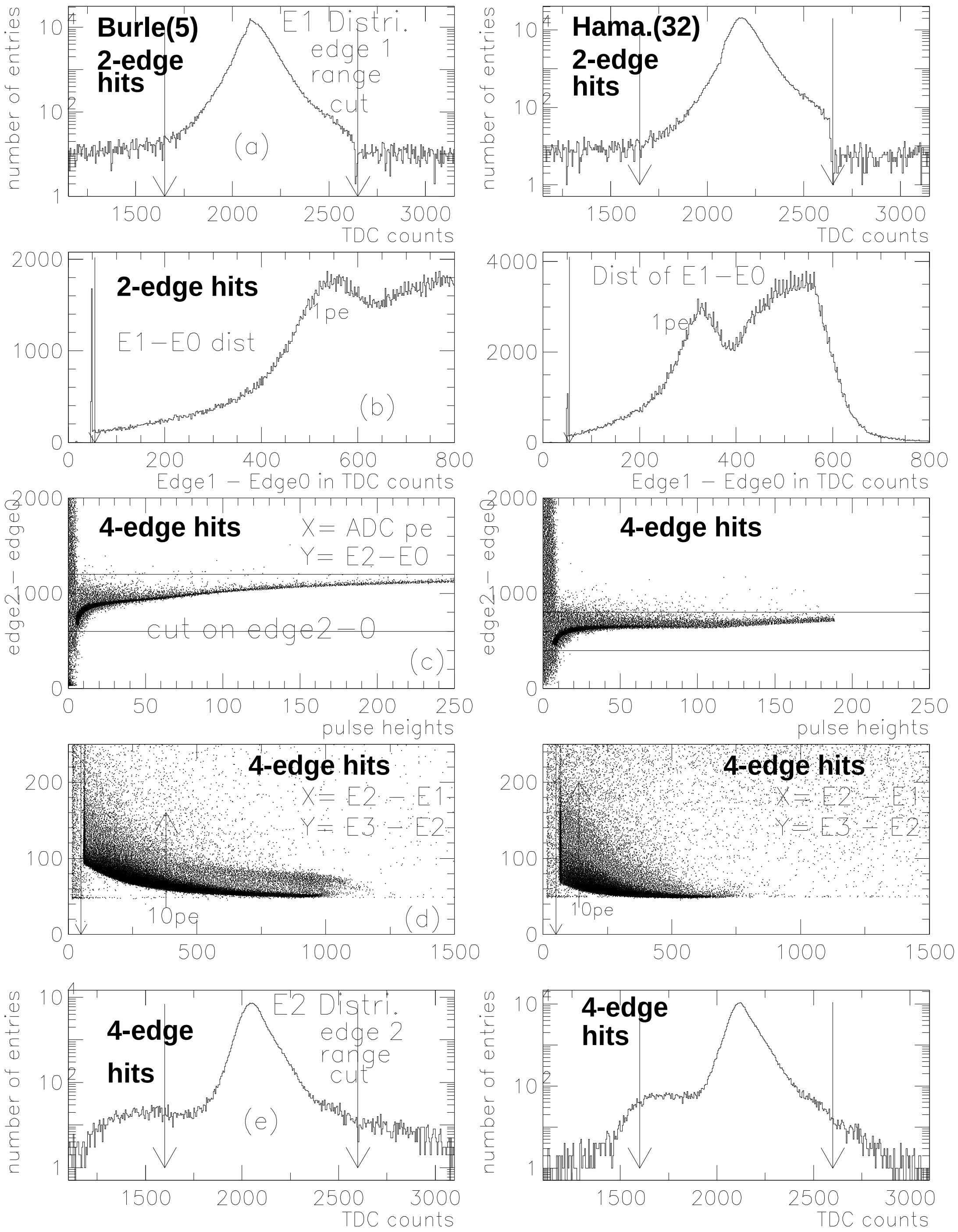

Figure 4.8: Explanations for the edge requirement cuts (a),(b),(c),(d),(e) in Figure 4.7. The figures are described in the text.

have been E30 (instead of E20), were it not for the existence of the prepulsing problem. Fortunately, the normal E32 is very close to a constant of 25 ns, which is intensionally shifted by the electronics. Therefore, E20 = E30 - 25 ns. E30 cannot be too small, because a true 4-edge pulse tells us that it is larger than the largest (saturated) 2-edge pulse, which is already 300 to 600 ns depending on what kind of tube it is originated from. On the other hand, E30 cannot be large enough to exceed the value of high ToT saturation limit. For example, an E30 value of 2,000 does not make any sense because it is equivalent to a pulse height of 10,000,000 PEs!

The scatter plots in Figure 4.8 (d) reveal some important features of 4-edge hits, but these plots are not used aggressively to make the cut. "E21 > 55" is just the minimal high-ToT span requirement and is analogous to cut (b).

When a big signal (many Čerenkov photons) arrives at a PMT, a few of the avalanche photoelectrons, instead of cascading down the series of anodes inside a PMT in order, jump over some anodes in between and arrive at the bottom anode early. This will in turn bring up a small pulse before the main signal. This is the origin of the prepulsing problem, and it is shown in Figure 4.6, as a dotted line. The double band for E2 - E1 $\geq$ 600 in Figure 4.8 (d) on the left is the result of prepulsing in the Burle PMT.

The final cut (e) is similar to the cut (a), but it is for 4-edge hits. The reason for checking E2 Range (Figure 4.7 (e)) instead of E3 is that, edge #3 is again plagued by the prepulsing problem. Normally, when there is no prepulse, E3 - E2 is approximately equal to 25 ns in the case of larger pulses as seen in Figure 4.8 (d).

A 4-edge hit which fails early cuts can still qualify as a valid 2-edge hit. As shown in Figure 4.7, three of the four 4-edge survival categories are identified as valid 2-edge hits (the conceptual drawings to the right and in bold-face lines).

The noise in TDC timing edges can be filtered out by these simple rules, even though there are correlations among them. As seen in Figure 4.7, after these cuts, there are still 96.2% of TDC hits kept, and, more importantly, with their correct time edge assignment identified (those edges in the right most column of Figure 4.7, marked with "time" or "time -25").

Finally, the time of a PMT hit, with 2 edges or 4 edges, is determined by subtracting the timing pedestal (tPed in the previous section) from the time of the edge number just described.

4.4 Timing Error

Section 4.1 explained the origin of the timing uncertainty, and also showed that the error on a PMT's time, or the uncertainty in the PMT's time, can be characterized by the PMT's pulse height. The ADC data keep all the pulse height information for a PMT hit.

4.4.1 ADC Calibration

To look at the ADC information, continuing with the example of Run 780, we can simply enter all ADC counts into 28 histograms channel by channel over the entire run. The results of Channel 16 (a Burle tube) and Channel 33 (a Hamamatsu tube) are displayed in Figure 4.9 . Notice that each histogram has two characteristic bumps. We can determine

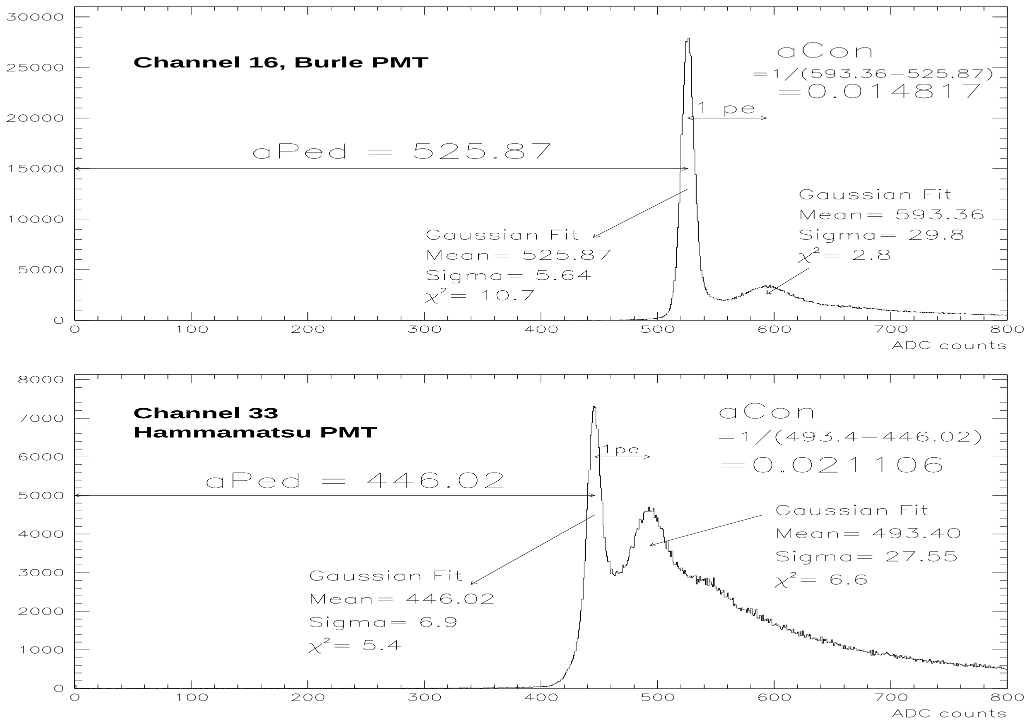

Figure 4.9: ADC pedestal and ADC conversion factor for channel 16 and 33. Data are plotted from Run 780, which has 10^6 triggered events.

where these bumps sit, by fitting them locally with Gaussian forms (even though the peaks look obvious). In Channel 16, we found the first peak sits at 525.9 and the second peak sits at 593.36. The first peak location is named the ADC pedestal, which means that, even with no signal at all, ADC #16 will read a value around 526. It is directly proportional to the length of the ADC gate opened. The second peak position is formed by the most probable pulse height. During an entire run, the chance for PMT #16 to detect just one PE (detectable Čerenkov photon) is substantially larger than the chance to detect 2 PEs, and so on. Thus, we can easily extract the 1 PE strength as, $1\,PE\ = 593.36 - 525.87 = 67.5$ (ADC counts) from the ADC histogram. It is sometimes more convenient to define an ADC conversion factor as $aCon\ = 1/67.5 = 0.0148$ (PE per ADC count). All aCons and aPeds for other channels are calibrated in the same way.

4.4.2 Relation Between ToT and Pulse Height

We have mentioned the Time-over-Threshold method several times already, and it is time to look at it more quantitatively.

As we can see in the ADC calibration results, the pulse height information looks very accurate. However, there are three existing problems to stop us from using the ADC data. First, for early runs before Run 233, there were 8 channels on the front-end analog board that did not have an ADC output. Second, for some unknown reasons during a regular run, the ADC and TDC output could go out of sync abruptly. One event's ADC data matched up with the next event's TDC data, whereas both of them should be written out together in the same event. Once it started to go out of sync, all triggers thereafter were out of phase, too. As a direct evidence for this problem, many channels recorded large ADC pulse heights, whereas the TDC data showed they were not even hit, or vise versa. Last of all, while we shall determine the slewing correction in the next section, the electronic slewing changes too fast (more than exponentially) with PE number; on the contrary, the slewing varies mildly with the ToT parameter. With the ADC, there is not enough resolution at low pulse height. As seen in Figure 4.9, a large portion of PMT hits are actually less than a PE. We can change the unit and use $log(PE)$ instead, but, for example, there are only 7 ADC counts (in Channel 16) to cover the range from 0.2 to 0.3 PE, whereas there are more than 60 TDC counts to cover the same region of 0.2 to 0.3 PE. In terms of statistical accuracy, ToT is a much better energy parameter than the ADC count.[16]

Actually, as mentioned in Chapter 2, Milagro's data acquisition is designed to employ only the ToT method in the first place, and so is Milagrisimo's acquisition system since they use the same front-end electronics. Nevertheless, as shown in Figure 4.10, ADC

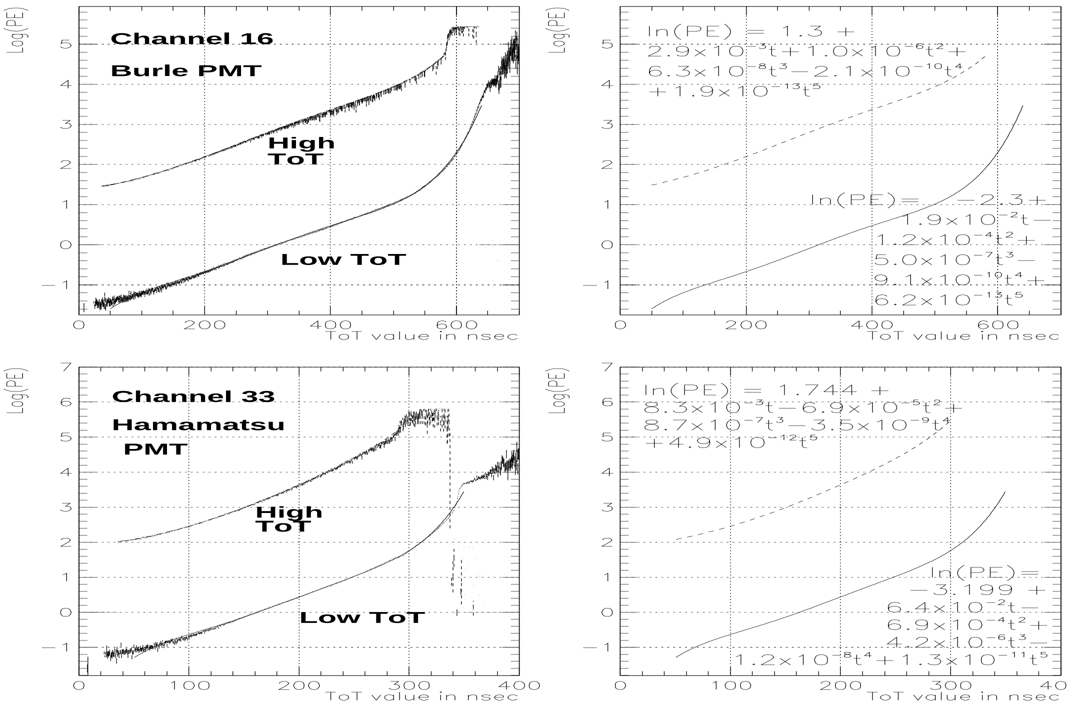

Figure 4.10: ToT versus ADC. The two plots, on the right, are showing the fitted results for the same curves on the left plots.

data is crucial to establish the one-to-one relationship between ToT (ns) and ADC pulse height (PE), before we can confidently use ToT as a legitimate pulse-height substitute.

[16] This is why mentioned in Chapter 2 that ToT has a better dynamic range than ADC.

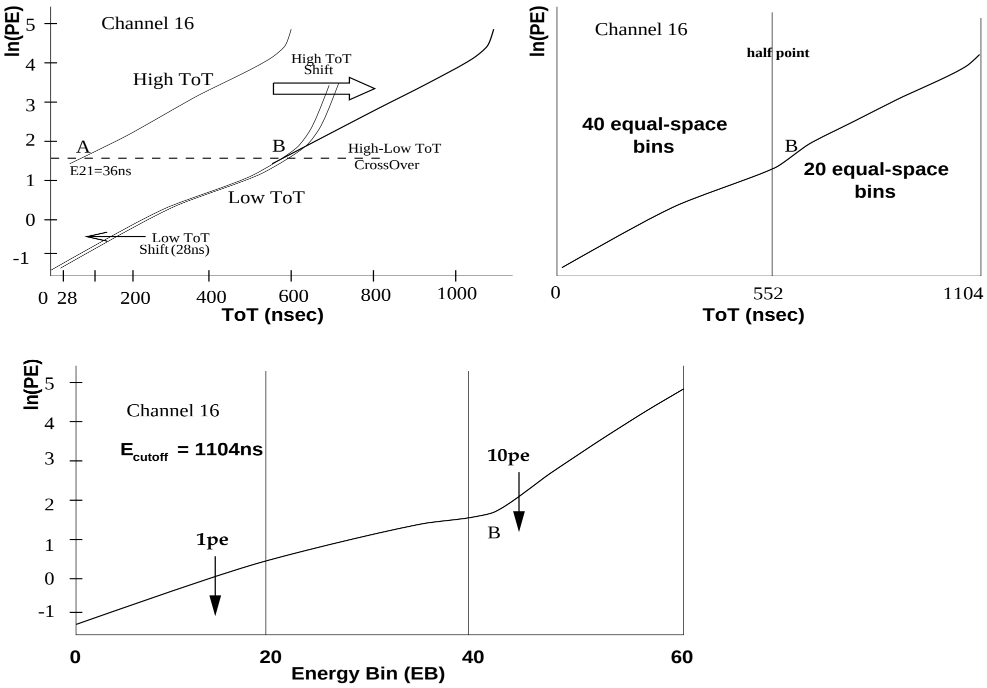

Figure 4.11: Combined and normalized ToT as a final pulse-height equivalent.

4.4.3 Combined ToT as Final Pulse Height Parameter

Even though we have decided to use ToT, the existence of a discontinuity between high ToT and low ToT is an awkward nuisance.[17] Something can be done to improve it. Notice that in Figure 4.10, there is an overlap area during the crossover from low ToT to high ToT. A single continuous ToT parameter can be constructed. Refer to the drawing in Figure 4.11, there are 4 steps to build the generalized ToT parameter: (1) remove the minimal opening of $\sim$ 55 counts from the low ToT, (2) shift the high ToT by adding a constant to overlap with low ToT, (3) apply a saturation limit to the high ToT, and (4) bin the entire region. The bins will be used to characterize the time calibration (both the offset and the resolution) as a function of pulse height for each tube. More explanations follow.

In Figure 4.11 , we want to shift the high-ToT curve horizontally along the ToT axis (from point A to point B). How do we decide where the best point B is? For channel 16, we choose small 4-edge hits, with E21 (high-ToT span) value falling in between 69 and 75 TDC counts, and plot the distribution histogram of the variable $\frac{E30-55}{2}$ (ns). The constant 55, is the asymptotic value of E32 (see Figure 4.8 (d)) for very large pulse heights, $E32_{\circ}$ = 55.[18] Recall that this constant is the hardwired minimal offset between the low and high threshold starts set by the electronics. The constant varies channel by channel; for example, it is 52 for channel 33. I locate the best crossover value by fitting the distribution

[17]As can be seen in Figure 4.10, the transition between the two separate ToT lines happens around $\sim$ 10 PE.

[18]In the scatter plot Figure 4.8 (d), as E21 (on the x-axis) increases, the lower sharp rim of the E32 (the y-axis) distribution approaches a constant value. In the Burle tube case, there is a visible band above the lower rim in the high E21 region, which is caused by the prepulses.

to a Gaussian and using its peak value. For channel 16, the crossover value is found to be $C_r = 512.4$ ns.

Next, we shall bin the entire combined-ToT range. When a pulse height approaches the ToT saturation limit, for example in channel 16, above 1,100 ns (about 400 PEs), there are not enough entries to make as good statistics as those in the low energy range. Also shown in the scatter plot Figure 4.8 (d), there are few entries above 1,100 TDC counts. A cut-off number of $R = 1,104$ (ns) is applied to channel 16. It means that, if a valid TDC value is larger than 1,104, it is taken to be 1,104. Different channels have different cut-offs, as well as different crossovers. The entire range of the combined ToT starts from zero (not 55) and ends at 1,104 for channel 16. We divide it, in the middle, into two halves. The lower half of the ToT range is further divided into 40 equally spaced bins, and the high-end half is divided into 20 equally spaced bins. Overflows above cut-off go to bin 60. The value of 1,104 is chosen, such that bin 59 and bin 60 have roughly equal numbers of entries.

After this procedure is done for every channel, different $E32_\circ$ (TDC count), C_r (ns), and R (ns) values are generated. Whenever there is a hit in any tube, either with 2 edges or 4 edges, it belongs to a new well-defined parameter "energy bin" (EB) for its channel. In the case of a 2-edge hit, its EB is given by

$$t = \frac{E10 - E32_\circ}{2},$$

$$\begin{aligned} if \qquad & t < \frac{R}{2} \ \Rightarrow \ EB = \ int(\frac{t}{R/80}) + 1, \\ if \qquad & t \geq \frac{R}{2} \ \Rightarrow \ EB = \ int(\frac{t}{R/40}) + 1. \end{aligned}$$

In the case of a 4-edge hit, its EB is given by

$$\begin{aligned} if \qquad & E21 < 36 \ ns \ \Rightarrow \ t = \frac{E30 - E32_\circ}{2}, \\ if \qquad & E21 \geq 36 \ ns \ \Rightarrow \ t = \frac{E21}{2} + C_r, \\ if \qquad & t < \frac{R}{2} \ \Rightarrow \ EB = \ int(\frac{t}{R/80}) + 1, \\ if \qquad & t \geq \frac{R}{2} \ \Rightarrow \ EB = \ int(\frac{t}{R/40}) + 1. \end{aligned}$$

We have gone a long way from the ADC to the ToT, then to the energy bin, EB. The timing error of a PMT time is now directly related to its EB number. The larger the EB number, the smaller the uncertainty width of a readout timing is. In fitting a shower direction, the EB values of PMT hits will pass into the fitter to directly determine weights. From now on, the term "ToT" will be used to represent the generalized ToT energy bins, whenever there is no ambiguity.

4.5 Direction Reconstruction

During a fit, the weight of a PMT hit, w_i, is inversely related to its ToT, EB_i, but the actual function form needs to be determined. To find the right weight for a chosen counter in a fit, we have to try to fit the shower first with an estimated weight for the chosen PMT. After the trial fit, the residual between the tube's time, t_i, and the fitted plane (it is called T-Chi in our jargon), can be derived. Of course, we have to assign an estimated weight for every counter, to be able to fit the shower; thus, there are actually 28 T-Chi values generated. The idea is that, after fitting many different showers with the same set of estimated weights, we can accumulate T-Chi distributions with characteristic widths for 28 channels, and, furthermore, 60 energy bins.

4.5.1 Least Squares Plane Fit and T-Chi

Let us fit the shower, now that we have all the information handy (see Figure 2.3 and Figure 4.2 for conceptual pictures). Assume a triggered event has N PMT hits, with N known PMT coordinates, (x_1, y_1, z_1), $(x_2, y_2, z_2), \cdots, (x_N, y_N, z_N)$,[19] and N known PMT times, $t_1, t_2, \cdots, t_N$; a best plane, which is defined by a perpendicular unit vector $\mathbf{p} = l\vec{x} + m\vec{y} + n\vec{z}$, can be found by minimizing the function, χ^2,

$$\chi^2 = \sum_{i=1}^{N} w_i \cdot [l\, x_i + m\, y_i + n\, z_i + c\,(t_i - T_o)]^2,$$

where c is the speed of light, T_o is a freely varied constant, which stands for the arrival time of the entire shower, and w_i is the weight of the i-th PMT hit,

$$w_i = \frac{1}{\sigma_i^2}.$$

In the first trial, σ_i is given by

$$\sigma_i = e^{3.54 - 0.038 \cdot EB_i} + 5, \tag{4.1}$$

where EB_i can be any integer between 1 and 60. This is just an educated guess from other people's experience.

We introduce the extra notation of σ_i because if the resulting T-Chi$_i$ distribution is a Gaussian, the standard deviation of the Gaussian distribution turns out to be σ_i. In real life, as we will see many times, the shape of T-Chi distributions is never Gaussian but has an asymmetrical tail to one side of the main peak. Nevertheless, the Gaussian σ_i is very useful and can be used as an approximation.

Given a dozen points in space, we can always find a best fitted plane to represent them, no matter how badly these points are distributed. Therefore, to assure the quality of shower fitting, we have to apply some reasonable requirements or cuts to the above fitter.

Basically, the scheme is that a shower is refit four times while far-off counters are removed between consecutive fits. When we finish the first pass fit of a shower, if any T-Chi$_i$ is greater than 5 σ_i (Equation 4.1), we throw away that i-th PMT, before proceeding to the

[19] Notice that the true z coordinates (water depths) for tubes are included in the fitter for real data.

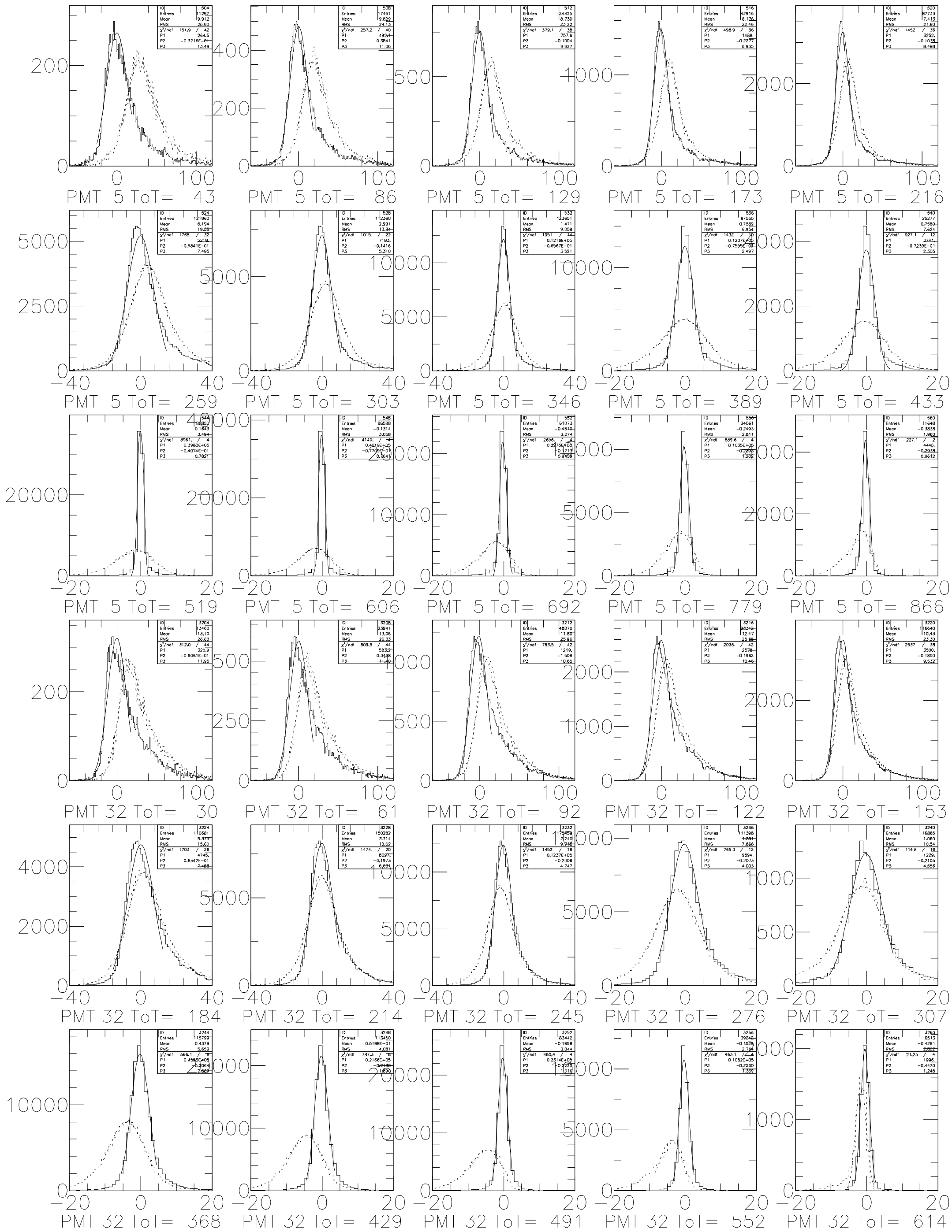

Figure 4.12: T-Chi distributions before (dotted) and after (solid) the slewing correction. The figures are described in the text.

second-pass fit. Similarly, we throw out counters with T-Chi$_i$ $> 3\,\sigma_i$, before we go to the third pass. At last, we throw out counters with T-Chi$_i$ $> 2\,\sigma_i$, before a final fourth pass fit. The requirement is that a successful fit has to have at least 5 counters remaining in the fourth pass fit.

Eight Milagrisimo runs from Run 269 to Run 275 (about 6 million triggered events) are fitted to demonstrate the method. The weights used to do the 4-pass plane fit are shown in Equation 4.1. Therefore, $28\times60=$ 1,680 T-Chi distribution histograms are made after the process. In Figure 4.12 , instead of all 1,680 histograms, only channel 5 (a Burle tube) and channel 32 (a Hamamatsu tube) are selected, and only 15 EBs (energy bin, $1,\ \ 5,\ \ 9,\cdots,57$) for each channel are shown. The upper 3 rows are from channel 5, and the lower 3 rows are from channel 32. The dotted-line histograms are the distributions which result. In the figure, the upper 15 plots reveal energy bin number 1,5,9,13,..,57 from PMT number 5 and the lower 15 ones are from PMT number 32 for the same corresponding energy bins. The ToT numbers on the plot are the generalized ToT values in nanoseconds. In each channel, the fourth plot of the 15 histograms roughly corresponds to 1 PE in ADC pulse height. The better looking solid histograms are obtained after putting in the slewing correction which will be discussed in the next section.

4.5.2 Slewing Correction

In Figure 4.12 , as expected, the widths of T-Chi distributions are decreasing as the energy bin (EB) increases, and the lower energy ones do have late tails toward the right-hand side. It is desirable to be able to view the information of the entire 1,680 histograms in fewer plots. The two most important attributes of the T-Chi distributions are their widths and peak locations. The peak in a T-Chi distribution can be found by simply searching for the maximal value, and the width can be estimated by fitting the distribution, around the peak area, with a Gaussian form. After the fit, the Gaussian in turn gives a better new peak position. The Gaussian peaks were actually used.

As shown in Figure 4.13, all these 1,680 widths (Gaussian sigmas) are plotted against their energy-bin numbers (EB = 0 – 60) in 28 charts. Each plot represents one PMT channel. Again, consider only the dotted line for now. Some spikes happen in lower energy bins, because sometimes the automatic[20] fitting process fails to select a good portion from the non-Gaussian distribution, before applying a Gaussian fit. This is okay, because most spikes go away in the lower solid histograms, which will be explained momentarily. There is also some jitter around EB = 40, which is caused by the roughness of the high-low ToT transition. Most channels have a T-Chi width about 20 ns in the first energy bin, and less than 3 ns in the last energy bin. The peak results are shown in dotted histograms in Figure 4.14. Obviously, most dotted T-Chi distributions are not centered at zero. Peaks at $EB = 1$, are up to 50 ns later than those at $EB = 60$.

Is this the shower curvature discussed in Section 4.1? It is not, because the 6 million randomly positioned shower cores have long smeared out that effect. It is true that, in an air shower, secondaries with less energy fall behind those with more energy, as discussed in Section 4.1 already. However, referring to the middle plot in Figure 4.3, the magnitude of 50 or 40 ns is too large for the typical shower front spread. Much of the additional delay comes from a new effect — electronic slewing. It is caused by two reasons.

[20]It is too tedious to do it by hand.

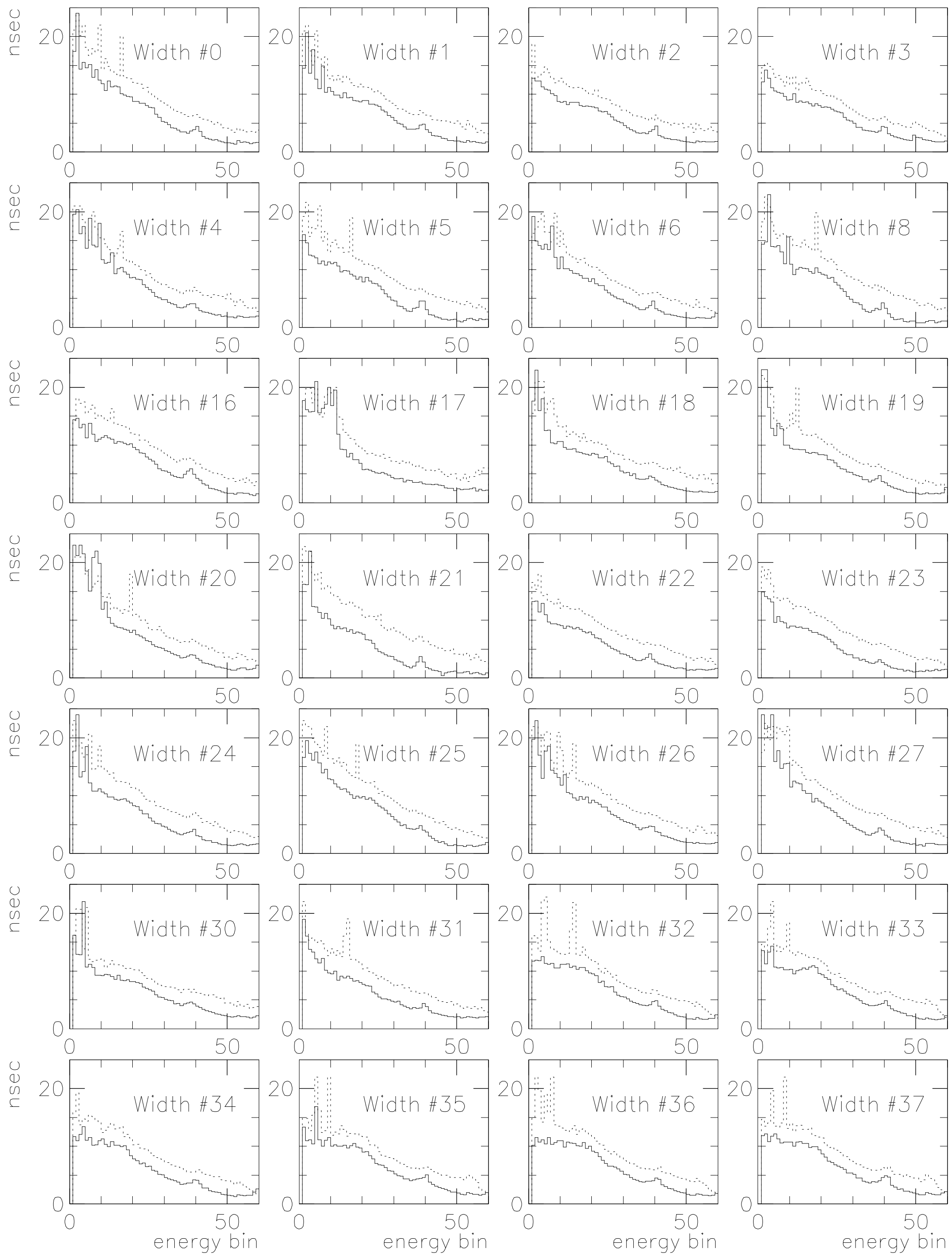

Figure 4.13: Gaussian widths for all 28 PMTs and all 60 energy bins. The dotted histograms are from those before the slewing correction is applied and the solid histograms are after the slewing correction.

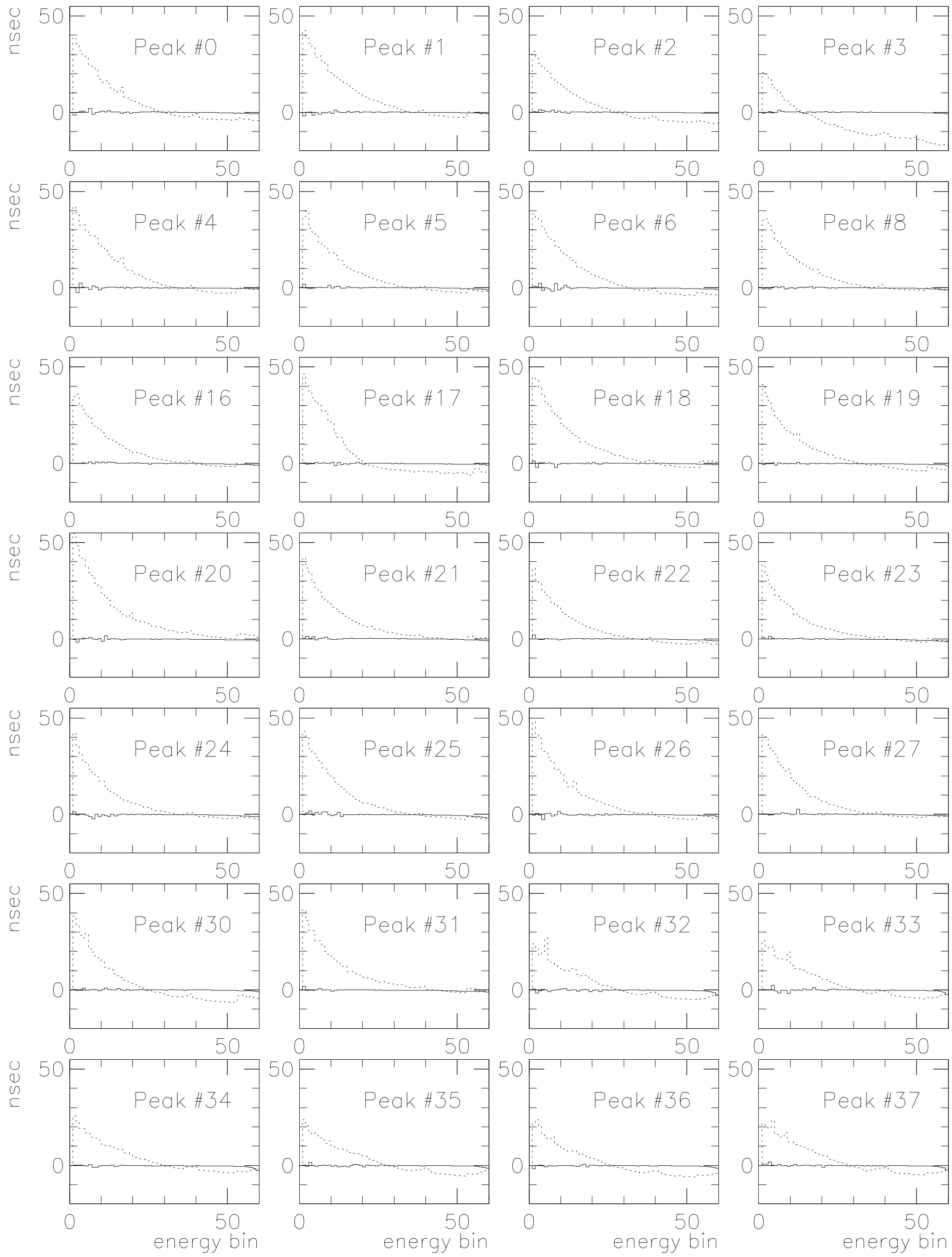

Figure 4.14: Peak positions for T-Chi distributions. Dotted ones are from those before slewing correction, and solid ones — after slewing correction.

First, the pulse arrival time is determined when the leading edge crosses a preset threshold. Large pulses have shorter rise times to reach a fixed threshold than those of smaller pulses (see Figure 4.6). As a result, the "observed" arrival time for a tiny pulse can be severely delayed. Second, there is a sampling effect inside the PMT during the generation and transport of photoelectrons before they convert into electric pulses. Small pulses come out of PMTs later than larger pulses although Čerenkov photons arrive at PMTs at the same time.

Another possible reason for the peak misalignment may come from inaccurate timing pedestal measurements. By looking at the plots, we can tell that PMT #3 likely has a bad timing pedestal calibration due to its very different baseline.

By applying a recursive algorithm, we can correct these slewing and pedestal problems. For each PMT hit, given its channel number and its energy bin number, the peak and the width value from these two plots can be found. Then, simply subtract the T-Chi peak value from the PMT timing of the hit, use the width value as the new weight, and refit the shower to get a new set of T-Chi values. After refitting many showers, we can regenerate these distributions, including new width and peak graphs. The new result should be better.

For example, take a PMT hit in channel 6. After we locate its energy bin, if it belongs to $EB = 1$, correct its PMT time(t) by 38 ns: $t = t - 38$ to make it arrive 38 ns earlier (see the dotted lines in Figure 4.14); if it belongs to $EB = 50$, add 4 ns to t, $t = t + 4$ to make it arrive 4 ns later, and so on. As for the weight, we do not use the old trial value ($e^{3.54-0.038 \cdot EB_6} + 5$) any more, but take the actual width found in the plot (dotted lines in Figure 4.13) for channel 6 as the new weight to do the second-round fit. After the second-round fit, the peak plot of channel 6 should be better, such that the peak value at $EB = 1$ is much less than 38 ns. If the bootstrap method is the right thing to do, the width of the second-round T-Chi distribution for channel 6 should be narrower, too.[21]

The way we obtained T-Chi, however, is biased. To make the process better, we have to exclude the counter under consideration. For example, in order to make the T-Chi histogram for channel 6, we select all showers with PMT 6 fired as usual, but this time we do not let counter 6 participate in the actual fit. The resulting plane is decided by everyone else but PMT 6. Nevertheless, the T-Chi value for channel 6 is still determined as before. In the original biased method, one single fit can generate 12 T-Chi entries or more depending on how many tubes were hit. Now one shower fit can only give one T-Chi entry (i.e., for channel 6). One shower can still give 12 T-Chi entries but it just has to be fitted 12 different times. This "exclusive" algorithm consumes a lot of computing time.

After the second-round fitting finishes, with the unbiased exclusive method, new peak positions and new widths are available. Most peaks are still not centered since the plane readjusts itself constantly. Nonetheless, we can repeat the processes until all peaks are centered at zero. For data between Run 269 and Run 275, the recursive bootstrap converges after 3 or 4 iterations. I iterate few more times to make sure the result is indeed stable.

As we have noticed already, those solid-line histograms in Figure 4.13 and Figure 4.14 are obtained after the recursion. Clearly, all peaks line up at zero, and, more

[21] The peak curves arise smoothly from zero to 30 ns below 1 PE. If we were to use ADC pulse height instead of the EB parameter, it would be difficult to do the slewing correction now. The ADC cannot supply this many data points below 1 PE.

importantly, all widths become narrower.

T-Chi is the time difference between counter and the fitted plane. A perfect shower would be one where every time sits, no higher, no lower, but exactly on the fitted plane. The shower direction, then, would be perfectly accurate. Unfortunately, the shower fluctuations alone ruin the possibility of that perfect line-up, and we cannot alter that. Other than the intrinsic shower fluctuations, there are other processes, such as the electronic slewing or wrong TDC pedestals, which worsen the timing accuracy. We have made a lot of efforts in this chapter to straighten up the second part. The fact that every T-Chi distribution becomes narrower after the recursive process makes us believe we have fixed up the "correctable" part of the shower timing.

This slewing calibration was carried out about every 100 runs. For example, all the data between Run 649 and Run 661 (about 8 million events) were taken to run the slewing correction, and 1,680 slewing-correction constants, after 6 iterations, were written out. These constants are to be used for real shower processing between Run 600 and Run 699. An example of the slewing correction constants is shown in Figure 4.15.

4.6 Pointing Difference Between Two Sub-Arrays

It is plausible that the slewing correction does improve the overall angular resolution, because all the T-Chi distributions get narrower. However, we want to find out, if there are any other parameters to be more directly linked to the angular resolution.

As shown in Figure 4.16, the detector is intentionally divided into two sparse arrays, which are embedded inside each other. We call them the even sub-array and the odd sub-array. Many showers are large enough to trigger both sub-arrays for five or more hit PMTs each. The same shower is fit separately in the two sub-arrays, and these two fitted directions are compared to each other to see how well they agree. The name for the space-angle difference between the two fitted directions is "deleo" (delta of even and odd). Deleo is always quoted in degrees.

Fewer than half of the triggered events can be fitted successfully with both sub-arrays and return the deleo value, because the usual criteria — 4-pass refit and 5 surviving counters — are required for each sub-array's fitting. Nonetheless, a typical 1-million event run will accumulate enough entries to demonstrate the result. Run 269 is processed on the two sub-arrays, for comparison purposes, with and without the slewing correction we describe in the previous section, and the result of deleo is plotted in Figure 4.17. Dotted histograms are deleo distributions without slewing corrections, and solid histograms are deleos with slewing corrections. Results for different shower sizes, in terms of Nhit (number of PMT hits), are shown, too. The difference between the two separate directions are much smaller, when the fitting is processed with the slewing correction, than without one.

A narrower deleo means a better pointing and a better angular resolution. Furthermore, via the definition of angular resolution, we can derive it from the deleo distribution. The lego plot in Figure 4.18 on the left is a 2-D Gaussian distribution with $\sigma_x = 1$ and $\sigma_y = 1$. After we convert x and y into a single variable $r = \sqrt{x^2 + y^2}$, the original 2-D Gaussian is transformed into a 1-D distribution (the plot on the right in the same figure). Notice that the peak position in the 1-D counterpart is the sigma of the original 2-D Gaussian distribution.

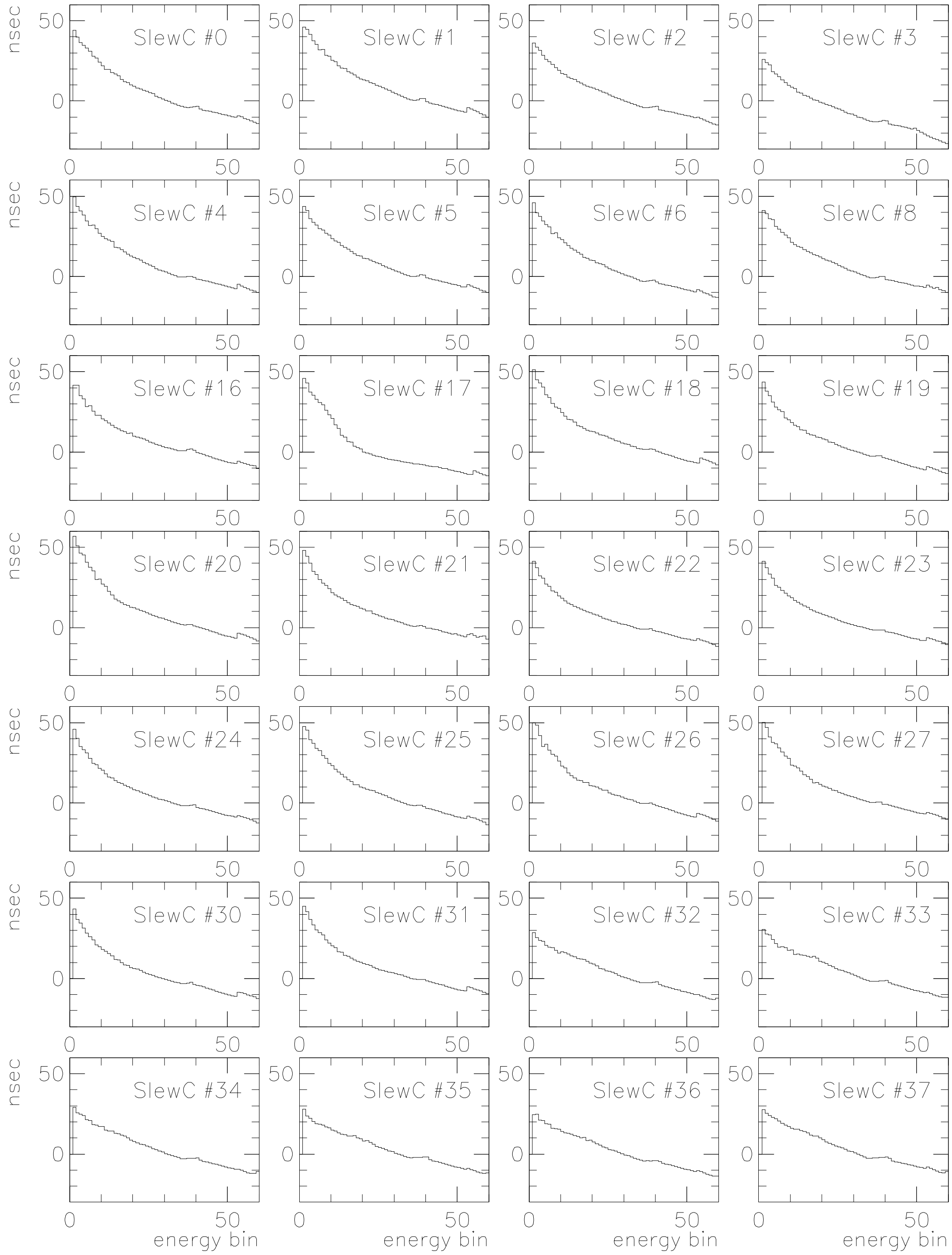

Figure 4.15: Final slewing correction used for data processing of Run 600 to Run 699.

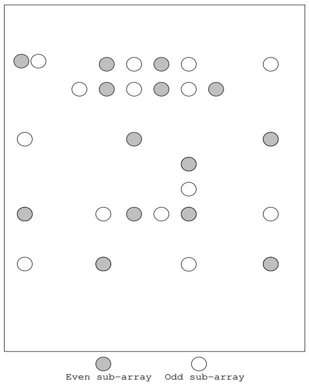

Figure 4.16: Tube assignments for the even and the odd sub-arrays.

If the shape of the 1-dimensional deleo distribution is truly equivalent to that converted from a symmetrical 2-dimensional Gaussian distribution, then, the angular resolution of the entire detector (not a sub-array) is given by

$$angular \quad resolution = \frac{peak \quad in \quad deleo \quad distribution}{\sqrt{2} \cdot \sqrt{2}}$$

The first $\sqrt{2}$ comes from the fact that, the difference between the two directions of sub-arrays is larger than that between the direction of either sub-arrays and the true shower direction. The second $\sqrt{2}$ comes from the fact that, the entire detector has twice as many counters than either sub-array, so gives a better fit than either subarray alone.

As shown in Figure 4.17 the top row on the left (Nhit $\geq$ 12), the solid histogram peaks around 4°. Thus, the Milagrisimo detector, after slewing correction and for all its events, has an angular resolution of about 2°. If we make an event-size cut at Nhit $\geq$ 26, the angular resolution can be as good as 1°.

However, there are two assumptions here, when I state the angular resolution above: (1) the deleo distribution is a 2-dimensional Gaussian, (2) there is no existing systematic pointing error. I shall discuss the effect of the first assumption in next chapter, when I address the angular resolution more rigorously.

Take an example to explain the second concern: suppose the shower fitting is off 10 degrees to the east and 10 degrees to the horizon, systematically. Both sub-arrays will see the same systematic effect, during their fits, and, as a result, the deleo will cancel the 14 degree error and show a narrow distribution.

The rest of this chapter is mainly trying to find out, if there are any systematic errors in the Milagrisimo pointing.

4.7 Effect of the Tilted Pond Bottom

We want to explore one more possible cause for systematic errors, before process the data. As we mentioned several times in Chapter 2 and Chapter 3, the pond bottom is not flat but tilting toward the middle. Even though we do use actual z values in the fitter to compensate for the effect, it may still have some residual effect remaining.

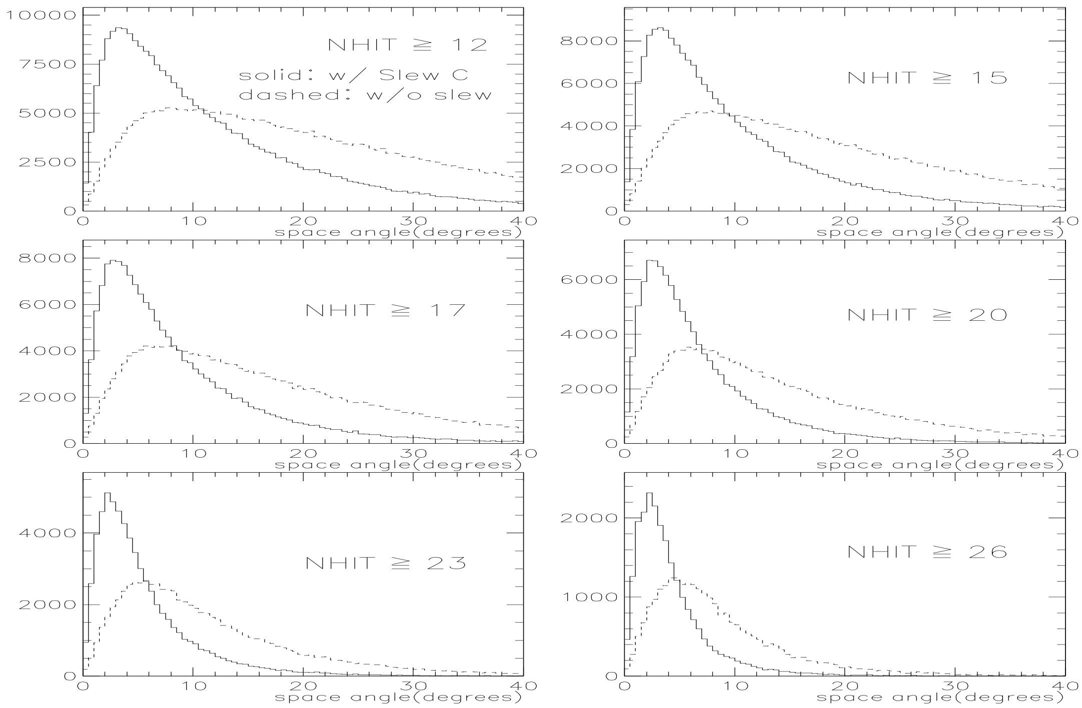

Figure 4.17: Space Angle Difference between two sub-arrays, with and without the slewing correction described in Section 4.5.

As shown in Figure 4.19, instead of even and odd, the detector is divided into north and south sub-arrays. Because there are more tubes sitting on the north slope, the two reconstructed directions, for the vertical shower in the drawing, may sense different systematic errors and may not cleanly cancel each other in the delns (delta of north and south) distribution.

Actually, if the situation is really as shown in Figure 4.19 , the north sub-array sees a systematic of 10° toward South, and the south sub-array sees a systematic of 10° toward North. The "delns" will show a result of 20°, compared to a result of zero in an ideal deleo case. Ironically, the entire detector under this scenario will suffer no systematic at all, [22] while delns shows a big number.

After enough fits are accumulated, the distributions of the three coordinate components of vector $\mathbf{u}_1 - \mathbf{u}_2$ (see Figure 4.19), instead of delns, are examined. These 3 values, thus, can vary from -2.0 to 2.0. If the two sub-arrays cancel the possible systematic cleanly, these three distributions should peak at zero exactly. Again, Run 269 is processed, which has one million triggers, with slewing correction, and according to the division of north and south sub-arrays. Thirty percent of the triggered events are fitted successfully with both the north and the south sub-array returning their directional vectors. The 300,000 or so x, y, z components of $\mathbf{u}_1 - \mathbf{u}_2$ are plotted in Figure 4.20, with the statistics shown.

[22] Actually, it cannot be cleanly canceled since there are more tubes in the north sub-array than in the south sub-array.

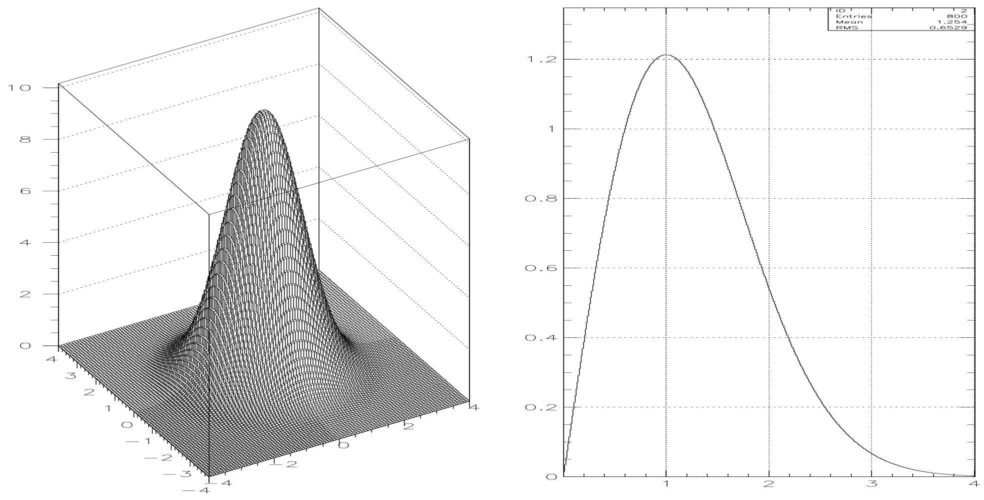

Figure 4.18: A 2-D Gaussian Distribution and its 1-D counterpart.

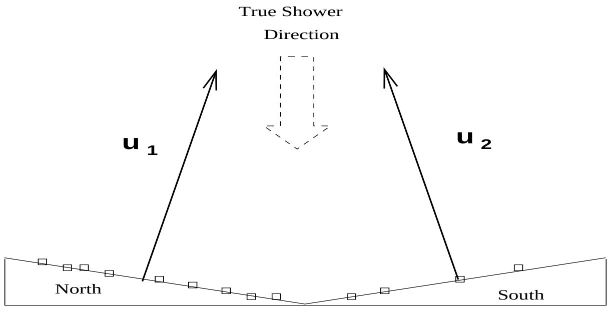

Figure 4.19: North-South Sub-arrays

The mean value of the upper x plot is 0.00934, or an equivalent of 0.54° in terms of space angle, and the mean value of y plot is 0.016, or equivalent to 0.92° in angle. The non-zero value of x shows the net depth difference is not symmetrical along the y-axis (see Figure 2.3). The only conclusion we can draw here is that the uneven water depth over tubes can have some extra effects on the reconstruction, even though we correct the depth difference in the fitter. However, from the deviation above, $\sqrt{0.54^2 + 0.92^2} = 1.07°$, the systematic error for the whole detector can be estimated to be less than 0.5°.

We shall look at this problem again at the end of this chapter, when we discuss the vertical spot and the directional preference.

4.8 Data Processing

To process the raw data, we have to finish all slewing correction calibrations. As shown in Table 4.2, there are altogether 10 calibration jobs done, spread across the entire experimental data set.

Table 4.3 shows the detailed data status, run by run. There are 942 runs, eventu-

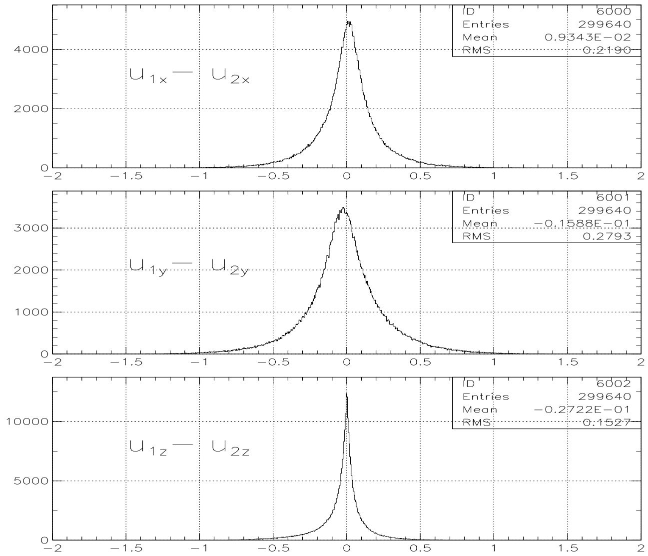

Figure 4.20: x,y,z components of the vector difference from two fitted directions, by the north and the south sub-array.

Calibration Runs	143-149	269-275	331-338	432-442	560-570	649-661	746-761	848-858	961-971	1010-1019
Data Processing	107-232	233-299	300-399	400-499	500-599	600-699	700-799	800-899	900-999	1000-1073

Table 4.2: Numbers within upper row are runs used for generating calibration data, slewing correction and widths. Lower row is the applicable run range using the corresponding calibration data.

ally available for data processing. Out of these 942 runs (the size varies from a single event to one million events, with an exception that, run 111 has 1.4 million events), there are a total of 527.8 million air showers recorded. The data processing successfully reconstructed 472.3 million events or 89.5 percent of the raw events were preserved.

Inputs needed for data processing are: raw data, PMT coordinates, Hi-Lo ToT crossovers, ToT cutoffs, slewing corrections, and T-Chi widths.

There are three levels in the output from the data processing: event-by-event level, run-by-run level, and the entire-experiment level. At the event-by-event level, the output for each triggered event is: fit flag (IERR), which tells if the shower is reconstructible, (θ, ϕ) of the shower direction (if reconstructible), trigger time in Julian day (JD) and Julian second (JS), which is accurate to a microsecond, the number of valid hits (Nhit), the number of PMTs used in the final round of the 4-pass refit (Nfit), total PE numbers from all hits (PEsum, converted from ToT), and the chi-square per degree of freedom of the fit (χ^2),

description	run numbers	sub-total
valid data w/ clock time	104 - 1073	970
missing runs; not on tape	113,116,117,118,135,136,137,244,259,955,956,981	12
bad tapes; non-readable	104,105,106,298,299,300,301,302,303,304,305	11
null runs; zero event	512,853,983	3
bad runs; non-recons.	1056,1057	2
total analyzable runs		942

Table 4.3: Data status by run numbers.

which is a modified version of the χ^2 formula earlier in this chapter,

$$\chi^2 = \frac{Nfit \cdot \sum_{i=1}^{N} w_i[c(t_i - T_o) + l \cdot x_i + m \cdot y_i + n \cdot z_i]^2}{(Nfit - 3) \cdot \sum_{i=1}^{N} w_i}.$$

These results are written compactly into a disk file (e.g., cmp269.dat) for later analysis use and they will be discussed momentarily in the next section.

At the run-by-run level, there is a histogram file, associated with the entire run (e.g., job269.paw). This file includes: the 1,680 T-Chi distributions, and deleo distributions (one try for every 10 raw events read)[23]. These are the same T-Chi and the deleo distributions as previously discussed.

Finally, in order to view the entire period of experiment at a glance, some charts, as shown in Figure 4.21, were made to monitor the stability of the data processing over the entire data set. Run size is the number of events in a run. The ratio of reconstructible events is very stable around 90%. The quality of the fitting is best described by the χ^2 distribution and deleo distribution. The mean value and rms (root-mean-squared)[24] of these two distributions for each run is plotted.

Clearly, the quality of reconstruction is consistent from Run 107 to Run 1073.

4.9 Distributions of Event Attributes

After the data processing, we can examine the distributions of some event properties such as θ, ϕ, χ^2, Nhit. We have the same set of event properties from Monte Carlo simulations in Chapter 3, too, although there are not as many entries compared to the real data. Some attributes of reconstructed data from Run 254 are plotted in Figure 4.22 , together with some Monte Carlo plots in dashed lines. The relevant Monte Carlo entries have been normalized accordingly to be able to compare head-to-head with the real data. In terms of individual plots, they are: (a) the distribution of trigger multiplicity during Run 254; triggers with Nhit < 12 can happen when some of the PMT timing edges cannot be accepted by our edge selecting procedure; on the other hand, the Monte Carlo results sharply peak at $Nhit = 12$, (b) 57% of the reconstructible real events have deleo information and they are plotted together with the results from Monte Carlo proton triggers; despite the

[23]The process calculates deleo; if the deleo fitting is successful, the value is included in the histogram

[24]Instead of distribution the peak and the Gaussian width, we use the mean and the rms, which are easier for histogram software to prepare. This does not matter as far as quality monitoring is concerned.

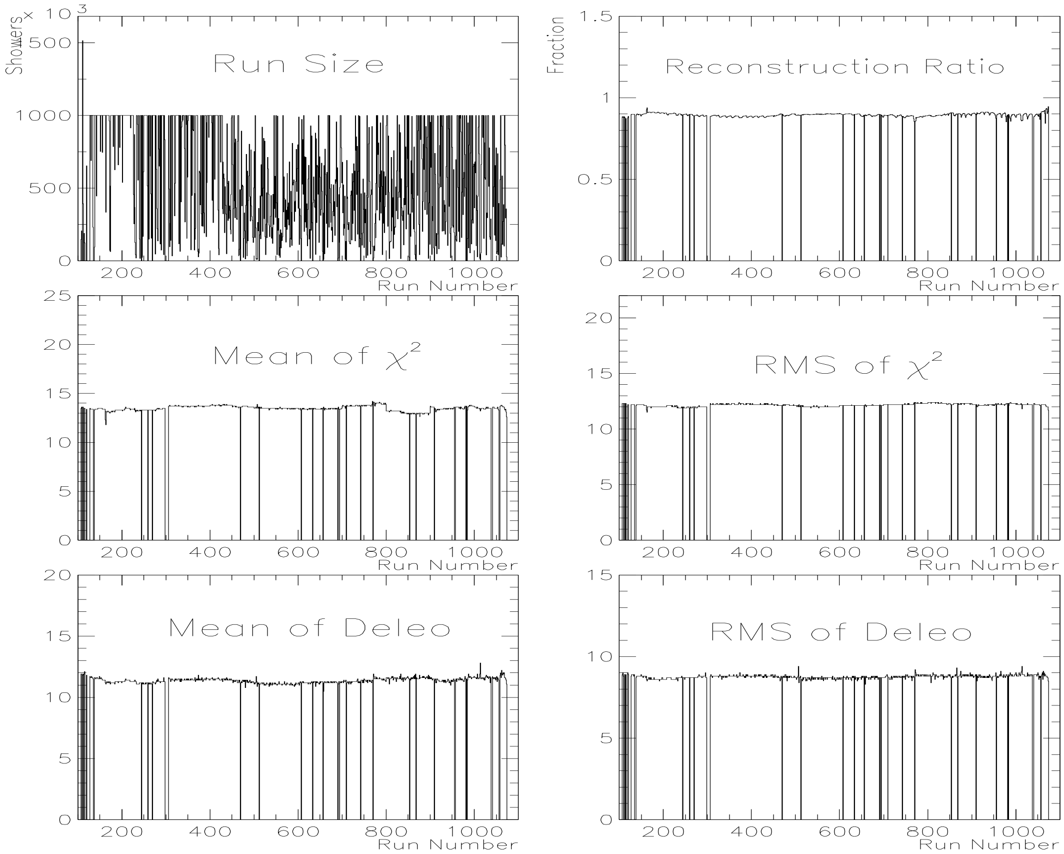

Figure 4.21: Quality monitoring of data processing. X-axis is Run Number in all six plots. There are 261 runs with one million event run size.

rather poor statistics for Monta Carlo events, they agree with each other well, (c) χ^2 of the fitting, (d) ϕ distribution together with Monte Carlo proton triggers; it peaks at around 260°, (e) θ distribution, 96% of entries happen when $\theta < 60°$, and the median value is 28°, (f) trigger density (number of triggers per unit solid angle) in terms of incident angle; at the median angle, 28°, the density is only 51% of that at the vertical spot. These plots are very important to the rest of the study.

4.10 Pointing Preference

The non-uniform ϕ distribution in Figure 4.22 (d) strongly indicates a systematic effect in Milagrisimo's pointing. It is necessary to take a closer look at it.

4.10.1 Vertical Spot

Referring to Figure 4.22 (f), the vertical spot in the sky, $\theta = 0$, under any considerations, should have the highest event density. In a sense, it is like a source. By checking

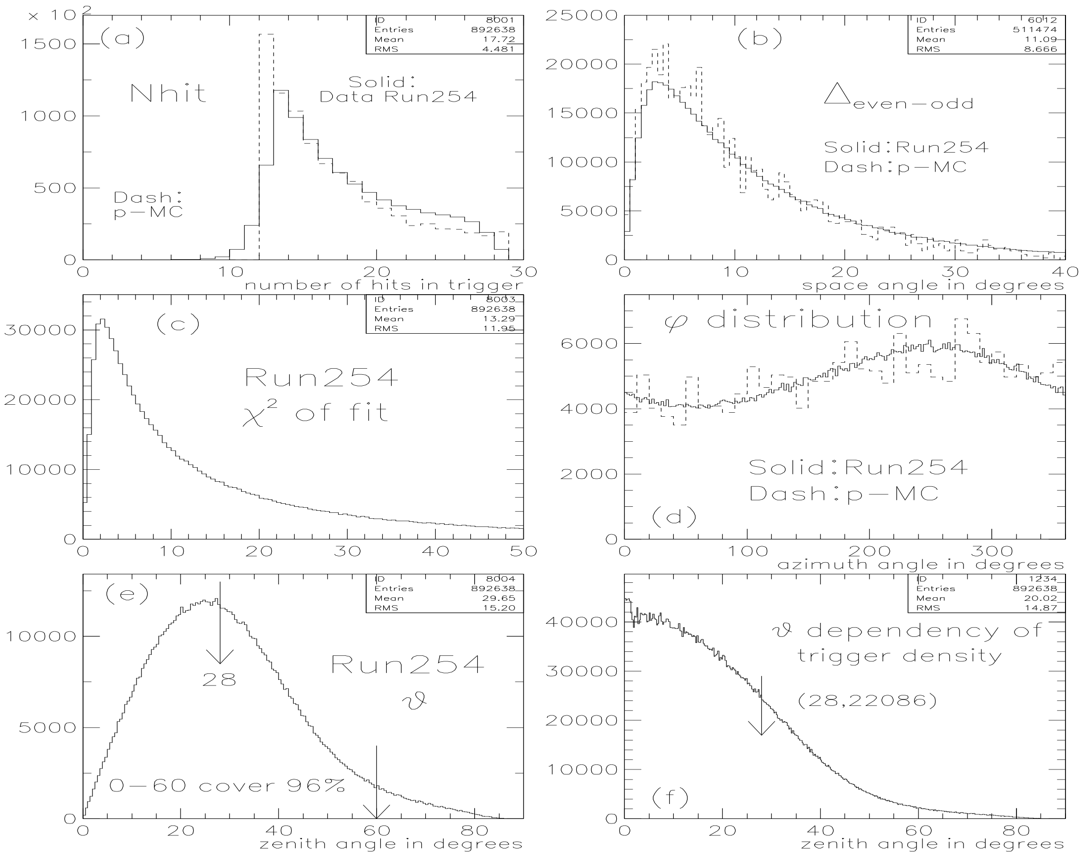

Figure 4.22: Some characteristic properties of a typical run after event reconstruction. Dashed lines are from Monte Carlo simulations. The figures are described in the text.

how far away the actual maximal density spot of the real data sits, relative to $\theta = 0$, the overall systematic error in pointing can be determined.

As a result in Figure 4.23, the 2-dimensional contour plot consists of (θ, ϕ) entries for all reconstructed events from Run 306 to Run 399.[25] These entries of θ and ϕ are plotted in a modified spherical coordinates, such that $(x, y) = (\theta \cos\phi, \theta \sin\phi)$ and the center coordinate origin is the point of $(\theta, \phi) = (0, 0)$. Both θ, and ϕ are in degrees. As seen in the figure, the maximum of the contour plot, accumulated from a lot of data, does not occur at (0,0), but in fact the center of mass is located at $(x, y) = (-1.69, -3.227)$ or $(\theta, \phi) = (3.64°, 242.4°)$. There is a net shift of 3.6° away from the origin.

4.10.2 Water Depth Difference

There are two possible mechanisms to cause this shift. The first scenario is that, for example, the air shower is actually from the direction of $(0, 0)$, it triggers the detector, and after shower reconstruction, the primary appears to be from (3.6°, 242°). The shift is

[25] It takes 50 million entries before the statistics are good enough to make visible the maximal spot.

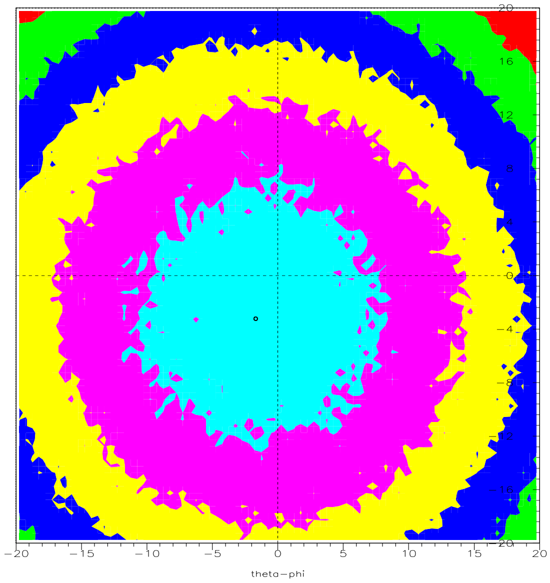

Figure 4.23: Overhead-look of the trigger density. The maximal density occurs at $(\theta, \phi) = (3.64°, 242.4°)$, instead of (0,0).

created during the processes of data reconstruction.

The second scenario is that the shower comes from the direction of $(0, 0)$, but it has a difficult time to trigger the detector. Thus, the detector has a biased choice in selecting incoming showers. After many triggers, the center of mass of these triggered events occurs at (3.6°, 242°). Under this circumstance, if a shower comes from $(0, 0)$ and it triggers the detector, the shower direction after data reconstruction is still at (0,0). This pointing preference happens in the CYGNUS experiment, where counters sit at different elevations (z), and the entire array tilts towards a particular ϕ direction. As a result, there are more showers triggered from that particular direction. However, the direction of shower pointing is not altered.[26]

As will be described in Appendix A, the trigger threshold of Milagrisimo is too low to be able to see the moon shadow for the purpose of pointing calibration. We have to go back to the Monte Carlo simulation to seek for answers.

In Section 3.7.2, we assumed that all PMTs sit at a horizontal plane, when we implemented the first-version detector simulation using a constant water depth of 110 cm for all tubes. In reality, the depth of water above the PMT surface varies from tube to tube as shown in Figure 4.24. The largest depth difference among tubes is 50 cm!

To modify the detector simulation, we use a water thickness of 130 cm for the deepest tube (the one near the middle and marked “0.0” in Figure 4.24), and in turn assign different depth values according to the z configuration as in Figure 4.24. After the assignment, there is, for example, only 81.4 cm of water above the surface of PMT 32 and PMT 33. As mentioned in Section 3.7.2, the same set of the 20 million showers are fed into

[26]The moon shadow, observed in the CYGNUS data, stays where moon is. That clears any speculation of a systematic pointing error in the CYGNUS data reconstruction.

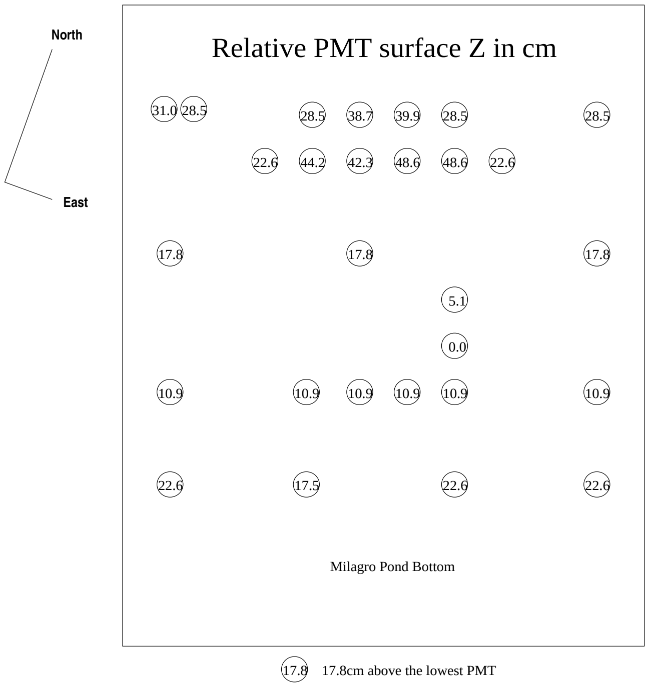

Figure 4.24: Height of each PMT above the deepest Milagrisimo PMT.

the modified detector simulation to get a new set of triggers.

Because the three thousand or so proton Monte Carlo triggers cannot generate enough statistics to make the same density plot as that in Figure 4.23, their center of mass, $(x, y) = (\theta\cos\phi, \theta\sin\phi) =$ (-1.02, -3.45), has large error and cannot be decisive. Nevertheless, it shows the same trend as the position of the maximum in the real data. Fortunately, the ϕ distribution is very sensitive to the broken symmetry. As shown in Figure 4.25 , the left plot is the ϕ distribution from proton Monte Carlo triggers using the constant water slab, and the plot at the right (solid histogram) is the ϕ distribution from proton Monte Carlo events using the real PMT depths. The dashed histogram is the ϕ distribution after reconstructing. The bump around 260° is obvious, and most of all the ratio of the bump (valley) area to the total number of entries is close to that in the real data. The new fitted ϕ distribution is also plotted together with the real data in Figure 4.22 (d).

The water depth as described in Section 2.2 was not constant throughout the experiment. We filled the pond with water on and off until about Run 400. After that, the water depth was kept constant, before we started to drain the pond at Run 773.

The center of mass (maximal spot) for every run is calculated, and their x and y values are plotted versus their run number in Figure 4.26 (first two plots). The third one to the right combines the x and y plots into a 2-dimensional scatter plot. It clearly shows a direction toward the origin (0,0) at the right-top corner. It means that if the water depth is infinity, these maximal spots will merge at the origin.

These two results strongly support that the observed $(\theta, \phi) = (3.64°, 242.4°)$ is not a pointing systematic in our shower reconstruction, but just a directional preference of the

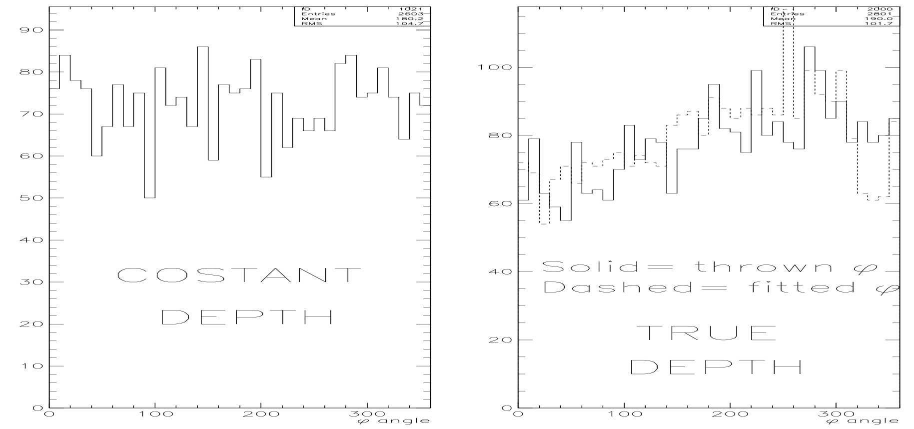

Figure 4.25: The ϕ angle distribution before and after the simulation deployment of water depth correction.

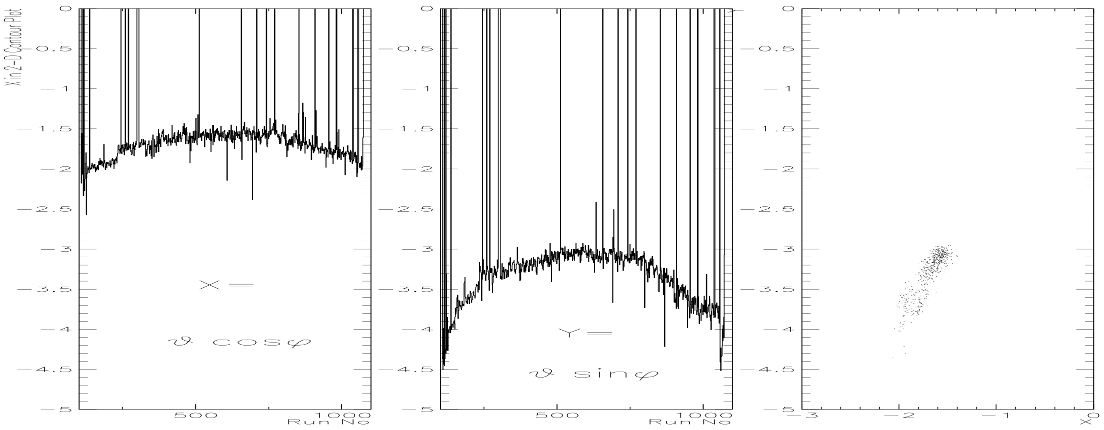

Figure 4.26: The maximal density spot is changing with water depth.

detector caused by the depth difference among counters.

To conclude this chapter, 472 out of the 528 million recorded air showers were successfully reconstructed for their primary directions. The overall angular resolution for these 472 million reconstructed events is about two degrees. In addition, any possible systematic errors in the pointing are believed to be less than 0.5°.

Chapter 5

Data Analysis

BATSE's overwhelming success in the field of gamma-ray bursts, as described in Chapter 1, leaves no room to argue if its detection of gamma-ray bursts (GRBs) is unambiguous. Therefore, instead of independently searching for gamma-ray bursts throughout the Milagrisimo data set, we perform a coincidence search with BATSE's results.

The paragraph on page 15 briefly mentioned the idea of how to search for sources over a homogeneous background. After we generated the Monte Carlo events in Chapter 3 and reconstructed Milagrisimo's air showers in Chapter 4, all the prerequisite tasks have been completed to proceed to do such a search. The first two sections in this chapter will use the Monte Carlo data sets to deduce the effective areas, the average triggered energy, the signal-to-background sensitivity and the best search bin size. Subsequently, all the relevant BATSE GRBs are listed in Section 5.3. Then, a search method will be proposed and verified via rigorous probability and statistics procedures. Once the method is verified by checking the expected background distribution, the real data will be examined using the proposed method. The results will be presented afterward. In addition, in case there is no significant signal found, a scheme is developed to set a quantitative upper limit to constrain these GRBs.

In terms of the signal-above-background method, a GRB is no different than a steady γ -ray source, except for its short time interval. Every time BATSE detects a GRB at a known location in the sky, at a certain time with a certain duration, and if this GRB occurs in Milagrisimo's field of view, we can place a circular space bin around it. Then practically we just count how many events are from within that circular bin, during the known time interval, and compare the number obtained to what should be expected from the background. For poorly localized bursts, some more complicated procedures are introduced. Basically, we shall spend most of this chapter just to fill in the details to describe these steps.

5.1 Effective Area and Median Energy

Since the energy spectra of cosmic-ray background and gamma-ray bursts can be measured by other independent experiments (e.g. Equation 3.6, and Equation 1.1), all we need now before we are able to derive the number of expected cosmic-ray background events, N_b, and the expected number of signal events, N_s, from a GRB, is the effective areas for

type	No of EAS	energy in TeV	E dist.	θ	N_t	core area in m^2	No trig	after cosine	eff. A in m^2
γ	300	50.0	fixed	0-60°	50	1.0×10^6	239	221.3	14754.1
P	500	20.0	fixed	0-60°	50	3.6×10^5	475	413.1	5948.6
γ	500	20.0	fixed	0-60°	50	3.6×10^5	684	581.3	8370.7
P	1000	12.0	fixed	0-60°	50	3.6×10^5	713	630.0	4536.1
γ	1000	12.0	fixed	0-60°	50	3.6×10^5	722	624.8	4498.2
P	2×10^5	0.1-8	$E^{-2.6}$	0-60°	50	3.24×10^4	2857	2581.7	8.36
γ	2×10^5	0.1-8	$E^{-2.6}$	0-60°	50	3.24×10^4	1791	1688.7	5.47
P	4×10^5	0.1-8	$E^{-2.6}$	0-60°	50	3.24×10^4	5444	4988.6	8.08
γ	4×10^5	0.1-8	$E^{-2.6}$	0-60°	50	3.24×10^4	3646	3405.0	5.52
P	2×10^5	.085-.1	$E^{-2.6}$	0-60°	50	3.24×10^4	21	19.7	0.0638
γ	2×10^5	.085-.1	$E^{-2.6}$	0-60°	50	3.24×10^4	48	46.08	0.149
P	2×10^5	.06-.085	$E^{-2.6}$	0-60°	50	3.24×10^4	1	0.95	0.0031
γ	2×10^5	.06-.085	$E^{-2.6}$	0-60°	50	3.24×10^4	19	18.24	0.0591
P	2×10^5	.04-.06	$E^{-2.6}$	0-60°	50	3.24×10^4	0	0.0	-
γ	2×10^5	.04-.06	$E^{-2.6}$	0-60°	50	3.24×10^4	3	2.97	0.0096

Table 5.1: A summary of Monte Carlo data sets. In terms of the incident angle θ, air showers are generated homogeneously according to the covered solid angle. N_t is the number of core positions thrown for each shower, which means that each EAS is reused 50 times. Right before the detector simulation, each EAS is randomly assigned a ϕ angle (0-360°) and a core location over an square area of ±90 meters ($180m \times 180m = 3.24 \times 10^4\ m^2$) or, for higher energy cases, ±300 meters ($600m \times 600m = 3.6 \times 10^5\ m^2$) and ±500 meter ($1000m \times 1000m = 1.0 \times 10^6\ m^2$) in x and y, where (0,0) is the center of the detector. Other than the randomized ϕ and core, the rest of attributes of an air shower during the 50 throws are all identical, including the common incident angle θ. Each trigger entry is subsequently adjusted by a factor of its $\cos\theta$ to accommodate the "cosine effect" discussed in Section 3.8.1. These showers are all processed by the refined version of detector simulation with various PMT depths.

both proton and γ showers over the entire interesting energy range. Monte Carlo data are needed to derive the effective areas. Once N_b and N_s are obtained, the optimal bin size and the signal sensitivity follow immediately.

In addition to the simulation of 0.1-8 TeV air showers and detector response described in Chapter 3, many more Monte Carlo events are generated to improve the statistics and to probe the detector response at energies lower than 0.1 TeV and higher than 8 TeV. A complete list of the Monte Carlo data sets is summarized in table 5.1. In the preparation of these simulations, the same power-law spectrum with an index of -2.6 for γ showers is used to enable a head-to-head comparison with those of protons. The effective areas (in m^2) are also plotted and parameterized in Figure 5.1 in both linear and log scales against their primary energies (in TeV). Notice that the entries between 0.1 and 8 TeV are further differentiated according to their primary energies as if they are independently generated with fixed energies.

As can be seen from the plots, as the energy drops below 100 GeV, the proton

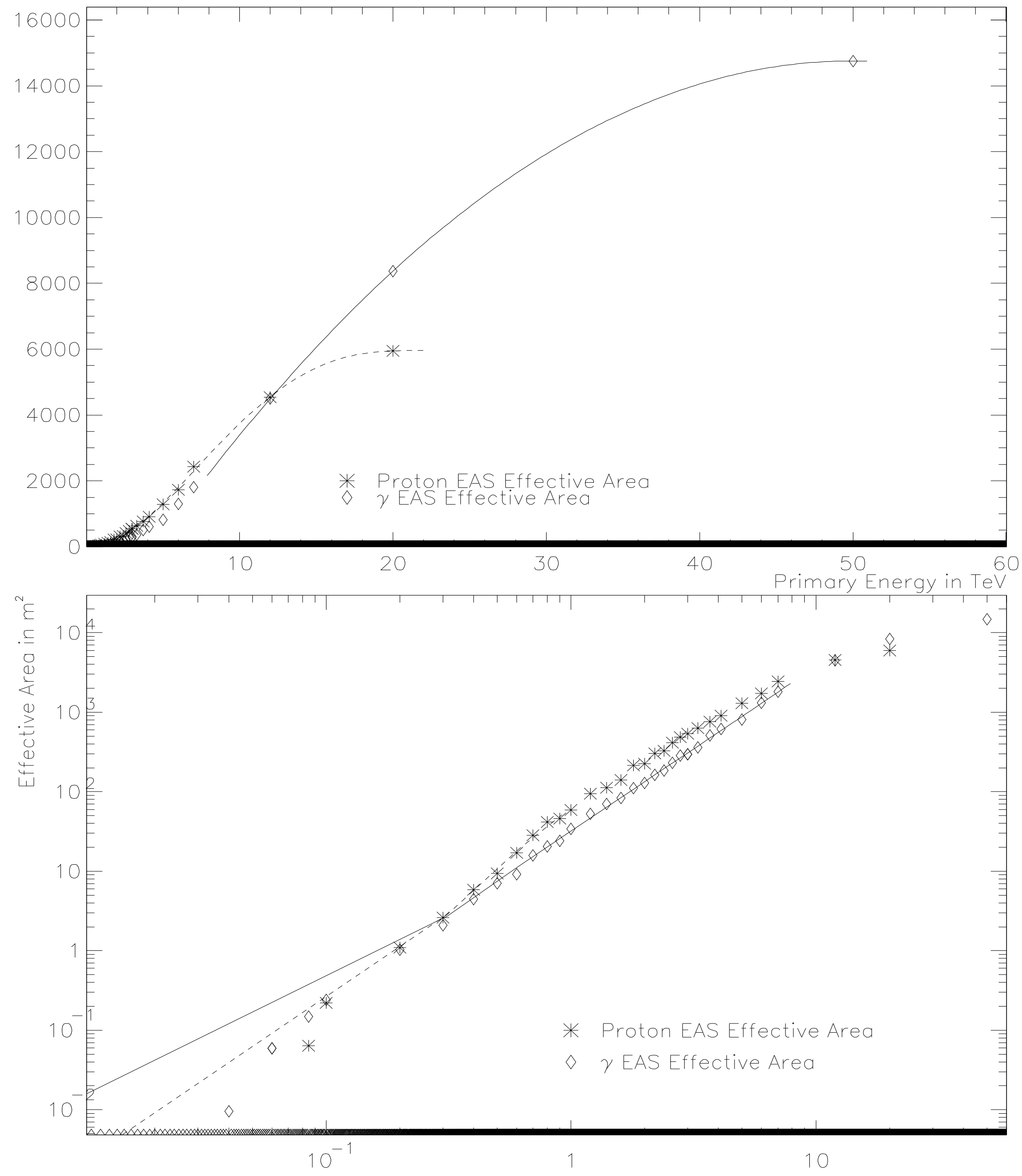

Figure 5.1: The differential effective areas (in m^2) of proton and γ showers as a function of their primary energies (in TeV) in both linear and log scales. In the proton case, entries are fitted with fourth order polynomials in two segments separated at 0.8 TeV. In the γ case, points are fitted with third order polynomials for the region of 0 - 8 TeV, and with second order polynomials for 8 - 50 TeV. Notice that the effective areas shown are averaged over all zenith angles.

EAS effective area diminishes faster than that of a γ EAS. For energies between 100 GeV and 8 TeV, proton effective areas are noticeably higher than those of γ showers and there is a clear cross-over which occurs around 12 TeV. The rationale for this cross-over is that when the energy is low, the more spread out nature of proton showers offsets their smaller shower size (fewer electromagnetic secondaries), but when energy is higher than 12 TeV, the shower size factor passes the shower spread factor and makes γ showers win over proton showers in the effective area.

Because the atmosphere has finite thickness, the effective areas in both cases cannot rise indefinitely with the primary energy. They will eventually reach constant values.

The simulation clearly shows the slowdown for proton events before 20 TeV, and for γ events, before 50 TeV. Other than these qualitative observations, the underlying theoretical distribution is not known and the attempt to fit the points with some simple functions fails. As a last resort, points on the plots are parametrized (or smoothed) with polynomials, and fitted in two segments separated at 0.8 TeV (proton) and 8 TeV (γ).

The Tibet cosmic ray spectrum (Equation 3.6) after some unit rearrangement is given by,

$$\frac{dN}{dE} = 0.212 \;\; E^{-2.6} \; m^{-2} s^{-1} sr^{-1} TeV^{-1}. \tag{5.1}$$

Within a time interval of one second and a sky coverage from zenith to 60 degrees, the equation is further reduced to:

$$\frac{dN}{dE} = 0.666 \;\; E^{-2.6} \; m^{-2} TeV^{-1}. \tag{5.2}$$

Now we can multiply the above cosmic flux by the proton differential effective area just derived to get the proton trigger rate for the detector. After we carry out the integration from 0.04 TeV (40 GeV) to 20 TeV using the two-piece parameterization, the resulting number is,

$$N_p = \int_{0.04}^{20.} A_{peff}(E) \; \frac{dN}{dE} \; dE = 205.7 \; s^{-1}. \tag{5.3}$$

This number 205.7 is larger than the earlier calculated number, 139, at the end of Chapter 3 because there are extra contributions from outside of the 0.1-8 TeV range. The finite integration is a product between a steeply rising function of the effective area and a fast falling function of the cosmic-ray flux. As a result, the outcome is very sensitive to small variations in either the effective area or the cosmic-ray (proton) flux. This product can be shown differentially over the same energy range. The result is plotted in linear and log-log scale in Figure 5.2 (a) and 5.2 (b), respectively. The noticeable sharp bumps in the otherwise smooth curves are caused by the discontinuity between the two piecewise parameterizations at 0.8 TeV. The trigger contribution from above 20 TeV (for protons) has not been determined.[1] However, according to the plots, the trigger contribution from cosmic rays above 20 TeV is rather limited, and the cut seems to be appropriate.

Section 3.8.2 discusses the assumption that all cosmic-ray background particles are protons, which makes the trigger rate larger than that in the experiment. If the simulations

[1] Simulation above 10 TeV becomes difficult because it takes a longer time to transport particles in air and Čerenkov light in water; it takes more storage space to hold the result; and more showers need to be thrown to sample a much larger area.

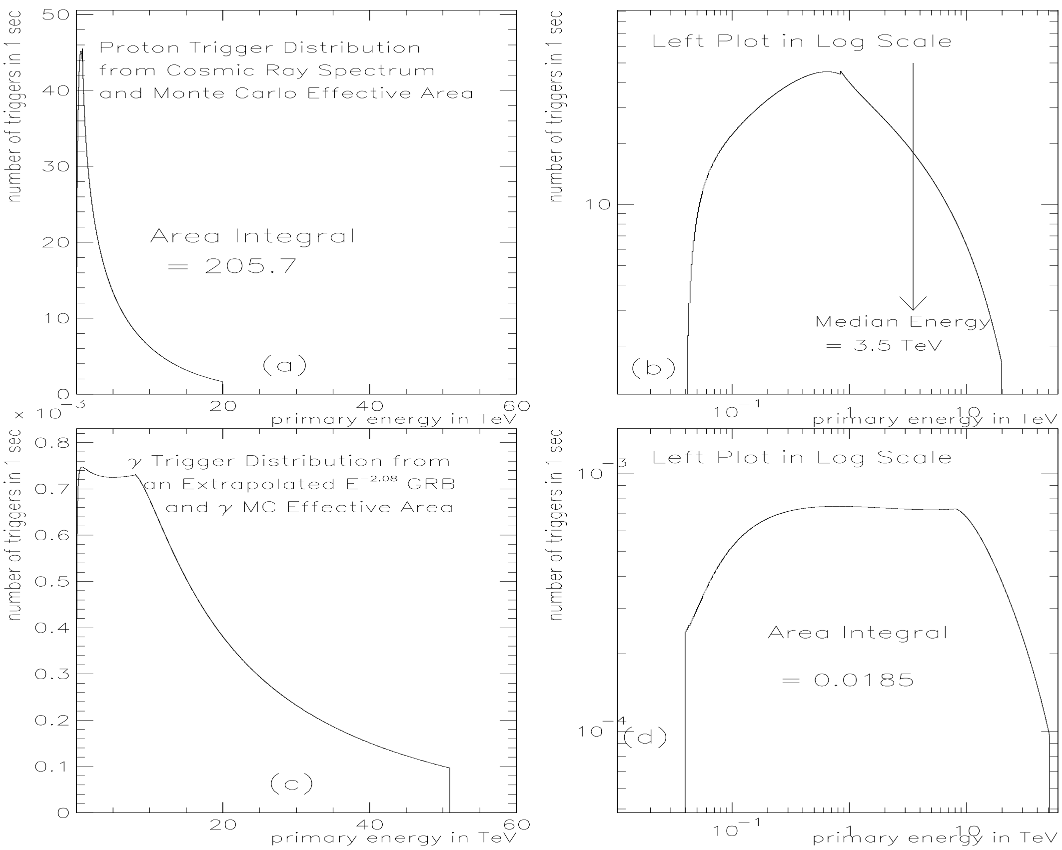

Figure 5.2: Milagrisimo trigger energy profiles for all-sky cosmic background (a), (b) and for an example of gamma-ray burst (a point source) (c), (d).

were carried out with 50% proton, 25% helium and 25% heavy primaries , instead of 100% proton primaries, the calculated trigger rate would be close to the experiment trigger rate of 125 s^{-1}.

Many ground-based experiments quote different cosmic-ray spectrum formulae. For example, the popular one derived from the results measured by the JACEE collaboration (Burnett, 1990; Nagle, 1988), states that the integral cosmic-ray all-particle flux from 100 GeV to $\sim$ 400 TeV is,

$$\phi_{cr}(>E) = (1.8 \pm 0.5) \times 10^{-5}\, E^{-1.76 \pm 0.09}\; cm^{-2}\, s^{-1}\, sr^{-1}. \tag{5.4}$$

After rearrangement, the differential cosmic-ray spectrum is,

$$\frac{dN}{dE} = 0.317\ \ E^{-2.76}\ m^{-2} s^{-1} sr^{-1} TeV^{-1}. \tag{5.5}$$

And, the new calculated trigger rate is,

$$N_p = \int_{0.04}^{20.} A_{peff}(E)\ \frac{dN}{dE}\ dE = 224.7\ s^{-1}, \tag{5.6}$$

which is close to the previous result of $206s^{-1}$ using Tibet's formula.

Nonetheless, from the plots, we can still fairly estimate the trigger threshold energy and the median energy for the Milagrisimo detector. The energy threshold is 100 GeV and the median trigger energy is 3.5 TeV.

Likewise, we can plug in a typical GRB flux to examine the γ trigger energy distribution. For example, the energy spectrum of GRB 940217 in Equation 1.1 can be simplified to,

$$\frac{dN}{dE} = 2.328 \times 10^{-5}\ E^{-2.08}\ \ photons\ m^{-2}\, s^{-1}\, TeV^{-1}.$$

If a GRB with this spectrum occurs (1) in the detector's field of view, (2) with a zenith angle of $\sim 30°$,[2] (3) emitting photons between 40 GeV and 50 TeV, and (4) for one second, the number of resulting γ triggers would be[3],

$$N_{1s} = \int_{0.04}^{50.} A_{\gamma eff}(E)\ \frac{dN}{dE}\, dE = 0.0185. \tag{5.7}$$

The contributions for this product is shown in Figure 5.2 (c) and 5.2 (d) in linear and log scale, respectively. The bump around 8 TeV is again caused by the sensitive nature of the integration, which amplifies the tiny roughness (refer to Figure 5.1) between the two parameterization regions in the effective area.

Compared to the previous proton result for the cosmic background trigger, the number of γ triggers is small. However, we should not compare that from the entire sky (the proton case) to that from a space point (the γ case).

To conclude this section, after we include all Monte Carlo events over a broad energy range and compare the calculated trigger rate with the experimental trigger rate, the simulations are believed to be reasonable and so are the effective areas and the median trigger energy for the detector.

5.2 Sensitivity and Optimal Bin Size

This section will first derive the detector's overall angular resolution for γ showers.

Referring back to the important plot of Figure 4.22 (b), we recall the nice agreement between the distribution of $\Delta_{even-odd}$ for Monte Carlo protons and the distribution of $\Delta_{even-odd}$ for real data. And, from all the good agreement in Chapter 3 when Monte Carlo results were compared comprehensively, we assume that the angular resolution distribution for the real γ triggered events, $\Delta_{true-recon}$(real data),[4] should match with the $\Delta_{true-recon}$ (MC γ) distribution. The smoothed and normalized $\Delta_{true-recon}$ (MC γ) distribution[5] is plotted in Figure 5.3 (a) to represent the angular resolution distribution for real γ events. The x-axis indicates the space angle difference in degrees between the direction of a reconstructed γ shower and the direction of the γ source ($x = 0.0$). The total area under the

[2] The median of the zenith angle distribution for γ triggered events.

[3] We cannot detect 0.0123 γ-ray, of course; we deal with probability here. If the GRB lasts for 1,000 seconds instead, we can use the number directly and expect a signal $\sim$12.

[4] $\Delta_{true-recon}$ stands for the space angle difference between the true shower direction and the reconstructed (fitted) shower direction.

[5] Obtained from fitting the first round 0.1-8 TeV 1,791 γ triggers.

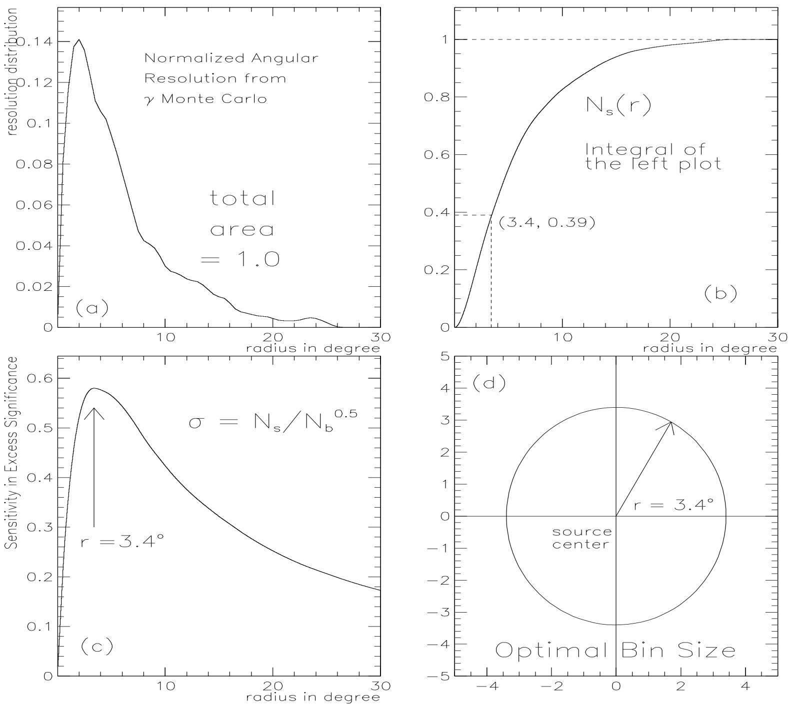

Figure 5.3: The sensitivity and optimal bin size calculation for the Milagrisimo detector.

curve has been normalized to 1.0. It has an longer tail than the one-dimensional counterpart of a two-dimensional Gaussian distribution, as shown in Figure 4.18.

Instead of fitting the $\Delta_{true-recon}$ distribution with a 2-D Gaussian, or extracting some parameters like the peak position or the median position from the distribution to give an "overall" angular resolution, I use the entire histogram itself (after some simple smoothing) to best represent the angular resolution for the detector for the following calculations. The integral of the curve in Figure 5.3 (a) is plotted in Figure 5.3 (b). The area from 0.0 to 3.4 degrees is 0.39, for example.

The idea of statistical significance of signal above background is defined as,

$$\sigma = \frac{Signal}{\sqrt{Background}} = \frac{N_s - N_b}{\sqrt{N_b}}, \tag{5.8}$$

where N_s is the counts in an on-source bin and N_b is the number in its corresponding off-source bin. It is a measure of probability on how far away a particular outcome deviates from random fluctuations of the background, in the absence of a signal. For the simplest case, one can choose the entire sky as the search bin, count how many events triggered during a particular burst interval, and compare the number with the average background trigger number for the same period of time. It is not too clever though, since the overwhelming number of background events can make the signal excess look insignificant. On the other hand, if the search bin (centered at the source, naturally) is chosen to be too small, according to the characteristic resolution distribution as seen in Figure 5.3 (b), there will be not many signal events included in the source bin either. We look for a compromise number between these two extremes and the criterion is to maximize the signal significance, σ.

Again, a time interval of one second is chosen since we can always in the end multiply any final calculated results by the real time span in seconds. Assume in 1.0 second, M γ rays come from a GRB and these M photons are distributed in reconstructed angles as in Figure 5.3 (a) (multiplied by M), according to the detector's angular resolution. As an alternative normalization scheme, it is equivalent to state that in 1.0 second 1.0 γ ray comes from a GRB and this signal is distributed according to Figure 5.3 (a). We accept for the moment the outcome of fractional trigger counts, keeping in mind that they get multiplied by the total rate and duration to give the real number of counts.

Then, a circle with a radius of r degrees can be placed and centered at the GRB. The solid angle, subtended by the cone defined by the circle and the detector is $2\pi\,(1-\cos r)$. Assume within this one second, all 125 background events come from directions between vertical and 60° away from vertical.[6] Even though the cosmic ray flux is isotropic in all directions at the top of atmosphere, the trigger density (number of triggers per unit of solid angle) is not constant in all directions. Figure 4.22 (f) shows the trigger density distribution versus the zenith angle. An overhead bin ($\theta = 0$) has 22 times more triggers than those at 60^o with the same bin size (solid angle). If the GRB is located at an average zenith angle, $\theta \sim 28^\circ$, such that the number of background events from inside the source bin circle is equal to,

$$N_b(r) = 125 \times \frac{2\pi\,(1-\cos r)}{2\pi\,(1-\cos 60^\circ)} = 250\,(1-\cos r),$$

we have,

$$\sigma(r) = \frac{N_s(r) - N_b(r)}{\sqrt{N_b(r)}} = \frac{N_{1s}(r)}{\sqrt{250(1-\cos r)}}.$$

For the circle radius r from zero to 30 degrees, the result of σ is shown in Figure 5.3 (c). $\sigma(r)$ peaks at $r = 3.4^\circ$. Thus, the best bin to search for an average angle GRB is a circular bin with a radius, $r = 3.4^\circ$. If the GRB occurs at a zenith angle other than the average angle, both $N_{1s}(r)$ and $N_b(r)$ vary roughly by the same factor. Since the radius $r = 3.4^\circ$ is small enough that the trigger density does not change much inside of the circle, the above significance function differs by a constant which depends on the zenith angle but not on r. Consequently, the optimal radius of $r = 3.4^\circ$ can be generally used to search for GRBs at any zenith angle.

If the angular resolution distribution of the detector is truly a 2-D Gaussian with standard deviation $\sigma = \sigma_\circ$, people "define" that the detector has an overall angular resolution of $\sigma_\circ$. The peak position of the 1-D counterpart can be shown to be equal to $\sigma_\circ$ and, furthermore, the radius of the corresponding optimal circular bin can be proven to be, $r_\circ = 1.6 \times \sigma_\circ$.

Now the radius of the optimal bin for Milagrisimo has been derived by another independent method to be 3.4° because its distribution is not Gaussian. We can derive an equivalent overall angular resolution for the detector by removing the factor 1.6:

$$Milagrisimo\ \ angular\ \ resolution = \frac{3.4^\circ}{1.6} = 2.1^\circ.$$

[6]This actually covers 96% of all triggers, see Figure 4.22 (e).

Incidentally, the peak position in Figure 5.3 (a) sits close to 2°. From the data, there is no evidence showing that the angular resolution of a $\theta = 60°$ trigger is worse than that of a $\theta = 0°$ trigger, albeit in theory the shower front of a tilted shower is thicker than that of a vertical shower because of the longer passage in air. For now, we assume a constant angular resolution over all angles for the following sensitivity discussion.

If GRB 940217, with flux described by Equation 1.1, with a zenith angle of $\sim 28°$, and with an emission duration of 90 min (T), occurs within Milagrisimo's field of view and its energy spectrum continues all the way to 50 TeV (and cuts off after 50 TeV), the calculated detection significance using a 3.4° circular bin is given by,

$$\sigma = \frac{N_{1s} \times 0.39 \times T}{\sqrt{250\,(1 - \cos 3.4°) \times T}} = \frac{0.0185 \times 0.39 \times \sqrt{T}}{\sqrt{0.44}} = 0.8. \tag{5.9}$$

This is not too impressive.

If the GRB happens right overhead, instead of at 28°, the number of background events doubles as shown in Figure 4.22 (f), but similarly, the effective area for γ doubles as well, which in turn makes the trigger number $N_{1s} = 0.0185 \times 2$. However, due to the definition of σ, there is a factor of $\sqrt{2}$ net increase.

Notice the energy spectral index in Equation 1.1 has an error of 0.56. If, one sigma away, we use $E^{-1.52}$ instead of $E^{-2.08}$ and still require a cut-off energy at 50 TeV, the significance will go up to,

$$\sigma = \frac{0.172 \times 0.39 \times \sqrt{90 \times 60}}{\sqrt{0.44}} = 7.6.$$

If the above two optimistic conditions occur simultaneously, we have a GRB signal significance of 11 sigmas.

Take the "Super Bowl" burst as another example. The spectrum in Equation 1.2 can be simplified to,

$$\frac{dN}{dE} = 0.001227 \;\; E^{-2.03} \; m^{-2} s^{-1} TeV^{-1}.$$

If again the energy cuts off at 50 TeV, the one-second integration number is 1.103, which is 60 times larger than the number 0.0185 in GRB 940217. Its characteristic time interval, 25 s, however, is much shorter than the 90 min interval in the previous example. Nonetheless, if it occurs right overhead, Milagrisimo will detect this burst with a signal strength of 4.6 σ.

As noticed in Equation 5.9, signal significance is favored by a factor of $\sqrt{T}$, even though both background counts and signal counts increase linearly with time T. The longer the exposure time, the better the signal significance. If, in the extrapolated 50 TeV energy range, an overhead "Super Bowl" burst could last for 2 min, instead of 25 seconds, the final significance ends up at 10 sigmas.

After these discussions, we conclude that the Milagrisimo detector is sensitive to γ-ray bursts and it is worthwhile to run through the experimental data to search for GRBs.

5.3 BATSE Gamma-Ray Burst Catalog

To cross check with BATSE's GRB candidates is one of the main motivations to operate the Milagrisimo experiment. Now that the data are reconstructed and ready to

GRB No.	run No.	time	θ	ϕ	α	δ	point error radius	T_{90} (sec)	T_{start} (sec)	Flux $\times 10^4$
960425	221	1112.78	40.0	156.9	59.9	40.8	5.08	N/A	N/A	0.44
960507	283	84959.69	35.1	201.7	79.2	17.9	8.30	0.985	-0.256	0.41
960513	331	80259.66	38.5	232.0	77.1	3.5	14.8	0.336	-0.104	0.21
960521	440	29146.83	38.5	46.9	303.2	55.8	2.56	16.29	-7.168	0.66
960521B	442	33806.73	17.9	156.5	251.6	41.1	3.48	2.970	-0.002	1.12
960525	561	84750.03	18.9	73.8	139.1	53.8	1.47	18.43	-1.280	0.81
960529	644	43665.10	39.6	35.8	14.4	48.9	0.36	17.09	0.128	18.43
960601	725	65576.01	41.8	120.0	5.6	64.8	3.90	2.560	-0.256	0.83
960607	847	78075.59	49.6	108.1	48.4	75.1	0.36	140.48	4.992	8.74
960615B	922	14822.35	26.8	94.5	214.4	62.6	14.5	0.769	-0.64	0.23
960616	940	66495.56	33.8	63.0	109.1	62.7	2.56	0.064	-0.064	0.29
960618	958	8000.20	17.7	77.8	199.4	53.0	4.56	N/A	N/A	0.66
960620	982	19535.56	31.9	184.2	206.9	27.8	5.19	6.720	-1.920	0.29
960621B	992	23685.83	26.8	344.9	290.5	25.3	2.84	50.72	-2.832	0.38
960621D	1000	80608.97	48.9	131.3	71.6	57.5	8.47	N/A	N/A	N/A
960623	1018	4728.52	28.5	262.2	180.8	7.6	0.74	90.36	-44.03	3.13

Table 5.2: A list of BATSE's GRBs that are in the field of view of Milagrisimo. There are eleven columns in the table: (1) GRB No. is the BATSE 4B catalog gamma-ray burst identifier, (2) run No. is the corresponding Milagrisimo run number, (3) time is the universal time in seconds after midnight, (4) θ is Milagrisimo's local incident zenith angle in decimal degrees, (5) ϕ is Milagrisimo's local incident azimuth angle in decimal degrees, (6) α is right ascension (J2000) in decimal degrees, (7) δ is declination (J2000) in decimal degrees, (8) point error is the radius in decimal degrees of the positional error disc, (9) T_{90} is the duration of the time interval during which 90% of the total observed counts have been detected, (10) T_{start} is the start time of the T_{90} interval relative to the trigger time, and (11) flux is the peak flux (in $photons/m^2/sec$) calculated using a time interval of 1,024 ms and an energy range of 50-300 keV.

search for sources, we make a list of all BATSE GRBs (Paciesas, 1997) which are also in the field of view of the Milagrisimo experiment. That means the experiment has to be up and running during the GRBs, and the zenith angles of GRBs have to be less than 50° (this is an arbitrary but rather conservative cut).

The selected candidates are summarized in table 5.2. To fit the table in one page, the Julian days for bursts are not listed. The first burst (960425) has Julian day 2450198.5 and the last burst (960623) has Julian day 2450257.5. There are a few disappointing facts: (1) there are not many GRBs overlapping with Milagrisimo, (2) there are no really overhead GRBs other than three bursts at 18°, (3) a few GRBs have position errors larger than Milagrisimo's optimal bin size of 3.4°, (4) several GRBs do not have hits recorded in the highest energy channel (> 300 keV) on BATSE, which makes the assumption of energy extrapolation inappropriate, and (5) three GRBs have incomplete data information.

BATSE also publishes the light curve for each burst. For examples, Figure 5.4 shows

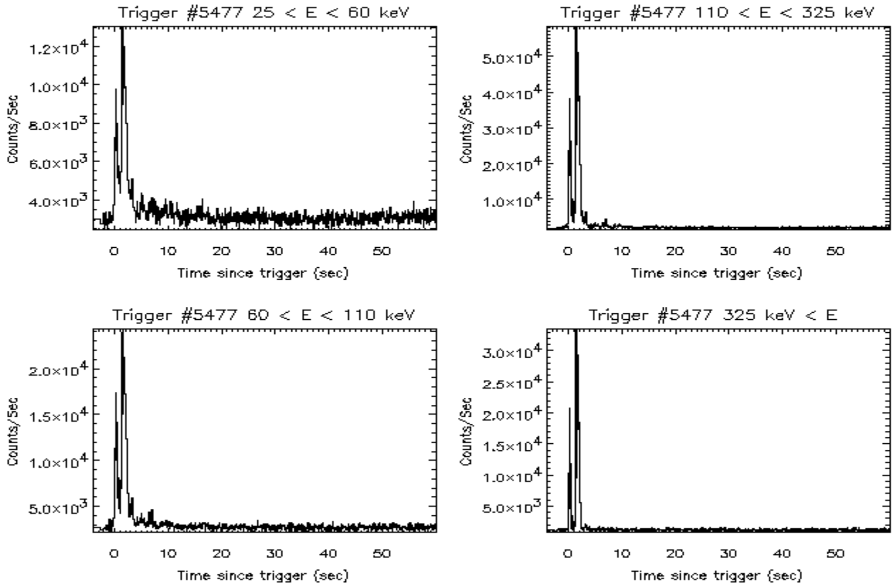

Figure 5.4: The light curve of GRB 4B 960529.

the light curve of GRB 4B 960529, and Figure 5.5, GRB 4B 960607. As described in Section 1.2, BATSE instruments have 4 different energy bins. In the light curve plots, the x-axis stands for time and time zero is the trigger time. Different GRBs can have very different light curves.

5.4 Search Method and Background Estimation

After the bin size and source positions are available, we can count air showers from inside the bin as the on-source events (N_s in Equation 5.8). How do we count the off-source events (N_b in Equation 5.8)? It is very important to precisely determine the background counts in the GRB search.

A celestial body, seen by an observer on the ground, moves at the fastest 360° a day, or 0.0042° per second, in terms of zenith angle. From the short time interval of GRBs (see Table 5.2), we can assume with small error that the source does not move during the entire period of γ emission. A regular Milagrisimo run with one million triggered events lasted about 2 hours. Here, just like what we did in deriving the optimal bin size, it is most helpful to go through a numerical example to explain how to estimate the background for a GRB.

Consider an imaginary GRB (which is not in our source list) which occurred on Julian Day 2450218.5 and at Julian Second 26394.9. We find it is covered in Run 350 of the Milagrisimo data. To make the example more general compared to the tabulated list, we further arbitrarily assign that it has, $T_{90} = 60s$, $T_{start} = -0.1s$, and an location at $(\theta_\circ, \phi_\circ) = (16.56°, 105.13°)$ with a 0.34° positional uncertainty.[7] According to these input numbers, we can select within Run 350 all the reconstructed showers whose coordinates

[7]The issue of BATSE's position errors will be addressed later.

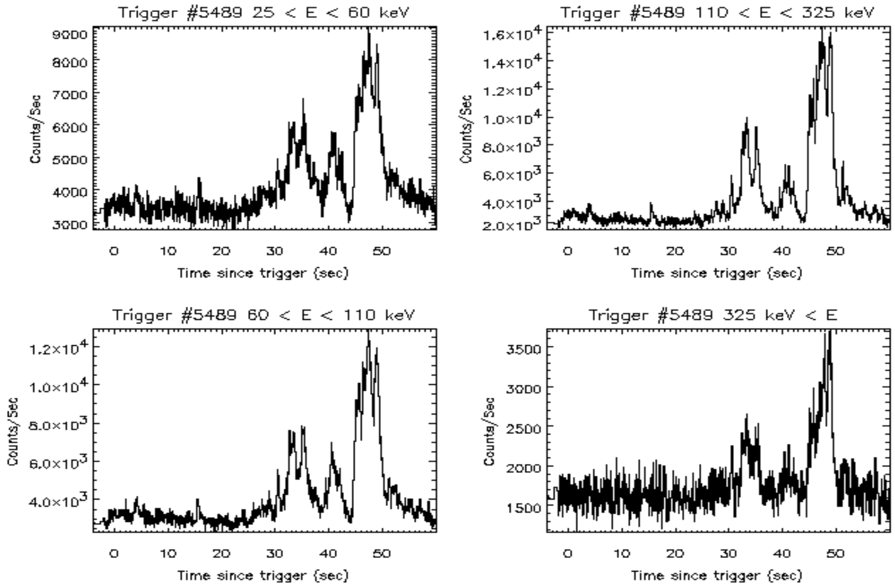

Figure 5.5: The light curve of GRB 4B 960607.

θ, ϕ are within 3.4° from the source location, (16.56°, 105.13°). Thus, the GRB turns on at $t_\circ = 26394.9 - 0.1 = 26394.8s$, lasts for 60 seconds and stops at 26454.8 s. As shown in Figure 5.6, after the time for the on-source bin has been pinpointed, we can further divide both forward and backward in time the rest of the events into many 60-second equal-interval bins until all the events are exhausted. In Run 350 (which has 10^6 triggers), there are 128 such 60 second bins plus two fractional intervals (less than 60 seconds) at the two ends. The GRB's on-source bin is found at bin number 26 and it has 51 events in it. All the rest of the 128 bins[8] are off-source bins for the GRB. Here we introduce some convenient notations, which will be used consistently throughout the rest of this chapter. The number of events in the on-source bin is,

$$N_s = N_{26} = 51,$$

and the expected number of events in an off-source bin is,

$$N_b = \frac{N_B}{m} = \frac{(\sum_{i=1}^{128} N_i) - N_{26}}{128 - 1} = \frac{7179 - 51}{127} = \frac{7128}{127} = 56.13.$$

The important integer, $m = 127$, is defined as the number of background bins. The integer, N_B, is the sum of event counts from m off-source bins.

The GRB's source bin contains 51 events while the expected background is 56.13. According to the definition in Equation 5.8, it thus has a negative signal excess, or a deficit.

Since the source is imaginary and randomly chosen from within Run 350, there is no real GRB candidate recorded by BATSE during that particular time and at that particular location. Therefore, all the 128 60-second blocks can be treated as background bins. The next question is how these 128 numbers are distributed relative to the mean value of 56.13. The 128 numbers are plotted in Figure 5.7(a). How can we decide if this

[8]The two partial bins are not used.

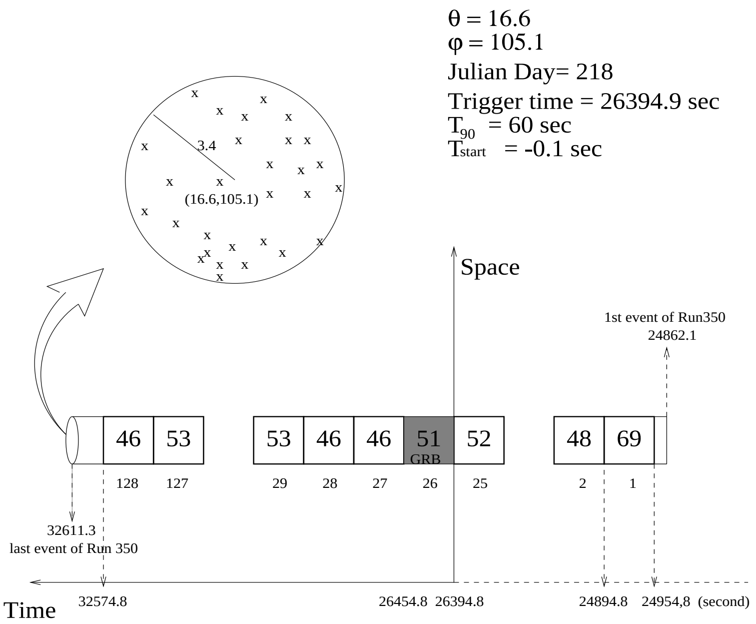

Figure 5.6: The on-source bin and off-source bins in a GRB search. The time direction runs from right to left on the x-axis.

distribution is well behaved before we use this search method to look for real GRBs? Prior to examining the background fluctuations, we also want to know if there are other influences that could affect the outcomes from bin to bin.

Other than the early assumption that a GRB does not move during its bursting interval, there are two more considerations supporting the described method: (1) a Milagrisimo run is long enough compared to the burst's duration (a factor of 128 in the example) that many background entries can be accumulated to average out the fluctuations, and (2) on the other hand, a Milagrisimo run is short enough ($\sim$ 2 hours) that the global environment (atmosphere, water depth, temperature, etc) of the experiment does not change much during a run. That is to say, the trigger rate is stable (constant). The numbers of total triggers (including all events outside the 3.4° circular bin) in 60-second intervals for Run 350 are plotted in Figure 5.7(b). As can be seen, the $\pm$100 or so fluctuation is only 1.3% of the average trigger number ($\sim$7450).

Now the question whether the background distribution (Figure 5.7(a)) makes sense has to be answered before we can actually use the described method. We can put more entries in the histogram and see how well it matches with certain underlying function, and the number of entries, m, can be increased by using more data runs. However, doing so will affect the suitability of the method because the global environment can change over a longer period of time. Nevertheless, people have tried to examine the background distribution itself, but concluded it is not effective.

Fortunately, for the source search techniques in VHE and UHE astrophysics, there are two more sensitive and commonly used quantities (parameters) developed to check if a background distribution is well behaved. They are the Probability, $P(\geq N_s|N_B, m)$, and the Li-Ma significance. Their meanings are described below.

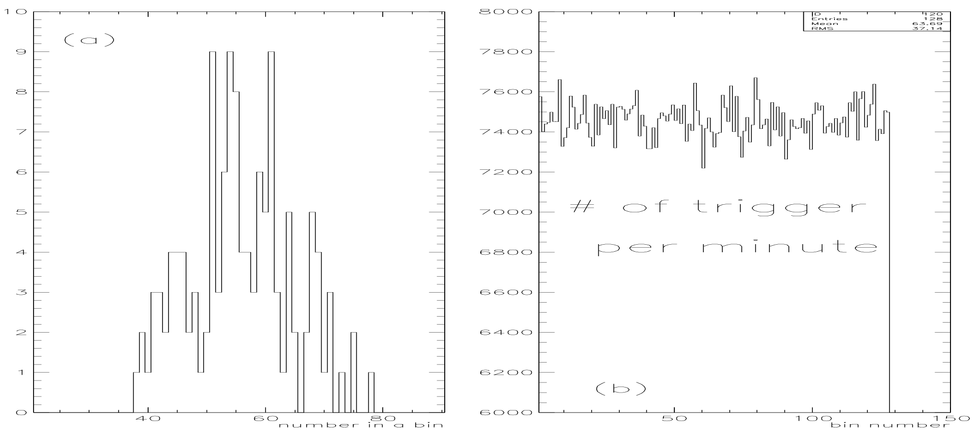

Figure 5.7: Histogram (a) shows the background fluctuation (distribution), and (b) shows the profile of the experiment trigger rate (per minute) over the entire run of Run 350.

5.4.1 Probability $P(\geq N_s|N_B, m)$

It is most desirable to directly derive the exact probability for each possible outcome, after observing a set of event distributions under the same conditions. Therefore, in a GRB search, we can directly quote the probability for obtaining that particular source bin count from the observed background distribution. Here, we have to assume that there are no real sources during the observation of "background" distribution, or this method will be strongly biased.

$P(\geq N_s|N_B, m)$ stands for the probability (or joint probability) of obtaining N_s or more counts from a fluctuation of the background, given the observed values of N_B and m. The notations N_s, N_B, m, and N_b all have the same meanings as in the example in the previous section. By definition,

$$P(\geq N_s|N_B, m) = P(N_s|N_B, m) + P(N_s+1|N_B, m) + P(N_s+2|N_B, m) + ... + P(\infty|N_B, m),$$

or equivalently[9]

$$P(\geq N_s|N_B, m) = 1. - \sum_{i=0}^{N_s-1} P(i|N_B, m).$$

We can expand the probability over all possible true background state, x, such that[10]

$$P(\geq N_s|N_B, m) = 1. - \sum_{i=0}^{N_s-1} \int_0^\infty P(i|x)P(x|N_B, m)\, dx.$$

Bayes' formula states

$$P(x|y) = \frac{P(y|x)P(x)}{\int_0^\infty P(y|x)P(x)\, dx}.$$

[9]Individual probability can be obtained by the difference between two consecutive $P(\geq N_s|N_B, m)$'s. For example, $P(51|7128, 127) = P(\geq 51|7128, 127) - P(\geq 52|7128, 127)$.

[10]The P's inside the integral are the corresponding probability density functions. The same notation as the probability is used since it is understood.

The probability expression becomes

$$P(\geq N_s|N_B,m) = 1. - \sum_{i=0}^{N_s-1} \frac{\int_0^\infty P(i|x)P(N_B,m|x)P(x)\,dx}{\int_0^\infty P(N_B,m|x)P(x)\,dx}.$$

Now, we have to assume the *a priori* probability:

$$P(x) = constant \;\; if \;\; x \geq 0;$$

$$P(x) = 0 \;\; if \;\; x < 0.$$

It means that *before* we actually measure the quantities and acquire the numbers, N_s, N_B, and m, we have no knowledge whatsoever about the probability distribution $P(x)$, except we know that the numbers, N_s, N_B, cannot be negative. For example, without conducting any measurement, we do not know if $P(55)$ is bigger or smaller than $P(12)$. The idea is if we do not know anything about them, they might as well be the same!

$P(i|x)$ is the probability (density) to observe an outcome of i counts given a true background count rate of x, and it is found to follow the familiar Poisson distribution,

$$P(i|x) = \frac{x^i\, e^{-x}}{i\,!} \quad .$$

Similarly,

$$P(N_B,m|x) = \frac{(mx)^{N_B}\, e^{-mx}}{N_B\,!} \quad .$$

Since $P(x)$ is assumed to be constant over all positive x values, the two $P(x)$'s in the formula cancel each other.

The original probability expression becomes

$$P(\geq N_s|N_B,m) = 1. - \sum_{i=0}^{N_s-1} \frac{\int_0^\infty (\frac{x^i\, e^{-x}}{i\,!})(\frac{(mx)^{N_B}\, e^{-mx}}{N_B\,!})\,dx}{\int_0^\infty \frac{(mx)^{N_B}\, e^{-mx}}{N_B\,!}\,dx} \quad . \tag{5.10}$$

We can simplify the integrals by repeatedly using the formula

$$\int_0^\infty e^{-kx}\, x^i\; dx = \frac{i\,!}{k^{i+1}}.$$

Below, I rearrange the final equation in such a way that it can be directly used in a computer program to calculate the numerical answer:

$$P(\geq N_s|N_B,m) =$$

$$1. - (\frac{m}{m+1})^{N_B+1}\{1 + \sum_{i=1}^{N_s-1}[(\frac{N_B+1}{1\cdot(m+1)})\cdot(\frac{N_B+2}{2\cdot(m+1)})\cdot(\frac{N_B+3}{3\cdot(m+1)})\cdot ...(\frac{N_B+i}{i\cdot(m+1)})]\}$$

Notice the extra 1 before the summation symbol which is the original index $i = 0$ entry from inside the summation.

Once the three numbers N_s, N_B and m are available, the probability $P(\geq N_s|N_B,m)$ can be calculated directly. In the example of our previous imaginary GRB, the corresponding number is, $P(\geq N_s|N_B,m) = P(\geq 51\,|\,7128,127) = 0.77$. We can interpret it from the definition: under the circumstance that there are 7128 counts selected in "a" background bin, which is 127 times longer than the signal bin,[11] the chance in the absence of a signal to observe, in the signal bin, 51 counts, or 52 counts, or 53... or ∞ is 77%.

After all this, what does it tell us about the suitability of our proposed search method? The explanation of its use will follow after the next subsection.

5.4.2 Li-Ma significance

While the previous section thoroughly explained how likely an observed excess is caused by pure luck, Li and Ma in 1983 (Li & Ma, 1983) introduced an easier method. They defined a parameter, S, of which the absolute value is given by

$$|S| \equiv \sqrt{2[N_s \ln(\frac{(m+1)N_s}{N_s+N_B}) + N_B \ln(\frac{m+1}{m}\frac{N_B}{N_s+N_B})]}. \tag{5.11}$$

The sign of S can be either positive or negative and it depends on if $N_s > N_b$ or $N_s < N_b$. This S parameter has the same meaning as our statistical significance, $\sigma = \frac{S}{\sqrt{B}} = \frac{N_s - N_b}{\sqrt{N_b}}$, and thus we can use S to redefine the statistical significance if we want to.

The main point Li and Ma proved is that, if there is no source, and hence the outcome of N_s is governed by pure luck, after many such observations (many different S values), the S distribution is Gaussian.

The formula is easy to calculate. In one histogram, we can both show the signal significance, if there is any, and examine the behavior of background fluctuations.

The only drawback, as will be shown soon, of Li-Ma significance is that it is not suitable when the value of N_s (or N_b) is too small ($< \sim 10$). When these two values drop below $\sim$10, the values of S become quantized, the left (negative) side of the distribution disappears, and it deviates from Gaussian. Unfortunately, many GRBs with short time intervals end up with small values of N_s (and N_b). Nevertheless, the Li-Ma significance is presented here since people are familiar with it, and it can be used to cross-check the distribution for $P(\geq N_s|N_B, m)$ in the next section when $N_s > 10$.

5.4.3 Background Profile

As indicated in the previous section of Li-Ma significance, we need many independent sets of (N_s, N_B, m) values (under the same conditions) to examine the background fluctuations. It is the case for $P(\geq N_s|N_B, m)$ as well. In the numerical example, the result, $(N_s, N_B, m) = (51, 7128, 127)$, gives only one value of P, which is 0.77 as we calculated. Instead of bin #26, if we choose bin #27 as the source bin and treat the rest as background bins, we can have a new number set, $(N_s, N_B, m) = (46, 7128, 127)$, and thus a new P value. After repeating this pattern 128 times, we can generate 128 P values (and 128 values of Li-Ma significance). However, this is not enough. Since we want to avoid overly sampling the same data, many runs are needed for a valid check.

Run 503 (with 10^6 triggers) is processed first; I pick an arbitrary but fixed θ value of 25°, a ϕ value of 36°, and a random time between 0 and 20 seconds (as an offset between the first event in Run 503 and the start time for the first bin), and as before, I place a

[11] The average count is 56.1.

3.4° circular bin centered at (25°, 36°) to select events and use a 60-second time interval to further slice these spatially selected events into serial time bins. The events in each bin are counted and I get[12] 128 different numbers (43,49,...,41).[13] Given these 128 numbers and following the pattern just described few sentences ago, I generate 128 P values and 128 Li-Ma significance values. They are entered in two histograms. This finishes the first round.

In the second round with Run 503, I select a new value of $\phi = 72°$ and a new random time offset between 0 and 20 seconds, while still use the same θ value of 25°. The resulting set of N_s's are similar to those in the first round, but different. In this way, I create another ~128 $P(\geq N_s|N_B, m)$ entries and ~128 Li-Ma significance entries in the two histograms. In the third round, $\phi = 108°$ is used. Run 503 is repeated for 10 rounds in total with the same θ angle of 25° but with various ϕ angles: 36°, 72°, 108°,..., and 360°. In the end, about 1,280 entries of P and Li-Ma values are accumulated in the two histograms. This finishes Run 503.

The same 10-round procedure is applied to the next data run, Run 504, with the same $\theta = 25°$ and the 10 corresponding ϕ angles: 36°, 72°, 108°,..., and 360° to make about[14] 850 entries in both the $P(\geq N_s|N_B, m)$ and the Li-Ma histograms. Run 505 is started after Run 504 is finished, and so on. The last run used in this entire exercise is Run 653.

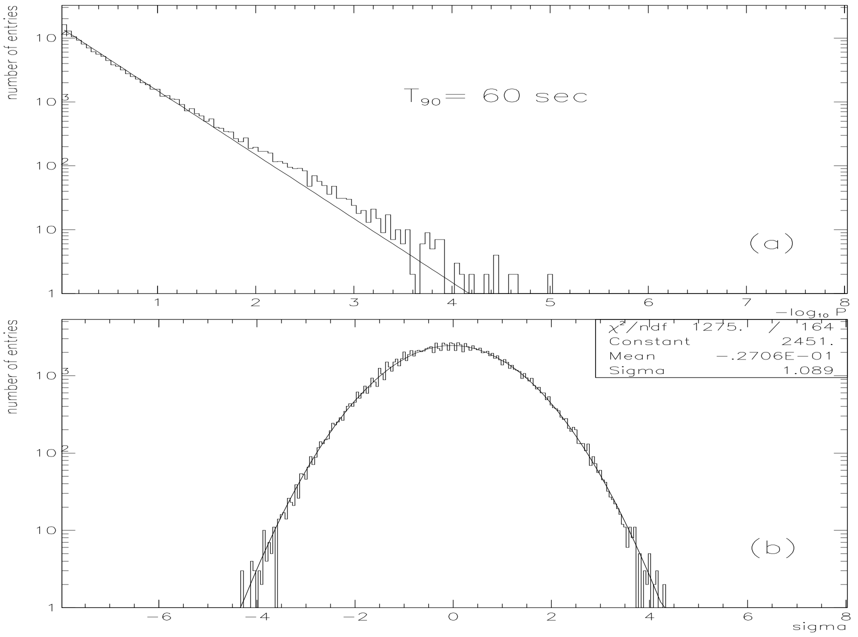

Figure 5.8: (a) The $P(\geq N_s|N_B, m)$ distribution, and (b) the Li-Ma significance distribution. The smooth solid curves are explained in the text.

[12] This is a coincidence. Because of the different run durations and the different time offsets just introduced, the number is not necessarily 128.

[13] N_b is equal to 42.7, instead of 56.1, because θ now is different.

[14] Run 504 lasted less than 2 hours.

	Li-Ma significance
$P(\geq\ 0\|5423, 127) = 1.$	-
...	...
$P(\geq 20\|5423, 127) = 0.9999591$	-3.868819
...	...
$P(\geq 26\|5423, 127) = 0.9975320$	-2.748128
...	...
$P(\geq 33\|5423, 127) = 0.9450465$	-1.541266
...	...
$P(\geq 38\|5423, 127) = 0.7836602$	-0.730452
...	...
$P(\geq 40\|5423, 127) = 0.6805450$	-0.416182
$P(\geq 41\|5423, 127) = 0.6230602$	-0.261020
$P(\geq 42\|5423, 127) = 0.5632094$	-0.107120
$P(\geq 43\|5423, 127) = 0.5023678$	0.045556
$P(\geq 44\|5423, 127) = 0.4419462$	0.197043
$P(\geq 45\|5423, 127) = 0.3832948$	0.347375
...	...
$P(\geq 58\|5423, 127) = 0.0152391$	2.209291
...	...
$P(\geq 80\|5423, 127) = 0.0000006$	5.059358
...	...
$P(\geq 99\|5423, 127) = 0.0000003$	7.302215
...	...

Table 5.3: Example values for the relation between numbers and $P(\geq N_s\,|N_B, m)$. Not all of them occur in the data.

The resulting $P(\geq N_s|N_B, m)$ histogram, with all entries from Run 503 to Run 653, is plotted as Figure 5.8 (a). Note the x-axis has been relabeled from $P(\geq N_s|N_B, m)$ to $-log_{10}\ P(\geq N_s|N_B, m)$, and a log scale is used on the y-axis to make visual checking easier. The histogram is fitted with a straight line under the requirement that the entry number (y-axis) drop in decades be equal to the probability (x-axis) drop in decades. As can be seen, the fitted line drops 4.2 decades in y-axis and drops 4.2 decades in x-axis as well.

Table 5.3 shows the relation between some specific numbers and $P(\geq N_s\,|N_B, m)$. The allowed P values are actually discrete within the region of [1,0]. Since the most probable N_s is roughly equal to $N_b = 42.7$, it makes sense that $P(\geq 43|5423, 127)$ has ~50% in probability.

Because of the integral nature of the definition of $P(\geq N_s\,|N_B, m)$,

$$P(\geq N_s|N_B, m) = \sum_{i=N_s}^{\infty} P(i|N_B, m),$$

if the condition for the *a priori* probabilities,

$$P(0) = P(1) = P(2) = \cdots = P(\infty),$$

is true, and the fluctuations of the background follow Poisson statistics, the resulting $P(\geq N_s|5423, 127)$ distribution will exactly match the fitted line in Figure 5.8 (a). Now that the histogram agrees with the fitted line well, this confirms the validity of the early assumption we made about the *a priori* uniform distribution of probability, which is believed what a truly random fluctuation should obey.

The normalization factor (the y-intercept) shows the number of trials under the same conditions of $(N_B, m) = (5423, 127)$. Out of ~16,000 trials, there are ~16 occurrences sitting at the probability of ~0.001, which makes sense.

The little difference, however, between the histogram and the fitted line results from the fact that not all entries occurred under the exact same conditions, $(N_B, m) = (5423, 127)$, or the same $N_b = 42.7$. Some runs are shorter than two hours.[15] The water depth, temperature, and pressure can slightly change among different runs and cause small difference in N_b. Most of all, as shown in Figure 4.22 (d), the event density at different ϕ angles can be different. To be conservative, we can use the histogram itself to quote the probability for a source bin count; for example, if $P(\geq N_s|N_B, m)$ is 10^{-3}, we can correct it to be 2×10^{-3}.

In Figure 5.8(b), the resulting Li-Ma significance distribution is plotted on a log scale to blow up the two tails. A Gaussian function fits the distribution well with the fitting statistics shown on the upper corner. As described in the previous subsection, truly random background fluctuations will generate a Gaussian distribution in Li-Ma significance.

By examining the tails in both Figure 5.8 (a) and Figure 5.8 (b), we can also visually spot candidate signals. For example, given $(N_B, m) = (5423, 127)$, if we detect a GRB with the on-source count, $N_s = 80$, for which the Li-Ma significance is 5.06 σ[16], the probability that this outcome results from random fluctuation is less than 6×10^{-7}. This particular entry will stand out obviously in both plots.

Since the 60-second duration is at the long end of the range of T_{90} on the GRB source list, we have to reduce the T_{90} to 10 seconds and repeat the same exercise. Instead of values in the low 40's, the new N_s and N_b are around 10 now and the m value goes up to ~768 for the same data Run 503. The resulting $P(\geq N_s|N_B, m)$ and Li-Ma significance distributions are plotted in Figure 5.9 (a) and Figure 5.9 (b) respectively. Unlike the 60-second case, we notice there are bumps in the two distributions. This is caused by the smaller number of events (~10, compared to 43) and the distribution starts to be quantized. The probability histogram still agrees with the uniform probability distribution. The Li-Ma distribution, on the other hand, starts to deviate from the symmetrical Gaussian.

Figure 5.9 (c) and Figure 5.9 (d) shows the extreme case of $T_{90} = 1$ second, where N_s and N_b values are around 1. The distributions now show ~9 discrete bands. If the expected background is $N_b = 0.91$, for example, we have a decent chance to observe zero as well as one or two events.[17] However, when N_s reaches 8, P is already $\sim 10^{-5}$. We practically only have a few discrete choices for the possible outcomes. These bands should

[15] This should not matter, as long as N_b remains the same and m is large enough.
[16] For comparison, $\sigma = \frac{S}{\sqrt{B}} = \frac{80-42.7}{\sqrt{42.7}} = 5.71$ sigmas.
[17] This is the familiar Poisson distribution.

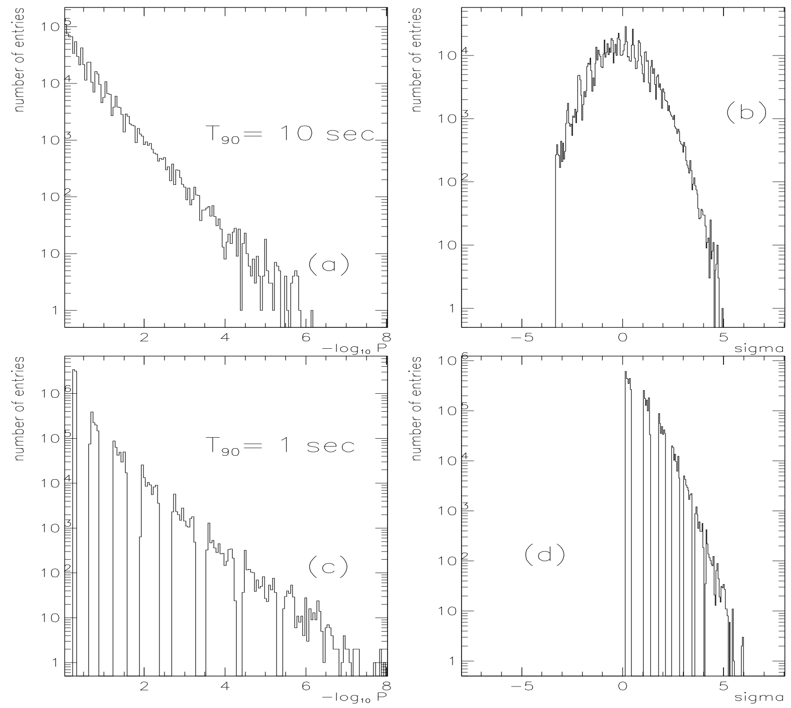

Figure 5.9: Top row: the distribution of $P(\geq N_s, N_B, m)$, and Li-Ma significance in 10 second intervals. Bottom row: the distributions in 1 second intervals.

degenerate into discrete sharp lines, if all N_s entries are conducted truly under the same condition where the values of (N_B, m) are identical. Nevertheless, the histogram still agrees with the uniform (but discrete) distribution of probability.

Overall, the background distribution of the proposed GRB search method for time periods down to one second is well behaved. The search method is verified.

5.5 Upper Limits

In case there is no statistically significant result found from a source, the numbers (N_s, N_B, m) can be used to derive an upper limit for the possible signal from the source. For example, a search result of $(N_s, N_B, m) = (10, 101, 10)$ looks unimpressive, but it is telling us, "I am 95% sure that the pure signal from that source is less than 8.25."[18]

Assume there is a joint probability density function $P(s, b|N_s, N_B, m)$ describing the probability density of the expectation of the source and background contributions being s and b, given the observations, N_s and N_B,

$$\int_0^\infty \int_0^\infty P(s, b|N_s, N_B, m)\ ds\ db = 1.$$

From now on, the symbol m, for it is understood and defined after N_B, is dropped from

[18]Contribution from source alone, not "source plus background".

formulae to clean up the appearance. We wish to obtain a 90% confidence level upper limit to the source contribution, N_{90}. The definition can be mathematically translated to

$$\int_0^\infty \int_0^{N_{90}} P(s,b|N_s,N_B)\ ds\ db = 0.9,$$

or

$$\int_0^\infty \int_{N_{90}}^\infty P(s,b|N_s,N_B)\, ds\, db = 0.1.$$

From the result of Bayes' theorem

$$P(x|y) = \frac{P(y|x)P(x)}{\int_0^\infty P(y|x)P(x)\ dx},$$

the N_{90} equation becomes

$$\frac{\int_0^\infty \int_{N_{90}}^\infty P(N_s,N_B|s,b)P(s,b)\, ds\, db}{\int_0^\infty \int_0^\infty P(N_s,N_B|s,b)P(s,b)\, ds\, db} = 0.1.$$

As in the treatment when deriving Equation 5.10, we once again assume the *a priori* uniform distribution of probability,

$$P(s,b) = \ constant;\ for\ s\ \geq\ 0\ and\ b\ \geq\ 0\ ,$$

so the factors $P(s,b)$ can be taken out of the integral and cancel each other. From equation 5.10, the integrand,

$$P(N_s,N_B|s,b) = \frac{(s+b)^{N_s}\ e^{-(s+b)}}{N_s\ !} \frac{(mb)^{N_B}\ e^{-(mb)}}{N_B\ !},$$

is the probability of obtaining the observations N_s, N_B given s and b, and is obtained using the Poisson distribution.[19] The N_{90} equation becomes

$$0.1 = \frac{\int_0^\infty \int_{N_{90}}^\infty (s+b)^{N_s}\ e^{-(s+b)}\ b^{N_B}\ e^{-(mb)}\, ds\, db}{\int_0^\infty \int_0^\infty (s+b)^{N_s}\ e^{-(s+b)}\ b^{N_B}\ e^{-(mb)}\, ds\, db}.$$

After a suitable change of variables and repeated use of the following integral, obtained by repeated integration by parts,

$$\int_t^\infty e^{-ax}\ x^n\ dx = \frac{e^{-t}\ n\,!}{a^{n+1}} \sum_{i=0}^{n} \frac{t^i}{i\ !}$$

(true as well for $t = 0$, which is needed), the N_{90} equation can be shown, (Sinnis, 1992) and (Biller, 1992), to be:

$$0.1 = \frac{e^{-N_{90}}\ \sum_{i=0}^{N_s} \sum_{j=0}^{i}\ N_{90}^{i-j} \frac{i\,!}{(i-j)\,!\,j\,!} \frac{(N_B+j)\,!}{(m+1)^j\ i\,!})}{\sum_{k=0}^{N_s} \frac{(N_B+k)\,!}{k\,!\ (m+1)^k}}.$$

[19]Notice that the symbol s now is pure signal from the source, while N_s means signal plus background.

To facilitate computation, the above formula can be rearranged to

$$0.1\ e^{N_{90}} = \frac{1+\sum_{i=1}^{N_s}\{\frac{N_{90}^i}{i!}+\sum_{j=1}^{i}[\frac{N_{90}}{i-j}][\frac{N_{90}}{i-j-1}]\cdots[\frac{N_{90}}{1}][\frac{N_B+j}{(m+1)j}][\frac{N_B+j-1}{(m+1)(j-1)}]\cdots[\frac{N_B+1}{(m+1)1}]\}}{1+\sum_{k=1}^{N_s}[\frac{N_B+k}{(m+1)k}][\frac{N_B+k-1}{(m+1)(k-1)}]\cdots[\frac{N_B+1}{(m+1)1}]}.$$

The N_{90} value can be found by using a root-finding algorithm, for example, the one by Brent (Press, 1990).

After N_{90} is calculated, we can define a normalized coefficient according to the expected background,

$$f_{90} = \frac{N_{90}}{N_b}.$$

Just like the way we can derive the detector trigger response from a given flux, so we can do the reverse and determine a source's flux once the number of counts is available. The γ-ray flux upper limit for a GRB is thus given by (Alexandreas, 1993),

$$\phi_\gamma(>E) = \frac{f_{90}\ \phi_B(>E)\ \Omega}{\epsilon\, R_\gamma},$$

where $\phi_B(>E)$ is the total cosmic ray flux above primary energy E (in TeV),

$$\phi_B(>E) = 0.132\ E^{-1.6}\ m^{-2}s^{-1}sr^{-1},$$

obtained from integrating the differential form of Tibet's cosmic ray spectrum in Equation 5.1, and Ω is the solid angle subtended by the source bin. In the case of a 3.4° circular bin, $\Omega = 2\,\pi\,(1-\cos 3.4°) = 0.011\ sr$. The coefficient ϵ is the fraction of the signals that are expected to be contained in the 3.4° circular bin. As shown in Figure 5.3 (b), ϵ is equal to 0.39.[20]

The last parameter R_γ stands for the detection efficiency ratio between a γ shower and a cosmic-ray background shower. Its reasoning comes from the following consideration — with all other conditions fixed to be the same, how easy it is for a γ shower to trigger the detector compared to a proton shower. Therefore, R_γ can be found by directly examining the effective areas for both cases in Figure 5.1. For example, $R_\gamma = 1.3$ at energy of 20 TeV, $R_\gamma = 1$ at 12 TeV, $R_\gamma = 0.76$ at energy of 3.5 TeV, and $R_\gamma = 0.58$ at 1 TeV.[21] However, in real data, since the primary energy is unknown, R_γ cannot be determined on an event-by-event basis.

An alternative is to consider the zenith angle. Since the trigger energy increases with zenith angle and the zenith angle is available for every event, we can find out the θ dependency for R_γ and use it. As shown in Table 5.1, the number of Monte Carlo showers thrown at a certain fixed θ angle for all data sets, except the solo point of 50 TeV γ, is the same between proton and γ showers. Therefore, the R_γ ratio at this certain zenith angle can be determined by counting the number of resulting Monte Carlo triggered events for both γ and proton showers with that θ value. For all energy ranges except 50 TeV, which does not

[20]Later, we have to make some modification for bursts with large positional uncertainties. In the case of a 5.2° circular bin, $\Omega = 2\,\pi\,(1-\cos 5.2°) = 0.026\ sr$ and ϵ is 0.49.

[21]The independent simulation results from Biller (Biller, 1992) shows an $R_\gamma = 2.5$ for the CYGNUS experiment. Considering the median energy for CYGNUS is around 100 TeV, it generally supports the crossover around 12 TeV.

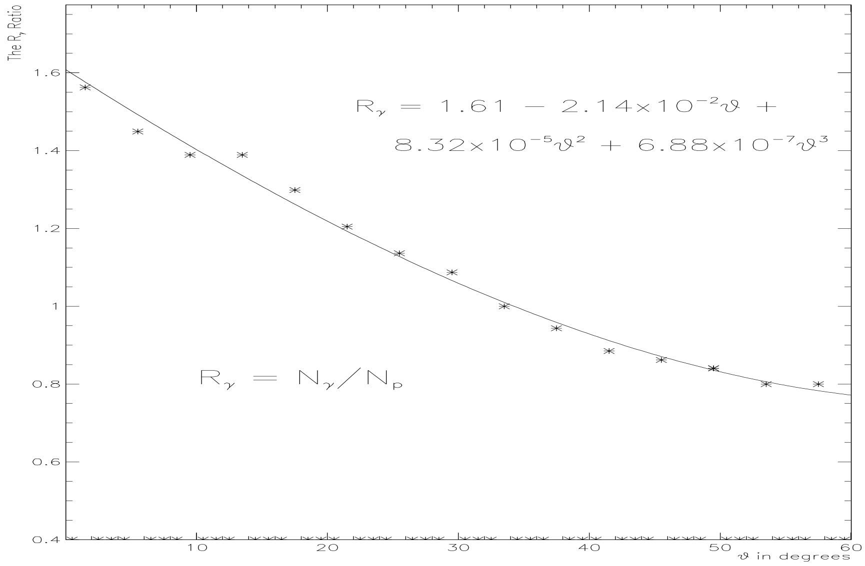

Figure 5.10: The R_γ ratio derived from Monte Carlo events.

have a proton entry, and 0.04-0.06 TeV, which has relatively poor statistics, the triggers in Monte Carlo data set are combined and sorted in terms of the zenith angles. In addition, as shown in Table 5.1, even though the majority of Monte Carlo triggers are with energies 0.1-8 TeV, to preserve the appropriate energy spectrum relative to the 0.1-8 TeV data set (3×10^7 γ and 3×10^7 proton showers), triggers with energies 20 TeV (25,000 showers), 12 TeV (5×10^4 showers), 0.085-0.1 TeV (10^7 showers), and 0.06-0.085 TeV (10^7 showers) are assigned with different weights of 0.02, 0.038, 0.89, and 2.91, respectively. After the process, the number of γ triggers with, for example, $44 > \theta > 40$ is $N_\gamma(42) = 246.7$, and the number of proton triggers with $44 > \theta > 40$ is $N_p(42) = 278.8$; thus, $R_\gamma(42) = \frac{246.7}{278.8} = 0.89$. The "cosine effect" has been canceled out since they are all at the same zenith angles. The relation between R_γ and θ is shown in Figure 5.10 .

After plugging in all these numbers, we derive the 90% confidence level γ flux upper limit to be

$$\phi_\gamma(> 3.5\ TeV) = \frac{f_{90} \times 0.132 \times 3.5^{-1.6} \times 0.011}{0.39 \times R_\gamma} = 5.02 \times 10^{-4} \times \frac{f_{90}}{R_\gamma}\ m^{-2}s^{-1}$$

for the method we use to search for GRBs.

5.6 Corrections for Bursts with Large Position Errors

As seen in Table 5.2, some source candidates have large positional uncertainties, which are larger than the derived 3.4° optimal search bin. Assuming there are no systematic errors in BATSE's pointing, the search method is modified and categorized into four groups: (1) if the error radius of a source candidate in Table 5.2 is smaller than or similar to Milagrisimo's angular resolution, $\sim 2.1°$, we proceed as planned and treat it as a point source;

this scenario covers 7 (960521, 960525, 960529, 960607, 960616, 960621B, and 960623) of the 16 listed bursts, (2) if the position error of a burst is larger than those in the previous group but smaller than $\sim 5.2^\circ$ (this group covers 5 bursts: 960425, 960521B, 960601, 960618 and 960620), a circular bin with the GRB's error radius plus 1° is used as its search bin size to calculate the probability, (3) since GRB 960507 and GRB 960621D have position errors

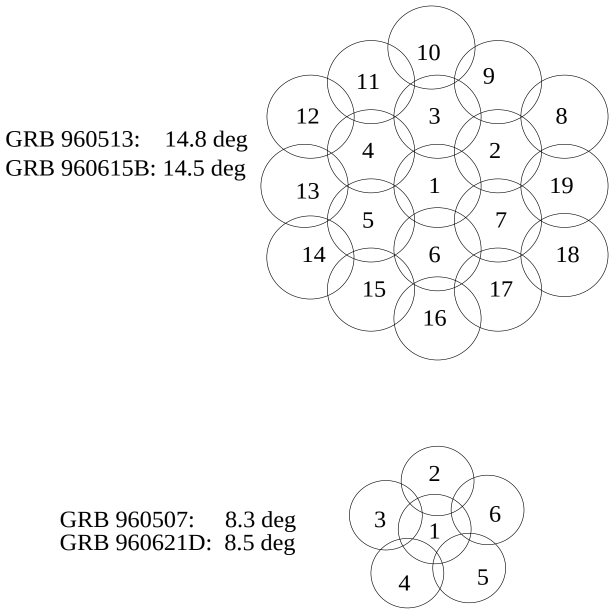

Figure 5.11: The search plan for four GRBs with large positional errors.

$\sim 8^\circ$, for each of them, 6 bins with radius of 3.4° around the burst's location (as shown in the lower drawing of Figure 5.11) are used to estimate the probability, and (4) for each of GRB 960513 and GRB 960615B, that have position errors $\sim 14^\circ$, 19 bins with radius of 5.2° around the burst's location (as shown in the upper drawing of Figure 5.11) are used to search for the burst.

The suitability for the second group is verified in Figure 5.3 (c); if the bin size is released from 3.4° to 5.2°, the sensitivity drops from 0.580 to 0.562, which is only 3%. Even if the bin size doubles to 6.8°, the sensitivity drops only 10%.

For the third and fourth groups, the final results will be derived after the 6 (GRB 960507 and GRB 960621D) and 19 (GRB 960513 and GRB 960615B) individual probabilities have been determined.

5.7 Search Results

Now that the search method has been proposed and verified for its suitability, it is time to run through the real data and present the results. GRB 960425, 960618 and 960621D do not have T_{90} or T_{start} values available. They are assigned with values $T_{90} = 1$ and $T_{start} = 0$. The results of the 7 VHE γ-ray source candidates in group one, the 5 candidates in group two, and 2 candidates in group three, based on the direction and the time of BATSE 4B GRB catalog, are listed in table 5.4. The results of the 2 VHE γ-ray source candidates in group four from the direction and the time of BATSE 4B GRB catalog are listed in table 5.5. There is not statistically significant excess of events from any burst.

Since there are 6 and 19 independent trials for group three and group four, respectively, the true probabilities are higher than the smallest assessed probabilites shown in the table. Since there are no significant excesses for any of the different trails, the trail factor is not important and the smallest probabilities and highest upper limits are quoted for those bursts, as indicated by the entries in boldface.

5.8 Conclusion

If the energy spectrum of a GRB on the list is known in the high energy domain, the upper limit we just derived for the GRB can be compared with the extrapolated spectrum in the VHE region. Thus, the distance for this GRB can be addressed as discussed in the AGN case in Figure 1.11. Unfortunately, none of the 16 GRBs has its energy spectrum measured by EGRET.

As shown in the last column of Table 5.2, the peak flux (measured in 1024 ms intervals) in an energy range of 50 keV – 300 keV of a GRB is available. Now that the flux limit of a GRB for energy above 3.5 TeV is known, we can connect these two points to derive a limit on the energy spectrum for the burst. A list of the spectral indices for all the bursts is summarized in Table 5.6. For bursts with their energy spectra measured by BATSE and EGRET, the power law indices vary anywhere from -1.7 to -4.3. The majority of them ($> 65\%$) have values close to -2 (Band, 1993). As shown in the table, our results fall in the acceptable range. However, the data are not strong enough to address the GRB distance or the absorption issue.

In summary, after the data have been analyzed to search for radiation from the directions of gamma-ray bursts listed in BATSE's 4B catalog, there is no evidence of statistically significant excess above the expected cosmic-ray background found from the direction of any of the 16 GRBs in the field of view of Milagrisimo. However, upper limits for the steady γ-ray flux above 3.5 TeV are quoted at 90% confidence level.

GRB No.	θ	ϕ	R_γ	N_s	N_b	N_B	P $(\geq N_s)$	LiMa σ	N_{90}	Upper Limit ϕ_γ $(\geq 3.5TeV)$
960521	38.5	232.0	0.93	5	4.45	1148	0.458	0.26	5.45	6.67×10^{-4}
960525	18.9	73.8	1.25	18	15.06	542	0.260	0.73	10.34	2.77×10^{-4}
960529	39.6	35.8	0.93	5	4.29	1372	0.427	0.33	5.54	7.05×10^{-4}
960607	49.6	108.1	0.83	12	10.45	836	0.357	0.47	8.07	4.68×10^{-4}
960616	33.8	63.0	1.00	0	0.02	3119	1.	-	2.30	6.87×10^{-2}
960621B	26.8	344.9	1.11	30	25.77	5772	0.227	0.81	13.25	2.33×10^{-4}
960623	28.5	262.2	1.07	62	50.63	6228	0.067	1.54	23.02	2.11×10^{-4}
960425	40.0	156.9	0.92	0	0.92	7863	1.	-	2.30	4.43×10^{-3}
960521B	17.9	156.5	1.27	4	4.89	7164	0.720	-0.42	4.40	6.21×10^{-4}
960601	41.8	120.0	0.90	2	1.28	2290	0.366	0.59	4.26	3.87×10^{-3}
960618	17.7	77.8	1.28	2	1.55	12522	0.459	0.35	4.10	2.78×10^{-3}
960620	31.9	184.2	1.03	6	9.15	15715	0.893	-1.11	4.34	7.69×10^{-4}
960507	35.1	201.7	0.98	0	0.53	4280	1.	-	2.30	2.25×10^{-3}
	40.9	201.7	0.91	0	0.37	3031	1.	-	2.30	3.69×10^{-3}
	30.4	205.1	1.05	0	0.67	5402	1.	-	2.30	1.54×10^{-3}
	30.4	198.3	1.05	1	0.66	5377	0.484	0.39	3.42	2.31×10^{-3}
	36.9	207.2	0.96	0	0.47	3827	1.	-	2.30	2.62×10^{-3}
	36.9	**196.2**	**0.96**	**2**	**0.47**	**3824**	**0.082**	**1.65**	**4.87**	$\mathbf{5.53 \times 10^{-3}}$
960621D	48.9	131.3	0.83	0	0.10	380	1.	-	2.30	1.47×10^{-2}
	54.7	131.3	0.80	0	0.05	219	1.	-	2.30	2.77×10^{-2}
	44.2	134.7	0.88	0	0.14	578	1.	-	2.30	8.69×10^{-3}
	44.2	127.9	0.88	0	0.14	568	1.	-	2.30	8.85×10^{-3}
	50.7	136.8	0.82	0	0.08	315	1.	-	2.30	1.83×10^{-2}
	50.7	**125.8**	**0.82**	**0**	**0.08**	**309**	**1.**	**-**	**2.30**	$\mathbf{1.86 \times 10^{-2}}$

Table 5.4: The GRB search results for Milagrisimo data. There are eleven columns in the table: (1) GRB No. is the BATSE 4B catalog Gamma Ray Burst identifier, (2) θ is the local Milagrisimo incident zenith angle in decimal degrees, (3) ϕ is the local Milagrisimo incident azimuth angle in decimal degrees, (4) R_γ is the detection efficiency ratio between a γ shower and a cosmic-ray background shower, (5) N_s is the observed counts in the on-source bin, (6) N_b is the expected counts in an off-source bin, (7) N_B is the total counts in all off-source bins in the Milagrisimo Run, (8) $P(\geq N_s)$ is the probability to observe N_s or more events under the expected background configuration, (9) LiMa σ is the parameter of LiMa significance, (10) N_{90} is the 90% confidence level upper limit counts for the source contribution, and (11) ϕ_γ is the 90% confidence level γ-ray flux upper limit (in $m^{-2}s^{-1}$) for energies greater than 3.5 TeV. Different Ω and ϵ values are applied for cases with different bin sizes. For clarity, they are not shown in the table.

GRB No.	θ	ϕ	R_γ	N_s	N_b	N_B	P ($\geq N_s$)	LiMa σ	N_{90}	Upper Limit ϕ_γ ($\geq 3.5TeV$)
960513	38.5	232.0	0.93	0	0.37	8868	1.	-	2.30	7.83×10^{-3}
	24.9	232.0	1.14	0	0.68	16183	1.	-	2.30	2.90×10^{-3}
	31.7	232.0	1.03	0	0.53	12604	1.	-	2.30	4.53×10^{-3}
	45.3	232.0	0.86	0	0.23	5540	1.	-	2.30	1.48×10^{-2}
	52.1	232.0	0.81	0	0.13	3197	1.	-	2.30	2.87×10^{-2}
	28.3	237.9	1.09	0	0.62	14571	1.	-	2.30	3.52×10^{-3}
	35.1	237.9	0.98	0	0.45	10745	1.	-	2.30	5.88×10^{-3}
	41.9	237.9	0.90	0	0.30	7159	1.	-	2.30	1.04×10^{-2}
	48.7	**237.9**	**0.84**	**1**	**0.18**	**4343**	**.168**	**1.33**	**3.73**	$\mathbf{3.20 \times 10^{-2}}$
	28.3	226.1	1.09	0	0.61	14396	1.	-	2.30	3.57×10^{-3}
	35.1	226.1	0.98	0	0.45	10737	1.	-	2.30	5.88×10^{-3}
	41.9	226.1	0.90	0	0.29	6906	1.	-	2.30	1.08×10^{-2}
	48.7	226.1	0.84	0	0.18	4188	1.	-	2.30	2.05×10^{-2}
	31.7	243.8	1.03	0	0.53	12630	1.	-	2.30	4.52×10^{-3}
	38.5	243.8	0.93	0	0.38	8897	1.	-	2.30	7.81×10^{-3}
	45.3	243.8	0.86	1	0.24	5720	.215	1.15	3.68	2.28×10^{-2}
	31.7	220.2	1.03	0	0.53	12659	1.	-	2.30	4.51×10^{-3}
	38.5	220.2	0.93	0	0.37	8662	1.	-	2.30	8.03×10^{-3}
	45.3	220.2	0.86	0	0.23	5368	1.	-	2.30	1.52×10^{-2}
960615B	26.8	94.5	1.11	0	0.73	6669	1.	-	2.30	3.35×10^{-3}
	13.2	94.5	1.35	1	1.14	10432	.681	-0.14	3.22	4.99×10^{-3}
	20.0	94.5	1.23	0	0.97	8848	1.	-	2.30	2.05×10^{-3}
	33.6	94.5	1.01	2	0.51	4635	.093	1.58	4.84	1.25×10^{-2}
	40.4	94.5	0.92	0	0.29	2692	1.	-	2.30	1.21×10^{-2}
	16.6	100.4	1.30	2	1.06	9708	.287	0.81	4.39	3.21×10^{-3}
	23.4	100.4	1.16	0	0.86	7820	1.	-	2.30	2.60×10^{-3}
	30.2	100.4	1.05	2	0.63	5772	.133	1.37	4.73	8.85×10^{-3}
	37.0	100.4	0.95	1	0.40	3672	.331	0.79	3.57	1.28×10^{-2}
	16.6	88.6	1.30	1	1.07	9743	.656	-0.07	3.25	2.37×10^{-3}
	23.4	88.6	1.16	0	0.85	7775	1.	-	2.30	2.62×10^{-3}
	30.2	88.6	1.05	1	0.61	5575	.457	0.46	3.45	6.68×10^{-3}
	37.0	88.6	0.95	0	0.40	3608	1.	-	2.30	8.42×10^{-3}
	20.0	106.3	1.23	2	0.98	8973	.258	0.90	4.46	3.90×10^{-3}
	26.8	106.3	1.11	1	0.75	6868	.529	0.27	3.38	4.76×10^{-3}
	33.6	**106.3**	**1.00**	**3**	**0.52**	**4776**	**.016**	**2.35**	**6.16**	$\mathbf{1.53 \times 10^{-2}}$
	20.0	82.7	1.23	2	0.97	8884	.254	0.91	4.46	3.94×10^{-3}
	26.8	82.7	1.11	0	0.73	6680	1.	-	2.30	3.35×10^{-3}
	33.6	82.7	0.99	0	0.49	4517	1.	-	2.30	6.11×10^{-3}

Table 5.5: The extension of Table 5.4 for the two bursts in group four.

GRB No.	flux (50-300 keV) $photons/m^2/sec$	flux ($\geq$ 3.5 TeV) $photons/m^2/sec$	differential energy spectral index
960521	0.66×10^4	$< 6.67 \times 10^{-4}$	< -1.88
960525	0.81×10^4	$< 2.77 \times 10^{-4}$	< -1.94
960529	18.43×10^4	$< 7.05 \times 10^{-4}$	< -2.06
960607	8.74×10^4	$< 4.68 \times 10^{-4}$	< -2.04
960616	0.29×10^4	$< 6.87 \times 10^{-2}$	< -1.58
960621B	0.38×10^4	$< 2.33 \times 10^{-4}$	< -1.91
960623	3.13×10^4	$< 2.11 \times 10^{-4}$	< -2.03
960425	0.44×10^4	$< 4.43 \times 10^{-3}$	< -1.76
960521B	1.12×10^4	$< 6.21 \times 10^{-4}$	< -1.92
960601	0.83×10^4	$< 3.87 \times 10^{-3}$	< -1.80
960618	0.66×10^4	$< 2.78 \times 10^{-3}$	< -1.80
960620	0.29×10^4	$< 7.69 \times 10^{-4}$	< -1.83
960507	0.41×10^4	$< 5.53 \times 10^{-3}$	< -1.74
960621D	N/A	$< 1.86 \times 10^{-2}$	N/A
960513	0.21×10^4	$< 3.20 \times 10^{-2}$	< -1.61
960615B	0.23×10^4	$< 1.53 \times 10^{-2}$	< -1.65

Table 5.6: A list of spectral index upper limits for the burst candidates. The fluxes in second column are supplied by BATSE and the fluxes in the third column are our flux limits. For each burst, the differential spectral index is determined by directly connecting these two flux points.

Appendix A

Moon Shadow

Most ground-based UHE γ-ray experiments examine their data around the directions of sun and moon to calibrate possible systematic errors in the pointing of the detectors, as well as their angular resolutions.

Cosmic rays from behind the sun and moon cannot penetrate the sun and moon to reach a detector on the earth. As a result, the obtained homogeneous sky background map should show a deficit, or shadow, from the direction of the sun and the moon. Since the angular span of the sun or moon and its location at any time can be well measured, by quantitatively looking at how sharp the shadow edge is, we can determine the detector's angular resolution. Also, by checking how far the shadow's center deviates from the expected position, we can derive the detector's pointing systematic.

However, because the homogeneous background showers are charged particles (most of them are protons), their trajectories are altered by the magnetic fields around the sun and the earth. The expected shadow is shifted and dispersed in a complicated pattern, depending on the energies and energy spectrum of these constituent comic rays, the distance from the sun or moon to the detector, the trajectory orientation of cosmic rays relative to the direction of magnetic fields, the strength of the magnetic fields as well as the time-dependent nature caused by the sun's activities. The higher the primary energy, the more rigid the trajectory of the cosmic ray is.

Since the sun's magnetic fields are much stronger than earth's and the distance between sun and earth is greater than that between moon and earth, a detector has to record cosmic rays with higher energies in order to see sun's shadow than moon's shadow. Can Milagrisimo see even the moon shadow, then?

Deflection due to the earth's magnetic field is approximately 1.7° per TeV in the plane containing the local zenith angle and the east direction. This was estimated by calculating deflection due to $\int Bdl$ along the particle trajectory assuming a dipole magnetic field of the earth. Specifically in this plane, the angle made with respect to the local vertical is shifted by $1.7^{\circ}/E\,(TeV)$. For example, a moon shadow cast by many fixed energy 300 GeV proton events, which are recorded by a detector with perfect angular resolution, will be shifted by 6° from the position of the moon. If these protons are not fixed in energy but with a spectrum distribution, the shifted sharp disc will become an asymmetrical blurred comet-like chunk. Furthermore, if the detector does not have a perfect angular resolution, the situation is worse.

Unfortunately, because the trigger energy for Milagrisimo was too low (100 GeV for threshold; 3.5 TeV for median energy), the overall angular resolution of 2.1° was not good enough, and the experiment period was too short (not enough moon transit time) to accumulate enough data, Milagrisimo cannot see the moon shadow and thus cannot calibrate its pointing by using this technique.

Bibliography

Aguilar-Benitez, M. *et al.*: 1998, *Phys.Rev.D* **54**, 135

Alexandreas, D. *et al.*: 1993, *Nuclear Instruments & Methods In Physics Research* **328**, 570

Allen, G.: 1996, *Ph.D. thesis*, University of Maryland, College Park

Amenomori, M. *et al.*: 1996, *Astrophysical Journal* **464**, 954

Arfken, G.: 1985, *Mathmatical Methods for Physicists*, Acdemic Press, San Diego

Band, D. *et al.*: 1993, *Astrophysical Journal* **413**, 281

BATSE-Map: 1998, *http://cossc.gsfc.nasa.gov/cossc/BATSE.html*, NASA Public World Wide Web

Begelman, M.C. Blandford, R. & Rees, M.: 1984, *Review of Modern Physics* **56**, 255

Bell, A.: 1978, *Mon. Not. R. Astron. Soc.* **182**, 147

Biller, S. D.: 1992, *Ph.D. thesis*, University of California, Irvine

Boas, M.: 1983, *Mathmetical Methods in the Physical Sciences*, Wiley, New York

Brun, R. *et.al.*.: 1989, *PAW, Physics Analysis Workstation*, CERN

Burnett, T. *et al.*: 1983, *Physical Review Letters* **51**, 1010

Burnett, T. *et al.*: 1990, *Astrophysical Journal Letters* **349**, 25

CGRO: 1998, *http://cossc.gsfc.nasa.gov/descriptions/cgro_info.html*, NASA Public World Wide Web

Chanmugam, G. & Brecher, K.: 1985, *Nature* **313**, 767

Coppi, P. & Aharonian, F.: 1997, *Astrophysical Journal Letters* **487**, 9

Costa, E. *et al.*: 1997, *Nature* **387**, 783

Dingus, B.: 1988, *Ph.D. thesis*, University of Maryland, College Park

EGRET-Figure: 1998, *http://cossc.gsfc.nasa.gov/cossc/EGRET.html*, NASA Public World Wide Web

EGRET-Map: 1998, *http://cossc.gsfc.nasa.gov/cossc/EGRET.html*, NASA Public World Wide Web

Gaidos, J. *et al.*: 1996, *Nature* **383**, 319

Gaisser, T.: 1990, *Cosmic Rays and Particle Physics*, Cambridge Univ. Press, New York

GEANT, C. P. L.: 1994, *GEANT Reference Manual, Version 3.21*, CERN Geneva, Switzerland

Halzen, F. *et al.*: 1984, *Quarks & Leptons: An Introductory Course in Modern Particle Physics*, Wiley, New York

Hillas, A. & Lapikens, J.: 1977, in *Proc. 15th Int. Cosmic Ray Conference*, Vol. 8, p. 460

Hurley, K. *et al.*: 1994, *Nature* **372**, 652

Jackson, J.: 1975, *Classical Electrodynamics*, Wiley, New York

Kobayashi, S. *et al.*: 1997, *Astrophysical Journal* **490**, 92

Kopka, H. & Daly, P.: 1995, *A Guide to Latex 2e*, Addison-Wesley, Wokingham

Krane, K.: 1988, *Introductory Nuclear Physics*, Wiley, New York

Leo, W.: 1987, *Techniques for Nuclear and Particle Physics Experiments*, Springer-Verlag, Berlin

Leventhal, M. *et al.*: 1978, *Astrophysical Journal Letters* **225**, 11

Li, T.-P. & Ma, Y.-Q.: 1983, *Astrophysical Journal* **272**, 317

Longair, M.: 1992, *High Energy Astrophysics*, Cambridge, New York

Mészáros, P.: 1995, in *Proc. 17th Texas Conf.Relativ.Astrophys.*, Vol. 759, p. 440

Mészáros, P. & Rees, M.: 1993, *Astrophysical Journal* **417**, 742

Meyer, S.: 1987, *Data Analysis for Scientists and Engineers*, Wiley, New York

Nagle, D. *et al.*: 1988, *Annu. Rev. Nucl. Part. Sci.* **38**, 609

Nelson, W. *et al.*: 1985, *The EGS4 Code System*, SLAC, Stanford University

Norris, J. *et al.*: 1998, *http://glast.gsfc.nasa.gov/GBrJan98*, NASA GLAST Brochure

Paciesas, W. *et al.*: 1997, *http://www.batse.msfc.nasa.gov/data/grb/4bcatalog*, NASA Public World Wide Web

Press, W. *et al.*: 1990, *Numerical Recipes*, Cambridge Univ. Press, New York

Reines, F. *et al.*: 1989, *Bull. American Astron. Soc.* **21**, 798

Sahu, K. *et al.*: 1997a, *Nature* **386**, 683

Sahu, K. *et al.*: 1997b, *Astrophysical Journal Letters* **489**, 127

Schnee, R.: 1996, *Ph.D. thesis*, University of California, Santa Cruz

Sinnis, G.: 1992, *CYGNUS memo: "Calculating Upper Limits"* p. 4

Sokolsky, P.: 1989, *Introduction to Ultrahigh Energy Cosmic Ray Physics*, Addison-Wesley, Redwood City, California

Sommer, M. *et al.*.: 1994, *Astrophysical Journal Letters* **422**, 63

Wrotniak, J.: 1984, *Showersim/84, A Modular System For Monte Carlo Simulation of Cosmic Ray Cascade Phenomena in the Atmosphere*, Univ. of Delaware and Univ. of Maryland, College Park

Wu, J.: 1995, *Ph.D. thesis*, University of California, Riverside